



FACULTY OF SCIENCE AND TECHNOLOGY

MASTER THESIS

Study programme / specialisation:
Environmental Engineering

The spring semester, 2022

Author: John Senith Ravishan Fernando

Open / ~~Confidential~~

Senith

.....
(signature author)

Course coordinator: Roald Kommedal

Supervisor(s): Sachin Maruti Chavan

Thesis title: **Selective Recovery of Nickel and Cobalt from Spent Battery Waste (Black Mass) by Adsorption: Resin and MOF Case Study**

Credits (ECTS):30

Keywords:
Adsorption, black mass, Nickel, Cobalt
Resin, MOF-808,

Pages:134.....

+ appendix:8.....

Stavanger, 15th June 2022.
date/year

Selective Recovery of Nickel and Cobalt from Spent Battery Waste (Black Mass) by Adsorption: Resin and MOF Case Study

Master's Thesis
Environmental Engineering



by

Senith Fernando

Department of Chemistry, Bioscience and Environmental Engineering
Faculty of Science and Technology
University of Stavanger
June 2022

ABSTRACT

In recent years, metal recycling and recovery from spent battery waste has become an area receiving much attention from the research community and environmentalists. With the rapid electrification of vehicles, battery manufacturing has increased in the presence of limited resources. Therefore, efficient and environmentally benign means of reusing the resources in spent battery waste is crucial for sustainability. Thus, this study was conducted with the objective of recovering critical metals: cobalt and nickel, using adsorption from the black mass.

Several characterization studies such as XRD, TGA, N₂ sorption, SEM-EDS, ATR-IR and NMR were conducted for black mass and the adsorbents: Amberlite IRC-748 and Zr-MOF-808 to identify their properties. The batch adsorption experiments were conducted to determine the effects of pH, contact time, temperature, initial metal concentration, and liquid-solid ratio. MOF-808-EDTA showed the highest Ni²⁺ uptake from MOF-808 analogues considered with an adsorption capacity of 27.4 mg g⁻¹ and 90 times selectivity for Ni²⁺ compared to Co²⁺ in simulated mixed solution. Amberlite IRC-748 showed better adsorption in as received sodium form compared to the treated form and over 99 % removal for Ni²⁺ and Co²⁺ in simulated black mass metal solution. Moreover, Amberlite IRC-748 exhibited consistent adsorption capacities for the 3 adsorption cycles considered.

CONTENTS

Abstract	i
List of figures	vii
List of tables	xi
Acknowledgements	xiii
Abbreviations	xiv
1. Introduction	1
2. Literature review and theory	3
2.1 Structure of LIB and NiMH	3
2.2 Environmental impacts and challenges	4
2.3 Economic aspects of metal recovery	6
2.4 State of the art of metal recovery from black mass	6
2.4.1 Pretreatment	7
2.4.2 Metal extraction	8
2.4.3 Pyrometallurgy	8
2.4.4 Hydrometallurgy	9
2.4.5 Bio-metallurgy	11
2.4.6 Comparison of metal extraction technologies	11
2.5 Metal extraction in NiMH batteries	12
2.6 Separation of extracted metals	13
2.7 Adsorption	14
2.7.1 Selection of adsorbents	14
2.8 Batch adsorption experiments	15
2.8.1 Adsorption isotherms	15
2.8.2 Adsorption kinetics	16
2.9 Selectivity in adsorption	17
2.10 Column adsorption experiments	17
2.11 Resins as adsorbent and ion exchanger	18
2.11.1 Amberlite IRC 748 resin	21
2.11.2 Resin ion exchange	22
2.12 Metal-organic frameworks	22
2.12.1 Zirconium based MOFs	23

2.12.2	MOF-808 and its functionalized analogues	25
2.12.3	Metal adsorption by MOF-808	25
2.13	Proposed process flow for the recovery process	28
2.14	Research gap	29
2.15	Objectives of the study	29
3.	Materials and Methods	30
3.1	Materials	30
3.2	Characterization methods	30
3.2.1	X-ray powder diffraction (XRD)	30
3.2.2	Thermogravimetric Analysis (TGA)	31
3.2.3	Attenuated Total Reflection- Infrared spectroscopy (ATR-IR)	32
3.2.4	Scanning electron microscope-energy dispersive spectrometer (SEM-EDS)	33
3.2.5	Nitrogen sorption at 77 K	33
3.2.6	X-Ray Fluorescence spectroscopy (XRF)	35
3.2.7	Inductively coupled plasma - optical emission spectrometry (ICP-OES)	36
3.2.8	Nuclear magnetic resonance (NMR)	37
3.3	Digestion of black mass using aqua regia	37
3.4	Characterization of black mass	37
3.5	MOF-808 Synthesis and ligand exchange	37
3.5.1	Synthesis of MOF-808-acetate	38
3.5.2	Ligand exchange to form derivatives of MOF-808	38
3.5.3	Synthesis of MOF-808-EDTA.	39
3.6	MOF-808 characterization	39
3.7	Characterization of resins	39
3.8	Leaching of black mass	40
3.9	Determination of acid stability of MOF-808	41
3.10	Preparation of simulated solutions.	41
3.11	Preparation of UV-visible spectrometer calibration curves	41
3.12	Resin batch adsorption experiments	42
3.12.1	Pretreatment of resins	42
3.12.2	Determination of the effect of resin form and pH	42
3.12.3	Determination of the effect of temperature	42
3.12.4	Determination of adsorption kinetics	42

3.12.5 Adsorption isotherm experiment	42
3.12.6 Determination of the effect of liquid-solid ratio	43
3.12.7 Determination of the effect of liquid-solid ratio in the presence of Mn^{2+} and Li^+	43
3.12.8 Regeneration of resins	43
3.13 Resin column breakthrough experiment	43
3.14 Characterization of regenerated resins	44
3.15 MOF-808 batch adsorption experiments	44
3.15.1 Determination of the effect of pH	44
3.15.2 Determination of the effect of liquid-solid ratio	44
3.15.3 Determination of the effect of liquid-solid ratio in the presence of Mn^{2+} and Li^+	45
3.15.4 Regeneration of MOF-808-EDTA	45
3.16 Characterization of regenerated MOF-808-EDTA	45
3.17 Batch adsorption experiments in black mass citric acid leachate	45
4. Results and discussion	46
4.1 Characterization of black mass and black mass leached residue	46
4.1.1 Determination of the composition of black mass	46
4.1.2 Black mass XRD analysis	48
4.1.3 Black mass SEM-EDS analysis	49
4.1.4 Black mass TGA analysis	50
4.1.5 Black mass ATR-IR analysis	51
4.2 Synthesis of MOF-808-acetate and ligand exchange	52
4.3 Characterization of MOF-808	53
4.3.1 XRD analysis	53
4.3.2 ATR-IR spectra	54
4.3.3 TGA analysis	55
4.3.4 SEM analysis	59
4.3.5 Nitrogen sorption analysis	60
4.3.6 NMR analysis	61
4.4 Characterization of resins	62
4.4.1 Nitrogen sorption (BET) analysis	62
4.4.2 IR analysis	63
4.5 Black mass leaching experiments	63
4.5.1 Leachate compositions and leaching efficiencies	63

4.5.2 Acid pH profiles	65
4.6 MOF chemical stability in black mass leachates	67
4.7 Adsorption experiments	69
4.7.1 Calibration curves	69
4.7.2 Cobalt calibration curves	69
4.7.3 Nickel calibration curves	70
4.8 Ion-exchange experiments for resins in single metal solutions	70
4.8.1 Effect of variation of pH	70
4.8.2 Effect of variation of temperature	72
4.8.4 Adsorption kinetics	72
4.8.5 Adsorption isotherms	75
4.9 Ion-exchange experiments for resin in Ni ²⁺ and Co ²⁺ mixed simulated solution	78
4.9.1 Effect of variation of pH	78
4.9.2 Elution of metals	79
4.9.3 Adsorption kinetics	80
4.9.4 Effect of variation of Liquid-Solid ratio	82
4.10 Ion-exchange experiments for resin in Ni ²⁺ , Co ²⁺ , Mn ²⁺ and Li ⁺ simulated mixed solution to determine the liquid-solid ratio.	83
4.11 Determining the potential of reusing the resin in adsorption	84
4.12 Resin column breakthrough experiment	86
4.13 Characterization of regenerated resins	87
4.14 Batch adsorption experiments for MOF-808 in single metal solutions.	88
4.14.1 Effect of variation of pH	89
4.15 Batch adsorption experiments for MOF-808 in Ni ²⁺ and Co ²⁺ mixed simulated solution	90
4.15.1 Liquid-Solid ratio variation for MOF-808-acetate	90
4.16 Batch adsorption experiments for MOF-808-EDTA in Ni ²⁺ , Co ²⁺ , Mn ²⁺ and Li ⁺ mixed simulated solution to determine liquid-solid ratio	91
4.17 Determining the potential of recycling MOF-808-EDTA	92
4.18 Batch adsorption experiments for MOF-808-EDTA in Ni ²⁺ , Co ²⁺ , Mn ²⁺ and Li ⁺ mixed simulated solution to enhance removal % by varying the liquid-solid ratio	95
4.19 Characterization of regenerated MOF-808-EDTA	96
4.20 Adsorption experiments in citric acid leachate under optimum conditions	99
5. Error analysis	103

5.1 Preparation of UV-visible spectrophotometer calibration curves	103
5.2 Batch adsorption experiments	103
5.3 Comparison of ICP-OES and UV-visible spectroscopy determined adsorption results.	104
5.4 Characterization of black mass and adsorbents	105
6. CONCLUSION	106
7. RECOMMENDATIONS	108
References	110
APPENDIX	119
Appendix 1-XRF analyzed aqua regia digestion	119
Appendix 2-Comparison of leaching results of ICP-OES and XRF	119
Appendix 3-Determination of spent battery cathode configuration	120
Appendix 4-Calculation of Theoretical yield of MOF-808-acetate	120
Appendix 5-Calculations from BET curve for MOF-808-acetate	120
Appendix 6-Calculation of molar ratios of molecular species in MOF-808 from NMR spectra	121
Appendix 7-Calculation of LUB for resin column adsorption	124
Appendix 8-Adsorption experiments for MOF-808 in single metal solutions	125
Appendix 9-Metal adsorption in simulated solution -ICP-OES results summary	126

LIST OF FIGURES

Figure 2.1. LIB cathode material composition trend (Azevedo et al., 2018).....	4
Figure 2.2. Process flow diagram of metal recovery from LIB	7
Figure 2.3. Structural modifications forming active sites (Uemura et al., 2009)	15
Figure 2.4. Breakthrough curve with the movement of MTZ (Patel, 2019)	17
Figure 2.5. Amberlite IRC-748 (a) Chemical structure and (b) pH vs stability of Amberlite IRC 748 (Zainol & Nicol, 2009b).....	22
Figure 2.6. Structures and formulas of common zirconium MOFs (Moon et al., 2015)	23
Figure 2.7. MOF-808 structures (a) octahedral and triangular units (b) large adamantine pore in orange (c) Atomic structure C, black: O, red: Zr, blue: yellow and orange are pores (Furukawa et al., 2014).....	24
Figure 2.8. (a) MOF-808 composition indicating linker, modulator and solvent. Structures of (b) MOF-808-formate (c) MOF-808-acetate (d) MOF-808-benzoate (Aunan et al., 2021). ...	25
Figure 2.9. Structure of EDTA	26
Figure 2.10. Concept of BS-HMT for MOF-808-EDTA.....	26
Figure 2.11. Functional groups in the structures of (a) 3,4-dihydroxybenzoic acid (b) 3,5- diaminobenzoic acid.....	27
Figure 2.12 – Missing cluster and missing linker defects (Winarta et al., 2020)	28
Figure 2.13 Proposed process flow diagram for nickel and cobalt recovery	28
Figure 3.1. (a) Slurry form XRD sample preparation (b) XRD instrument.....	31
Figure 3.2. TGA instrument showing sample positions.....	32
Figure 3.3. ATR-IR instrument.....	32
Figure 3.4. SEM-EDS instrument.....	33
Figure 3.5. Types of adsorption isotherms (Naderi, 2015)	34
Figure 3.6. (a) Degassing unit with samples placed on heating positions (b) N ₂ sorption instrument with samples inserted for analysis	35
Figure 3.7. (a) XRF instrument (b) Solid samples placed on sample plate for XRF analysis ..	36
Figure 3.8. Experimental setup for synthesis of MOF-808-acetate.....	38
Figure 3.9. Experimental setup for ligand exchange	39
Figure 3.10. Experimental setup for black mass leaching.....	40
Figure 3.11. Solutions prepared for preparing calibration curve (a) nickel (b) cobalt	41
Figure 3.12. Resin breakthrough column experimental setup	44
Figure 3.13. Black mass leachate solutions after adsorption experiments.....	45

Figure 4.1. ICP-OES determined composition of digestion solution	47
Figure 4.2. X-ray diffraction patterns of black mass and black mass leach residues of acids.	49
Figure 4.3. SEM-EDS analysis: (a) EDS and (b) SEM of black mass. (c) EDS and (d) SEM for black mass after citric acid leaching	50
Figure 4.4. TGA for black mass and black mass after citric acid leaching.....	51
Figure 4.5. ATR-IR for black mass and citric acid leached black mass residue	51
Figure 4.6. Normalized X-ray diffraction patterns for (a) simulated MOF-808 (b) MOF-808-acetate slurry (c) MOF-808-acetate powder	53
Figure 4.7. Normalized X-ray diffraction patterns for MOF-808	54
Figure 4.8. ATR-IR spectra of MOF-808	55
Figure 4.9. Variation of weight and heat flow with time for MOF-808-acetate.....	56
Figure 4.10. Regions of TGA curve of MOF-808-acetate	56
Figure 4.11. Calculation of experimental weight % of regions for MOF-808-acetate.....	57
Figure 4.12. TGA curves for synthesized MOF-808-acetate batches	58
Figure 4.13. TGA curves for MOF-808 types	59
Figure 4.14. SEM images for MOF-808-acetate (a) as synthesized (b) after adsorption in citric acid black mass leachate. MOF-808-EDTA (c) as synthesized (d) after adsorption in citric acid black mass leachate	59
Figure 4.15. Nitrogen sorption isotherms for MOF-808	60
Figure 4.16. Nitrogen sorption isotherms for resins as received and treated	62
Figure 4.17. ATR-IR spectra for resins	63
Figure 4.18. Black mass leaching efficiency of citric and tartaric acid	65
Figure 4.19. pH profile for citric acid with volume of 1 M NaOH	66
Figure 4.20. pH profile for tartaric acid with volume of 1 M NaOH	66
Figure 4.21. pH profile for phosphoric acid with volume of 1 M NaOH	67
Figure 4.22. XRD of MOF-808-acetate after adsorption experiments in black mass leachates	67
Figure 4.23. XRD spectra of MOF-808-acetate after 24 h stirring in pH adjusted (a) citric acid without metals (b) citric acid leached black mass metal solution	68
Figure 4.24. (a) UV-visible spectra for cobalt (b) Calibration curve for absorbance vs concentration for cobalt in concentration range 250-2500 mgL ⁻¹	69
Figure 4.25. (a) UV-visible spectra for nickel (b) Calibration curve for absorbance vs concentration for nickel in concentration range 500-6000 mgL ⁻¹	70

Figure 4.26. (a) Variation of adsorption capacity with pH (a) for treated resins (b) as received resin	71
Figure 4.27. Variation of removal percentage with pH (a) for nickel and (b) cobalt for treated and as received resins	71
Figure 4.28. Variation of (a) adsorption capacity and (b) removal percentage of Ni ²⁺ and Co ²⁺ with temperature	72
Figure 4.29. Variation of (a) Ni ²⁺ concentration and (b) adsorption capacity of Ni ²⁺ with time	73
Figure 4.30. (a) Pseudo first order and (b) pseudo second order kinetic models for Ni ²⁺	73
Figure 4.31. variation of (a) Co ²⁺ concentration and (b) adsorption capacity of Co ²⁺ with time	74
Figure 4.32 (a) Pseudo first order and (b) pseudo second order kinetic models for Co ²⁺	74
Figure 4.33. Experimental and model adsorption isotherms for Ni ²⁺	75
Figure 4.34. (a) Langmuir and (b) Freundlich isotherm linear plots for adsorption isotherms of Ni ²⁺	76
Figure 4.35. Experimental and model adsorption isotherms for Co ²⁺	77
Figure 4.36. (a) Langmuir and (b) Freundlich isotherm linear plots for adsorption isotherms of Co ²⁺	77
Figure 4.37 (a) adsorption capacity and (b) metal ion removal percentages for adsorption cycles with pH	79
Figure 4.38. Variation of relative selectivity for Ni ²⁺ compared to Co ²⁺	79
Figure 4.39. Variation of (a) eluted concentration (b) elution recovery efficiency for samples adsorbed at different pH values	80
Figure 4.40. Variation of (a) metal concentration and (b) adsorption capacity of metals with time	80
Figure 4.41. (a) Pseudo first order and (b) pseudo second order kinetic models for Ni ²⁺	81
Figure 4.42. (a) Pseudo first order and (b) pseudo second order kinetic models for Co ²⁺	81
Figure 4.43 (a). Removal percentage and (b) adsorption capacity of Ni ²⁺ and Co ²⁺ in the mixed solution	82
Figure 4.44. Variation of relative selectivity for Ni ²⁺ compared to Co ²⁺ with liquid-solid ratio	82
Figure 4.45 (a) metal ion removal percentages and (b) adsorption capacity with solid-liquid ratio	83
Figure 4.46. Variation of relative selectivity for Ni ²⁺ compared to Co ²⁺	83

Figure 4.47. (a) adsorption capacity and (b) metal ion removal percentages for Ni ²⁺ adsorption cycles for samples with different solid-liquid ratios	85
Figure 4.48(a) adsorption capacity and (b) metal ion removal percentages for Co ²⁺ adsorption cycles for samples with different solid-liquid ratios	85
Figure 4.49. Variation of relative selectivity for Ni ²⁺ compared to Co ²⁺ for samples with different solid-liquid ratios.....	85
Figure 4.50. Resin breakthrough curve for mixed simulated solution of Ni ²⁺ , Co ²⁺ , Mn ²⁺ and Li ⁺	86
Figure 4.51. Nitrogen sorption isotherms for resins as received and regenerated resins	87
Figure 4.52. ATR-IR spectra for as received and regenerated resins.....	88
Figure 4.53. Variation of adsorption capacity with pH for (a) Nickel and (b) cobalt ions with MOF-808-types.....	89
Figure 4.54. Variation of removal percentages with pH for (a) Nickel and (b) cobalt ions with MOF-808-types.....	90
Figure 4.55. Variation of metal removal percentage and (b) adsorption capacity with solid-liquid ratio for MOF-808-acetate.....	91
Figure 4.56. Variation of relative selectivity for Ni ²⁺ compared to Co ²⁺ with solid-liquid ratio for MOF-808-acetate	91
Figure 4.57. Variation of metal removal percentage and (b) adsorption capacity with solid-liquid ratio for MOF-808-EDTA.....	92
Figure 4.58. Variation of relative selectivity for Ni ²⁺ compared to Co ²⁺ with solid-liquid ratio for MOF-808-EDTA.....	92
Figure 4.59. (a) adsorption capacity and (b) metal ion removal percentages for Ni ²⁺ adsorption cycles for samples with different solid-liquid ratios for MOF-808-EDTA.....	93
Figure 4.60 (a) adsorption capacity and (b) metal ion removal percentages for Co ²⁺ adsorption cycles for samples with different solid-liquid ratios for MOF-808-EDTA	94
Figure 4.61. Variation of relative selectivity for Ni ²⁺ compared to Co ²⁺ for samples with different solid-liquid ratios for MOF-808-EDTA.....	94
Figure 4.62. (a) Metal ion removal percentages and (b) adsorption capacity with further optimized solid-liquid ratios	95
Figure 4.63. Variation of relative selectivity for Ni ²⁺ compared to Co ²⁺ with further optimized solid-liquid ratios	95
Figure 4.64. X-ray diffraction patterns for as synthesized and regenerated MOF-808-EDTA.	96

Figure 4.65. TGA for as synthesized and regenerated MOF-808-EDTA	96
Figure 4.66. ATR-IR spectra for as synthesized (red) and regenerated MOF-808-EDTA(blue)	97
Figure 4.67. Nitrogen sorption isotherms for as synthesized, metal adsorbed and regenerated MOF-808-EDTA	98
Figure 4.68. EDS analysis for (a) metal adsorbed and(b) regenerated MOF-808-EDTA	99
Figure 4.69. X-ray diffraction patterns for MOF-808 types in citric acid black mass leachate adjusted at pH 6	101
Figure 4.70. TGA for MOF-808 types in citric acid black mass leachate adjusted at pH 6 ..	102
Figure 6.1. Suggested process flow diagram for recovery of Ni ²⁺ and Co ²⁺	107

LIST OF TABLES

Table 2.1. Mine production of cobalt distribution in 2019	5
Table 2.2. Mine production of nickel distribution in 2019	6
Table 2.3. Summary of studies on leaching of valuable metals from spent LIB waste	10
Table 2.4. Advantages, disadvantages and environmental impacts of metal extraction techniques(Garole et al., 2020; Zheng et al., 2018).....	11
Table 2.5. Summary of studies on leaching of valuable metals from spent NiMH battery waste	12
Table 2.6. Properties of chemical and physical sorption (Basuki et al., 2019).....	14
Table 2.7. Properties of commercially available iminodiacetic chelating resins.....	19
Table 2.8. Studies conducted on metal uptake by resins.....	20
Table 2.9. Properties of Amberlite IRC-748.....	21
Table 2.10. Studies on adsorption recovery of metals using MOF-808.....	27
Table 3.1. Quantities of chemicals required for ligand exchange	38
Table 3.2. Optimized conditions used for black mass leaching.....	40
Table 4.1. XRF analyzed composition for black mass	46
Table 4.2. ICP-OES analyzed composition for digested solution	46
Table 4.3. Mean leachate metal weight percentages	47
Table 4.4. MOF-808-acetate yields for the synthesized batches.	52
Table 4.5. Comparison of theoretical and experimental weight loss percentages.	58

Table 4.6. Calculated properties from BET curve equation of MOF-808	61
Table 4.7. Summary of NMR quantified molar ratios for MOF-808	61
Table 4.8. Calculated properties from BET curve equation for resins	62
Table 4.9. Metal composition of black mass leachates from acids	64
Table 4.10. Metal leaching efficiencies of black mass leachates from acids.....	64
Table 4.11. Calculated parameters from the kinetic models	75
Table 4.12. Calculated parameters from Ni ²⁺ adsorption isotherm models	76
Table 4.13. Calculated parameters from Co ²⁺ adsorption isotherm models	78
Table 4.14. Calculated parameters from adsorption kinetics models.....	81
Table 4.15. Resin masses used for adsorption cycles.....	84
Table 4.16. Summary of calculated bed lengths for breakthrough curves.	86
Table 4.17. Comparison of calculated properties from BET curve equation for regenerated resins.....	87
Table 4.18. Mass of MOF-808-EDTA used for adsorption cycles	93
Table 4.19. Comparison of calculated properties from BET curve equation for regenerated MOF-808-EDTA	98
Table 4.20. Summary of adsorption experiments with citric acid black mass leachate	100
Table 4.21. Metal composition in pH 6 adjusted citric acid black mass leachate	100
Table 5.1 Error analysis for Ni ²⁺ calibration standard absorbance values	103
Table 5.2. Error analysis for Co ²⁺ calibration standard absorbance values	103
Table 5.3. Error analysis for resin batch adsorption experiment to determine the effect of liquid-solid (L-S) variation in simulated solution of Ni ²⁺ , Co ²⁺ , Mn ²⁺ and Li ⁺	104
Table 5.4. Comparison of ICP-OES and UV-visible spectroscopy results for Ni ²⁺ and Co ²⁺ batch adsorption with MOF-808-EDTA at different liquid-solid ratios	105

ACKNOWLEDGEMENTS

This thesis is the ultimate product of a combined effort of many supporters. First, I would like to thank my parents and past teachers who shaped me into the person I am today.

I would like to express my gratitude to my thesis supervisor, associate professor Sachin Maruti Chavan for having confidence in me to hand over the thesis project, continuously supporting in related matters sharing the knowledge, especially in material characterization techniques and reviewing the draft report. Special thanks go to associate professor Kidane Fanta Gebremariam for the support in XRF analysis. I would like to thank the two PhD students, Simmy Rathod and Ananya Chari, for their extensive support in the experimental work.

I would also like to thank the support given by all the laboratory engineers in the university laboratories by providing training for the analytical instruments and guiding throughout the instrumental analysis work.

Finally, I would like to thank my colleagues, Shiva Hashemi and Bilal Asghar, for their excellent companionship in the laboratories. Also, I like to remind the support given by the academic staff of the chemistry, life sciences and environmental technology department and my batch mates from the Environment Engineering Master's degree program throughout the study period.

John Senith Ravishan Fernando

Stavanger, Norway

15th June 2022

ABBREVIATIONS

ATR-IR	Attenuated Total Reflection- Infrared
BET	Brunauer-Emmett-Teller
BS-HMT	Broad-Spectrum Heavy Metal ion Trap
BTC	Benzene tricarboxylic
DHBA	dihydroxybenzoic acid
EDTA	Ethylenediaminetetraacetic acid
ICP-OES	Inductively Coupled Plasma - Optical Emission Spectrometry
LCO	Lithium Cobalt Oxide
LIB	Lithium Ion Battery
LUB	Length of Unsued Bed
NMC	Nickel Manganese Cobalt
NiMH	Nickel-Metal Hydride
NMR	Nuclear Magnetic Resonance
MOF	Metal Organic Frameworks
MTZ	Mass Transfer Zone
PMMA	Polymethyl methacrylate
PVDF	Polyvinylidene fluoride
REE	Rare Earth Elements
SALE	Solvent Assisted Ligand Exchange
SBU	Secondary Building Units
SEM-EDS	Scanning Electron Microscope-Energy Dispersive
TGA	Thermogravimetric Analysis
UiO	Universitetet i Oslo
UV	Ultra Violet
XRD	X-Ray Diffraction
XRF	X-Ray Fluoresce

1. INTRODUCTION

Cobalt and nickel are critical transition d-block metals used in various applications. Cobalt is used in electrode production in batteries, super-alloys, magnets, catalysts, pigments, pharmaceuticals, and drying agents. Similarly, nickel is used in stainless steel and alloys, coatings, and electrodes, especially nickel-metal hydride (NiMH) batteries (Henckens & Worrell, 2020). It is estimated that global reserves of cobalt and nickel are 7.1 and 94 million metric tons, respectively (U.S. Geological Survey, 2021). Cobalt has become a cost-determining factor in battery manufacturing because of its scarcity compared to the other elements used in batteries (Sun et al., 2019).

LIB and NiMH batteries are rechargeable batteries used as energy storage in many electrical appliances, smartphones, and electric vehicles due to their reasonable energy density and cycle life (Etacheri et al., 2011; Rodrigues & Mansur, 2010). However, the usage of NiMH batteries has reduced significantly due to the higher self-discharge rate (Liang et al., 2019).

According to the estimates, 11 million Metric tons of LIBs will reach the end of life between now and 2030 and less than 5% are being recycled (Jacoby, 2019, p. 30). The heavy metals in these batteries will enter the food chain and may threaten human health (F. Guo et al., 2012). Recovery of these metals are essential due to the large number of spent NiMH batteries resulting from battery useful lifetime of two years (Meshram et al., 2017; Pradhan et al., 2021). Therefore, this study focuses on separating and recovering cobalt and nickel from spent batteries to limit the usage of new resources and prevent untreated disposal.

A detailed literature review was conducted to identify the research gap and objectives. Amberlite IRC-748 is a resin which has the potential to uptake divalent metal ions. Similarly, Zr-MOF-808 and its modified form of Zr-MOF-808-EDTA have been used in metal uptake studies. Therefore, a metal solution was prepared from the crushed electrode material of the spent battery waste to investigate the potential of metal uptake by Amberlite IRC-748 and Zr-MOF-808 types. Several acids, such as phosphoric acid, sulphuric acid and organic acids citric and tartaric, which showed the potential of leaching efficiently, were used to determine a stable media for the adsorbents. Laboratory scale experiments were conducted according to the methodology developed to achieve the aforementioned objectives. The metal uptake experiments were conducted initially in simulated solutions due to the limited availability of ICP-OES for the metal concentration analysis in the leachates. The effects of pH, temperature,

and liquid-solid ratio were analyzed to determine the metal uptakes together with adsorption kinetics and isotherm studies. This thesis report is a combination of seven sections.

1. Introduction
2. Literature review and theory
3. Materials and methods
4. Results and discussions
5. Error analysis
6. Conclusions
7. Recommendations

Note the following terminologies used in the thesis.

Black mass: Crushed electrode material of the spent battery waste

MOF-808: Zirconium MOF-808

Resin: Amberlite IRC-748

2. LITERATURE REVIEW AND THEORY

This section included a detailed literature review of the metal recovery from spent battery waste and materials used for metal recoveries, such as resins and MOF-808, with relevant theoretical backgrounds.

2.1 Structure of LIB and NiMH

Overall, the Li-ion batteries consist of 5–20% cobalt, 5–10% nickel, 5–7% lithium, 15% organic compounds and 7% plastics which may slightly vary depending on the producer (Ordoñez et al., 2016). The rechargeable Li-ion batteries are made of an anode and cathode to convert the stored chemical energy to electrical energy. The anode is graphite coated on copper foil. The cathode is of layered LiCoO_2 , LiNiO_2 or LiMn_2O_4 on Al foil and non-aqueous liquid electrolyte (Bruce et al., 2008; Chagnes & Pospiech, 2013; Chagnes & Swiatowsk, 2012). These active electrode materials are attached to the foils using a binder. Because of its thermoresistance and non-reactive properties, the widely used binder is Polyvinylidene fluoride (PVDF). Polyethylene (PE) or polypropylene (PP) is used as the separator to prevent the short circuit of the two electrodes (X. Zeng et al., 2014). The commonly used cathode layering material is LiCoO_2 which makes up 90% of the cathode while containing 7–8% of acetylene black and 3–4% of the organic binder (Y. Guo et al., 2016). The material, $\text{LiNi}_x\text{Co}_y\text{Mn}_{1-x-y}\text{O}_2$ has become the best choice for cathode materials due to its stable structure, higher capacity of discharge, lower cost and better cyclic performance (Zheng et al., 2018). The electrolyte consists of high dielectric constant salts of lithium such as LiPF_6 , LiBF_4 , LiCF_3SO_3 , or $\text{Li}(\text{SO}_2\text{CF}_3)_2$ dissolved in organic solvents such as dimethyl sulfoxide, propylene carbonate, and ethylene carbonate (Chagnes & Pospiech, 2013; X. Zeng et al., 2014).

At present, five LIB technologies are available with different cathode compositions; lithium cobalt oxide (LCO), lithium nickel manganese cobalt (NMC), lithium nickel cobalt aluminium (NCA), lithium iron phosphate (LFP), and lithium manganese oxide (LMO) (Azevedo et al., 2018).

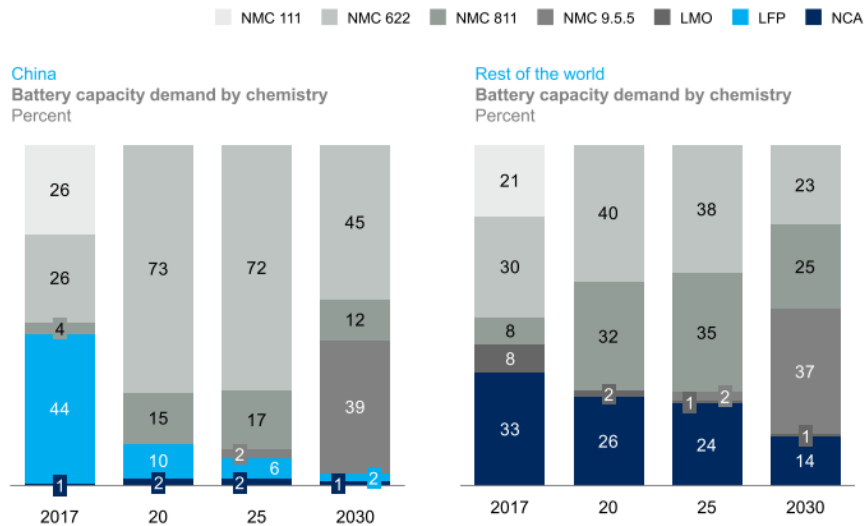


Figure 2.1. LIB cathode material composition trend (Azevedo et al., 2018)

As shown in Figure 2.1, the global trend is to reduce the amount of cobalt content in the LIBs by moving from NMC 622 to NMC 811 and ultimately to NMC 9.5.5 (nickel 9 parts, manganese 0.5 parts, and cobalt 0.5 parts).

The NiMH battery consists of a porous polymer impregnated cathode as a mechanical support and a current collector with a nickel paste containing nickel hydroxide as the active material and electrode stabilizing additives, a polymer impregnated anode with the mixture of metal ions capable of hydride formation, a plastic separator, and a concentrated potassium hydroxide solution with minor constituents as the electrolyte. The porous electrode substrate acts as mechanical support for the active material and a current collector. Cobalt, calcium, and zinc are added in small quantities to improve the efficiency of the material and the electrical conductivity (Fila et al., 2019; Scott, 2009). NiMH batteries contain valuable metals such as nickel 33%, cobalt 3% and Rare Earth Elements (REE) 10% as hydrides in the anode.

2.2 Environmental impacts and challenges

Cobalt is obtained as a byproduct of mining of copper and nickel currently. The main supplier of global cobalt minerals is the Democratic Republic of the Congo, which accounted approximately for 54% of production in 2016, while China (~8 %), Canada (~5 %) and Australia (~5 %) (van den Brink et al., 2020) The table 2.1 indicates the leading countries of mine production of cobalt in 2019 (U.S. Geological Survey, 2021).

Table 2.1. Mine production of cobalt distribution in 2019

Country	Mine production (Metric tons)
The Democratic Republic of the Congo	100000
Russia	6300
Australia	5740
Philippine	5100
Cuba	3800
World total	144000

The rapid transformation toward clean energy has increased the demand for cobalt, and concerns are arising about whether cobalt resources can fulfil the requirements without any scarcity (Z. Chen et al., 2020). This concern has grown into a severe problem due to mining-related problematic situations such as the use of child labour and pollution in mining sites in the democratic republic of Congo, where over 50% of the global cobalt mining activities are carried out (van den Brink et al., 2020). The concentration of available cobalt mines in a few countries and their rapid depletion will create a scarcity in cobalt supplies in the near future. Therefore, the technological and management aspects of cobalt recovery need to be enhanced, making the necessary investments.

The inappropriate disposal of spent batteries would cause serious environmental problems such as heavy metal contamination, global warming due to incineration and an increase in terrestrial ecotoxicology potential due to the release of hazardous materials on both ground and underground. The REE mining and processing results in a significant environmental impact by accumulating in soil, bioaccumulating in plants, and entering the upper levels of the food chain.

Spent battery recycling and recovery processes also have their means of impacting the environment. The pyrometallurgy and hydrometallurgy processes of extracting metals increase global warming and human toxicity potential, respectively. There is also a high impact on global warming due to the transportation of spent batteries to recycling facilities (Boyden et al., 2016).

Nickel is mined mainly from Sulfide ores compared to the laterite ores, which is the other main source of nickel. These ores are typically low grade as sulfide ores, and laterite ores contain 0.2%-2% and 1.0%-1.6% nickel, respectively (Henckens & Worrell, 2020). Therefore, the mining and refining process is highly energy-intensive. This may lead to emit high amount of

greenhouse gases if the source of energy is a fossil fuel. In addition, nickel mining and refining may also destruct habitats and pollute water and soil.

Table 2.2 indicates the leading countries of mine production of nickel in 2019 (U.S. Geological Survey, 2021).

Table 2.2. Mine production of nickel distribution in 2019

Country	Mine production (Metric tons)
Indonesia	853000
Philippines	323000
Russia	279000
New Caledonia	208000
Canada	181000
World Total	2610000

The mine production of nickel showed a better distribution among the countries without localizing to a single country compared to the mine production of cobalt.

2.3 Economic aspects of metal recovery

The recovered metals from spent battery waste can be used in various applications. The possibility of using recovered metals again in battery manufacturing provides a direct incentive for battery manufacturers to recycle spent batteries. The recycling process costs come under the categories of fixed costs and variable costs, including the costs of technology and material costs, respectively. Based on cost-benefit analysis, the recovered metals decrease the raw material costs. Thus the hydrometallurgy recovered Lithium-cobalt oxide lithium and nickel cobalt manganese oxide, save 41% and 13% of virgin raw material costs (Steward et al., 2019). These benefits can be further increased by recovering more pure and higher value metals in higher quantities. The economic analysis also considers other benefits, such as positive impacts on the environment and society due to recycling as a result of reducing potential risks of untreated discharge of spent battery waste (Harper et al., 2019).

2.4 State of the art of metal recovery from black mass

Metal recovery has become a trending global research area because of the economic value of metals in spent metal equipment, the depletion of available metal resources and environmental concerns regarding the disposal of spent metals. The final objective of the metal recovery

process is the sustainable utilization of resources and pollution mitigation. The recovery process focuses on capturing the required components by separating them from the other materials (J. Wang et al., 2021). The recovery process is divided into three sections: pretreatment, extraction, and separation of metals, as illustrated in Figure 2.2.

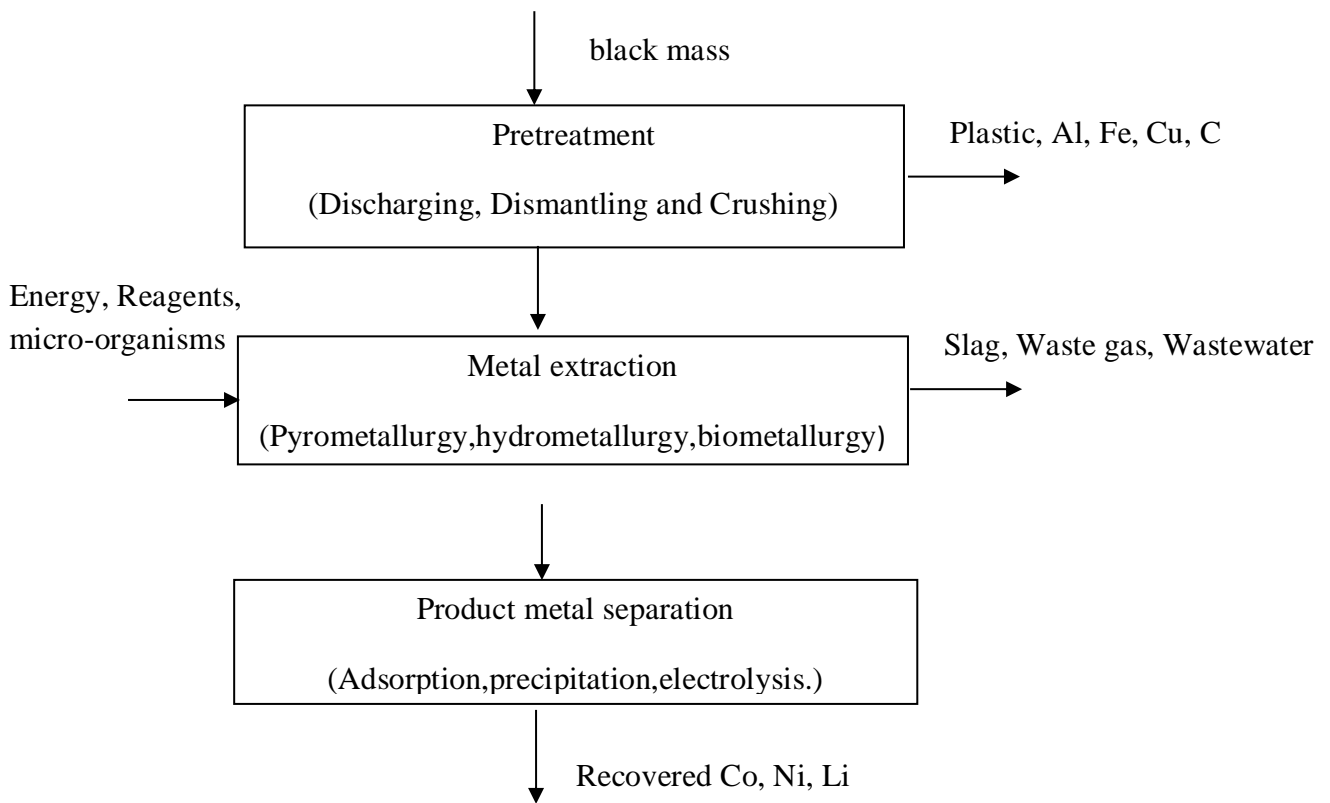


Figure 2.2. Process flow diagram of metal recovery from LIB

In LIBs, the metals copper, aluminium, and iron are in an elemental state, while cobalt, lithium and nickel are combined (X. Zeng et al., 2014). According to the process block diagram, the easily detachable parts of the spent Li-ion battery, such as plastic, copper, aluminium, iron and carbon, are separated in the pretreatment process from the combined metals. The combined metals can be extracted from the pretreated black mass using pyrometallurgy, hydrometallurgy, and bio-metallurgy. The extracted metals can then be separated by metal-specific techniques such as adsorption, precipitation and electrolysis to isolate the target metals.

2.4.1 Pretreatment

The spent LIBs can still contain residual charges. The Li metal is subjected to radical oxidation due to mechanical shock by overcharging when exposed to air, causing a blow-up (X. Zeng et al., 2014). Therefore, the battery needs to be discharged before carrying out any treatment to prevent short-circuiting or self-ignition (Li Li et al., 2011; Li Li et al., 2012). The discharging

process is carried out by connecting to a discharger until the battery is discharged below 0.1 V (Ku et al., 2016). Also, complete discharging can be achieved by adding 5 % (w/w) NaCl solution, deionized water washing, and drying or soaking in 1 mol L⁻¹ NaCl solution for 12 h (M.-M. Wang et al., 2017; Zhao et al., 2020).

The dismantling is carried out manually or by physical processes using gravity or magnetism. The plastic case is cut and removed. The metallic shell cover was immersed in liquid nitrogen for 4 min and fixed in a lathe before being cut open for safety. The battery's internal parts are taken out, and the both the electrodes are dried at 60 °C for 24 h and scraped to remove the attached metals from copper foil and the Al foil (Dorella & Mansur, 2007; Li Li et al., 2012). The separated materials are crushed in a CO₂ atmosphere to evaporate volatile organic components (Georgi-Maschler et al., 2012). The combined metals obtained are treated further to separate from other components such as copper, aluminium, and carbon.

2.4.2 Metal extraction

In the metal extraction process, solid-state metal compounds are transformed into their solution or alloy form. This process enhances the removal of cathode and anode materials on aluminium and copper foils. Several methods are used for the metal extraction process: pyrometallurgy, hydrometallurgy, and biometallurgy. The review by (Zheng et al., 2018) indicated that hydrometallurgy is the prominent method due to considerable recovery and purity of products.

2.4.3 Pyrometallurgy

Pyrometallurgy refers to the metal recovery processes under thermal treatment with chemical reactions at high temperatures. It includes many metal recovery processes such as calcination, roasting, smelting, and refining (Garole et al., 2020). These processes yield products such as alloys, including transition metals cobalt, nickel, iron, slag, lithium, aluminium, manganese and gasses, and volatile organic compounds at low temperatures (less than 250° C) and electrode and binder component emissions at higher temperatures.

The transition metals are recycled comparatively efficiently by the pyrometallurgy process. But the drawback is the emission of toxic gases, high process energy requirement, and the necessity of further treatment to get the final products. Therefore, pyrometallurgy is combined with hydrometallurgy for complete recovery (Harper et al., 2019; Piątek et al., 2020).

2.4.4 Hydrometallurgy

Hydrometallurgy involves sub-process dissolution and leaching, where solid metals change to solution form. Different types of reagents are used for this process depending on the metals in the solution and the target metal/s to be extracted. Some commonly used reagents as leaching agents are H_2SO_4 (F. Jiang et al., 2018; Zhao et al., 2020), ammoniacal solvents (Ku et al., 2016; H. Wang et al., 2017), mild organic acids (Nayaka et al., 2016; Yuliusman et al., 2018; X. Zeng et al., 2015). The recovery efficiency of cobalt is enhanced by using reducing agents such as H_2O_2 and ethanol at a moderate dosage of 3 % (v/v) and 5 % (v/v), respectively, which reduces Co^{3+} to Co^{2+} , and accelerates the leaching process by increasing the dissolving rate (Xiangping Chen et al., 2019; Zhao et al., 2020). H_2O_2 is the widely used reducing agent, while glucose (Xiangping Chen et al., 2016), NaHSO_3 (Meshram et al., 2015), and organic acids such as ascorbic acid are also being used (Li Li et al., 2012). The temperature, concentration of leaching agent and reducing agents, leaching time, and S/L ratio affect the leaching process (Zheng et al., 2018).

When considering acid leaching agents, HCl is more efficient compared to HNO_3 and H_2SO_4 (Joulié et al., 2014). Still, these inorganic acids are likely to emit hazardous gases such as SO_x , NO_x and Cl_2 . Also, the resulting leachates of low pH values require treatment before discharging into the environment (Yao et al., 2015). Therefore, using mild organic acids is a possible alternative which is comparatively environmentally friendly. According to (Ku et al., 2016), ammoniacal leaching is preferred over acid leaching due to reducing sodium hydroxide requirement for pH adjustment and eliminating manganese and aluminium separation steps.

Various combined technologies are being tested to enhance the efficiency and quality of recovered products. Spent LIB metals are recycled to produce LiCoO_2 crystals by applying electrochemical deposition technology to the leach liquor of nitric acid leaching, which results in only a 4% reduction in capacity after 30 cycles (Li Li et al., 2011). Investigations carried out on the ability of usage of reductive power of impurity metals such as copper, aluminium, and iron was implemented to enhance the dissolution of actively recovered metals with a cobalt and lithium recovery efficiency of over 99% while reducing the cost for reductants (C. Peng et al., 2019).

Table 2.3 shows the conditions and efficiencies of studies done using hydrometallurgy to recover cobalt, nickel and lithium in LIB using different leaching and reducing agents.

Table 2.3. Summary of studies on leaching of valuable metals from spent LIB waste

Leaching agent	Reducing agent	Conditions	Leaching efficiency	Reference
Deep eutectic solvents (DES)		200 °C 12 h	Co -95% Li -86%	(H. Guo et al., 2021)
Sulphuric acid (ultra sonic assisted)	H ₂ O ₂	30 °C 30 min	Co -94.63% Li-98.62%	(F. Jiang et al., 2018)
Ammonia	Ammonium sulphite	40 min	Ni -26% Co- 78%	(Ku et al., 2016)
Mild organic acids	Ascorbic acid	80 °C 1 h	Co and Li >90-95%	(Nayaka et al., 2016)
Ammonia	H ₂ O ₂		Co-96.3% Ni-96.4% Li-81.2%	(H. Wang et al., 2017)
Oxalic acid		95 °C 150 min 400 rpm	Co -97% Li-98%	(X. Zeng et al., 2015)
Sulphuric acid	Ethanol	90 °C 160 min	Co and Li >99%	(Zhao et al., 2020)
Ascorbic acid	Ascorbic acid	70 °C 20 min	Co-94.8% Li-98.5%	(Li Li et al., 2012)
Sulphuric acid	NaHSO ₃	95 °C 4 h	Co- 91.6% Ni- 96.4% Li-96.7% Mn-87.9%	(Meshram et al., 2015)
Citric acid	H ₂ O ₂	80 °C 90 min	Co- 95% Ni- 97% Li-99% Mn-94%	(Xiangping Chen & Zhou, 2014)

Studies above show that ammoniacal leaching and mild organic acid leaching result in similar metal recovery efficiencies as inorganic acid leaching. Therefore, ammoniacal leaching and

mild organic acid leaching are preferred over the others by considering favourable environmental aspects and reducing the cost of pH adjustments.

2.4.5 Bio-metallurgy

Bio-metallurgy is the process of leaching metals due to the acids produced by the metabolic activities of microorganisms (X. Zeng et al., 2014). *Acidithiobacillus ferrooxidans*, a chemolithotrophic acidophilic bacteria, produces ferric ions and sulphuric acid in the medium by using ferrous ions and elemental sulphur as energy sources. When the ferrous ion concentration is higher, the metal dissolution is lower due to the co-precipitation of metals with formed ferric ions (Mishra et al., 2008). Cobalt recovery of 99.9% was obtained after six days of bioleaching in the presence of 0.75 g L⁻¹ of copper ions. In contrast, only 43.1 % of cobalt recovery was observed after ten days of leaching in the absence of copper ions (G. Zeng et al., 2012). However, the drawback of biometallurgy is the slower leaching rate compared to hydrometallurgy.

2.4.6 Comparison of metal extraction technologies

The metal extraction technologies discussed above have their pros and cons when considering different process aspects, as shown in Table 2.4.

Table 2.4. Advantages, disadvantages and environmental impacts of metal extraction techniques (Garole et al., 2020; Zheng et al., 2018).

Process	Advantages	Disadvantages	Environmental impacts
Pyrometallurgy	High capacity Simple operation	High energy consumption High temperatures	Air pollution by waste gases and dust released
Hydrometallurgy	Higher purity Lower energy consumption Higher recovery	Higher chemical consumption Higher operation time	Discharge of waste liquids

Biometallurgy	Lower energy consumption Higher recovery Mild operation conditions.	Higher operation time Difficulties in growing bacteria	Discharge of wastewater
Mechanochemical	Treat waste by waste Lower operational cost	Higher capital cost Lower capacity Higher process time	Sound pollution due to noise

Therefore, a combination of technologies was used to enhance the effectiveness of the metal extraction process. A mechanochemical, more environmentally friendly process of co-grinding LiCoO₂ with EDTA in a mass ratio of 1:4 for 4 h at 600 rpm recovered 98% of Co and 99% of Li. The stable and water-soluble chelates Li-EDTA and Co-EDTA can be separated by chemical precipitation (M.-M. Wang et al., 2016). This mechanochemical process requires fewer chemicals and energy, but it has a long process time, lower capacity and high capital cost. However, hydrometallurgy is a widely used industrial application which is economically feasible (Garole et al., 2020; Piątek et al., 2020).

2.5 Metal extraction in NiMH batteries

The NiMH batteries consist of REE in addition to the metals that may be possibly present in LIB. Therefore, nickel and cobalt were extracted by acid leaching from spent NiMH batteries after separating the REE (La +Ce+ Pr +Nd) by precipitation with NaOH (Rodrigues & Mansur, 2010). According to the study by (Korkmaz et al., 2018), nickel, cobalt and REE were recovered by sulfation using 8 M H₂SO₄, selective roasting at 850 °C for 2 h and water leaching to recover 96% of REE to aqueous phase while leaving the oxides of nickel and cobalt in the solid phase.

Table 2.5 presents the techniques, leaching agents, and conditions used to obtain the recovery efficiencies of valuable metals from spent NiMH battery waste.

Table 2.5. Summary of studies on leaching of valuable metals from spent NiMH battery waste

Technique	Leaching agent	Conditions	efficiency	Reference
Leaching	H ₂ SO ₄	25°C 75 min	Co - 79.4%, Ni - 66.2%, Fe -	(Sobianowska-Turek, 2018)

			68.5%, Mn - 91.9%, Ce - 97.7%, La - 88.7%, and Zn - 100%	
Leaching and NaOH precipitation	H ₂ SO ₄	Room temperature	96% for La, Ce and Nd	(Alonso et al., 2015)
Solvent extraction	primary amine (N1923)	20°C 5 min	REE-99.98%	(XIA et al., 2015)
Leaching, oxalate precipitation and purification	HCl	70°C	REE-95.16 %	(Yang et al., 2014)
Leaching	H ₂ SO ₄	<90 °C 3 h.	Ni-99.9% and Co-99.4	(Rabah et al., 2008)

The studies conducted on the extraction of metals in NiMH batteries indicated that REE was also leached together with cobalt and nickel. A separation procedure such as selective precipitation or heating to form oxides must be carried out to separate cobalt and nickel from REE.

2.6 Separation of extracted metals

The metal extraction step is generally not selective, and it may contain various other constituents. Therefore, purification is done initially before the separation of metals. The method of recovering metals from leachate depends on leached solution properties such as composition, metal concentration and pH (Botelho Junior et al., 2019). The commonly used separation processes are adsorption (Anirudhan et al., 2019; Bożęcka et al., 2020), ion exchange (Vaughan et al., 2016; Zainol & Nicol, 2009a), chemical precipitation (Piątek et al., 2020), membrane processes (Pospiech, 2014), complexation, and electrolysis (Li Li et al., 2011).

This study focuses on solid-phase extractions, adsorption and ion exchange separation methods because of their ability to effectively extract metals at low concentrations at a reasonable cost (X. Jiang et al., 2014).

2.7 Adsorption

Adsorption is a cost-effective and efficient separation technique out of the commonly used separation technologies (Liu et al., 2019). This study is focused on adsorbing metals from the liquid phase to the solid phase. Metal ions from the liquid bulk transfer to the solid adsorbent surface via diffusion through the interfacial layer, maintaining the equilibrium between the adsorbent and liquid phases. Physical and chemical sorption determines the behaviour of the interfacial layer by forming Van der Waals and ionic or covalent bonds, respectively, between adsorbent and adsorbate. The properties of physical and chemical sorption can be analyzed further as follows in Table 2.6.

Table 2.6. Properties of chemical and physical sorption (Basuki et al., 2019)

Properties	Chemical sorption	Physical sorption
Type of bonding	Ionic and covalent	Van Der Waals
Adsorption heat	20-400 kJ/mol	1-40 kJ/mol
Reversibility	Irreversible	Reversible
Activation energy	High	Low
Effect of temperature	Some positive cases	Negative
Formation of layers	Monolayer	Monolayer or Multilayer

The adsorption process is considered to be spontaneous. Hence Gibb's free energy is negative, and the thermic nature is mostly exothermic but can also be endothermic depending on the interactions (Ji et al., 2022). The factors such as pH, contact time, solid-liquid (adsorbent-adsorbate) ratio, and temperature govern the adsorption efficiency (Ugwu et al., 2020). Therefore, experiments were conducted on determining the effect of the above factors.

2.7.1 Selection of adsorbents

Adsorption highly depends on the type of adsorbent used. Even though there are many different adsorbents, still there is a demand for a more efficient, stable, selective and cost-effective material. MOFs have a porous structure facilitating structural modifications in pore size,

dimensions, shape, and functionality to form active adsorption sites, as shown in Figure 2.3 (Uemura et al., 2009). Therefore, in this study, several structural modifications were done to MOF-808 to vary the above parameters to change the properties of adsorption. Resin, Amberlite IRC-748, which is well known for heavy metal removal, was also used in this study to identify the best pathway to adsorb Ni²⁺ or Co²⁺ ions selectively.

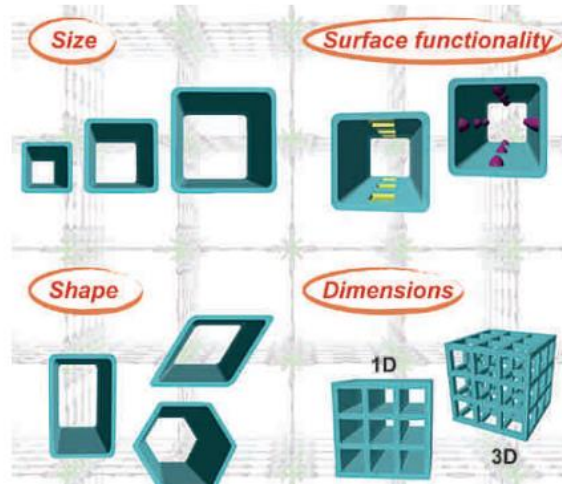


Figure 2.3. Structural modifications forming active sites (Uemura et al., 2009)

2.8 Batch adsorption experiments

Batch adsorption experiments were initially conducted to determine the properties such as adsorption capacity, removal efficiency and other parameters such as optimum pH, temperature, liquid-solid ratio, and contact time. The easy and fast operation in low sample quantities makes batch adsorption the preliminary step in the scale-up of the adsorption processes (Marzbali & Esmaili, 2017).

2.8.1 Adsorption isotherms

The adsorption isotherms depict the adsorption capacity with the equilibrium concentration of the adsorbate. Thus it gives an overview of the maximum adsorption capacity for the adsorbate and the adsorbent. The amount of metal ions adsorbed per unit mass of adsorbent, q (mg g⁻¹), is given by equation 1 below

$$q = \frac{(C_0 - C_e)V}{m} \quad (1)$$

where m (g) is the mass of adsorbent, V (L) is the volume of the solution, C_0 and C_e are the metal ion concentration before and after adsorption (mg L^{-1}), respectively.

Langmuir and Freundlich adsorption models were the models widely used to analyze the adsorption isotherms by curve fitting. The Langmuir model was proposed based on the adsorption occurring on a homogeneous surface in a monolayer, while the Freundlich model facilitates more than one layer with the heterogeneous surface (Liu et al., 2019). The Langmuir and Freundlich model equations are indicated in equations 2 and 3, respectively.

$$q_e = \frac{k_1 q_m C_e}{1 + k_1 C_e} \quad (2)$$

$$q_e = K_f C_e^{\frac{1}{n}} \quad (3)$$

The linear formats of the Langmuir and Freundlich model equations are indicated in equations 4 and 5, respectively.

$$\frac{C_e}{q_e} = \frac{C_e}{q_m} + \frac{1}{q_m K_1} \quad (4)$$

$$\ln q_e = \ln K_f + \frac{1}{n} \ln C_e \quad (5)$$

Where q_e (mg g^{-1}) is the adsorption capacity at equilibrium, q_t (mg g^{-1}) is the amount of adsorbed metal ions at time t , t (min) is adsorption contact time, q_m (mg g^{-1}) is the maximum adsorption capacity, C_e (mg L^{-1}) is the equilibrium concentration of metal ions, K_1 (L mg^{-1}) is the Langmuir adsorption constant, K_f ($\text{mg g}^{-1}(\text{L mg}^{-1})^{1/n}$) is the Freundlich isotherm constant, and n is the adsorption intensity.

2.8.2 Adsorption kinetics

Adsorption kinetics experiments were conducted to determine adsorption rate and the time taken to reach the adsorption equilibrium. The adsorption kinetics were determined by curve fitting using model equations 6 and 7 for pseudo-first and pseudo-second order, respectively.

$$\ln(q_e - q_t) = \ln q_e - k_1 t \quad (6)$$

$$\frac{t}{q_t} = \frac{1}{k_2 q_e^2} + \frac{1}{q_e} t \quad (7)$$

Where k_1 (min^{-1}) and k_2 ($\text{g mg}^{-1} \text{min}^{-1}$) are the pseudo-first and pseudo-second order rate constants, respectively

2.9 Selectivity in adsorption

The selectivity plays a key role in adsorption based metal recoveries. The black mass leachate consists of a mixture of several metals. Therefore, to recover a metal, adsorbents which selectively adsorb the required metal is necessary. Therefore, in this study a selectivity factor was used to present the selectivity in a quantitative manner as shown in equation 8.

$$\text{Selectivity } i \text{ relative to } n = \frac{\text{Adsorption capacity of metal of concern}(i)}{\text{Adsorption capacity of reference metal}(n)} \quad (8)$$

Hence, the equation 9 was used when evaluating the results.

$$\text{Selectivity of } Ni^{2+} \text{ relative to } Co^{2+} = \frac{\text{Adsorption capacity of } Ni^{2+}}{\text{Adsorption capacity of } Co^{2+}} \quad (9)$$

The selectivity can vary depending on the adsorbate solution pH, contact time during the adsorption, and the properties of adsorbents such as pore size and type of active functional groups.

2.10 Column adsorption experiments

Column adsorption experiments are conducted with a continuous fluid flow, loading the adsorbents fully with adsorbate while adsorbents in batch adsorption are in equilibrium with the residual concentration of the metals in the solution. The special feature of column adsorption is that in the initial period of the process, there is nearly zero adsorbate concentration in the fluid flowing out (Dichiara et al., 2015).

According to Figure 2.4, the mass transfer zone (MTZ) is at the top of the column bed. MTZ moves down the column with the saturation of the column's upper region, resulting in an increased adsorbate concentration in the column outflow from the initial zero concentration. The breakthrough point is selected arbitrarily at a point before the sudden increase in adsorbate's relative concentration.

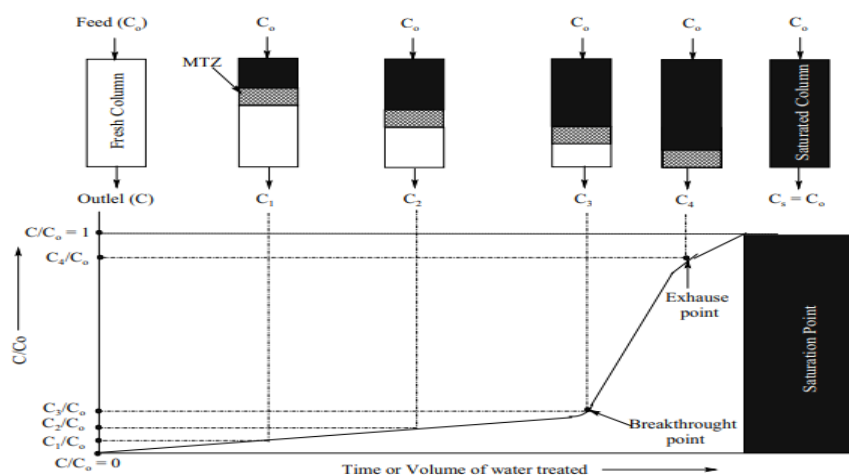


Figure 2.4. Breakthrough curve with the movement of MTZ (Patel, 2019)

In practical applications, the column adsorption is stopped at the breakthrough point, and the adsorbent is regenerated for the next adsorption cycle. Hence the full bed capacity is not used in the adsorption. The length of the unused bed (LUB) is thus calculated, which is the equivalent height of the original bed with the same capacity as the unused region of the column bed.

2.11 Resins as adsorbent and ion exchanger

The resins have become the widely used adsorbent due to the ability to effectively exchange mobile ions with equally charged ions contained in the medium (Botelho Junior et al., 2019; X. Jiang et al., 2014). Therefore, the resins are considered the agent to separate the leached metals in this section.

Equation 10 represents an ion exchange reaction, where the cationic resin exchanges the cation X^+ in the functional group with the cation M^+ present in the solution. Similarly, the anionic resins exchanges with anions present in the solution.



The characteristics of resins are determined by the functional groups present. The four main types of resins are strongly acidic, weakly acidic, strongly basic, and weakly basic, which differ in functional groups. There are ligand exchange resins known as chelating resins in the subcategory of ion exchange resins. The chelating resins consist of functional groups of atoms consisting of nitrogen, oxygen, sulphur and phosphorous. Their lone pair electrons are attracted to transition metal ions by coordination bonds and the electrostatic interactions of the general ion exchange resins. Therefore, the metal selectivity is higher in chelating resins than in the other general resins (Botelho Junior et al., 2019; Zainol & Nicol, 2009b).

After removal of interfering metals, Co^{2+} was selectively recovered from a binary mixture of Co^{2+} and Ni^{2+} by chromatographic operation through solvent impregnated resin (SIR) with PC-88A and Cyanex 272 at lower concentrations of Ni^{2+} (F. Guo et al., 2013). However, Cyanex 272 was preferred over PC-88A even though it is expensive due to high selectivity towards Co^{2+} to separate Co^{2+} from a binary mixture of Co^{2+} and Ni^{2+} (F. Guo et al., 2012). An acid such as HCl can be used to elute the adsorbed Co^{2+} from the resins (X. Jiang et al., 2014).

According to the study by (Mendes & Martins, 2004), commercially available resins such as Dowex M4195, Ionac SR-5, Amberlite IRC748 and Purolite S930 showed higher selectivity for copper. Nickel can be extracted as the second highly selective metal by optimizing pH,

contact time, initial metal concentration, and nickel to cobalt concentration ratio. Dowex M4195R was able to recover nickel and cobalt equally in pH range 1-3 with a less impact from other elements. A chelating resin made by coupling Amberlite XAD-2 by an azo spacer with salicylic acid showed a Co^{2+} sorption capacity of 87.4 mg g^{-1} at an optimum pH of 7.5. The resin was reused without a considerable loss of sorption capacity for 20 cycles of sorption – desorption. The elution was conducted by 0.5 M HNO_3 , which yielded 95.3 % recovery (Panahi et al., 2012).

The commercially available iminodiacetic chelating resins with sodium ionic form are compared in Table 2.7 (Zainol & Nicol, 2009a).

Table 2.7. Properties of commercially available iminodiacetic chelating resins

Description	Amberlite IRC 748	Lewatit TP 207	Lewatit TP 208	Lewatit TP 207 Monoplus	Purolite S 930
Source	Rohm and Haas, USA	Lanxess, Germany	Lanxess, Germany	Lanxess, Germany	Purolite, UK
Matrix	Styrene	Styrene	Styrene	Styrene	Styrene
Structure	Macroporous	Macroporous	Macroporous	Macroporous	Macroporous
Bead size (mm)	0.3-1.1	0.4-1.25	0.4-1.25	0.61 ± 0.05	0.14-0.52
Bulk density (g L^{-1})	685-760	800	800	750	710-745
Total capacity (eq L^{-1})	1.25	2.4	2.7	2.0	1.1
Operating pH	1.5-14	0-14	0-14	0-14	2-6

The performance of these resins differs in kinetics due to the variations of matrix structure, crosslinking, functional group density, particle sizes, and iminodiacetate group proportion. The Amberlite IRC 748 and TP 207 Monoplus were proposed as the best resins in terms of

adsorption capacity for nickel and adsorption kinetics, even though they have a lower theoretical capacity. Therefore, it will reduce resins' inventory and cost, making it the better choice for lower residence time applications (Zainol & Nicol, 2009a). (Mendes & Martins, 2005) presented that Amberlite IRC 748 recovered 99% nickel and cobalt from acid leach pulp at pH 4 and 60 °C in 45 min.

According to the studies, the chelating resins, Amberlite IRC 748, Dowex M4195R and TP 207 Monoplus were highlighted as the resins with the potential of selectively recovering cobalt and nickel from the leachate.

A summary of the state of the art of metal uptakes by resins is indicated in Table 2.8.

Table 2.8. Studies conducted on metal uptake by resins

Resin	Conditions	Maximum capacity (mg g ⁻¹)	Metal	Reference
D113-III resin (polymeric material containing a functional group (-COOH))	pH = 6.5 298 K.	192.1	Co ²⁺	(X. Jiang et al., 2014)
SIR containing PC-88A	pH = 3.8 298 K.	20.63	Co ²⁺	(F. Guo et al., 2012)
SIR containing PC-88A	pH = 4.0 298 K.	19.95	Ni ²⁺	(F. Guo et al., 2012)
SIR containing Cyanex 272	pH = 5.5 298 K.	29.47	Co ²⁺	(F. Guo et al., 2012)
SIR containing Cyanex 272	pH = 6.8 298 K.	28.76	Ni ²⁺	(F. Guo et al., 2012)
Amberlite IRC 748	pH = 3 [Ni]/[Co]=5	102.71 14.73	Ni ²⁺ Co ²⁺	(Mendes & Martins, 2004)
Amberlite XAD-2 with salicylic acid	pH = 7.5	87.4	Co ²⁺	(Panahi et al., 2012)
Amberlite IRC 748	pH = 7.5	97.6	Ni ²⁺	(Mendes & Martins, 2005)

The D113-III resin has resulted in the highest metal uptake capacity, but the experiment was carried out for an aqueous solution containing only the Co^{2+} . The other experiments were conducted in the presence of competing ions, where lower metal uptake values have resulted. Therefore, it is necessary to focus on the metal selectivity of the resins when more than one metal is present in the solution. Amberlite IRC-748 was selected for the analysis in this study due to the recorded selectivities and significant metal uptake capacities.

2.11.1 Amberlite IRC 748 resin

The chelating resins consist of functional groups of atoms consisting of nitrogen, oxygen, sulphur and phosphorous. Their lone pair electrons are attracted to transition metal ions by coordination bonds and the electrostatic interactions of the general ion exchange resins. Therefore, the metal selectivity is higher in chelating resins than in the other general resins (Botelho Junior et al., 2019; Zainol & Nicol, 2009b). A commercial chelating resin Amberlite IRC 748, supplied by Thermo scientific, was used in this study. The properties of Amberlite IRC 748 resin are summarized in Table 2.9.

Table 2.9. Properties of Amberlite IRC-748

Physical form	Beads
Density	0.7500 g/mL
Mean Particle size	0.500 - 0.650 mm
Ionic form as shipped	Na
Moisture holding capacity	60-65%
Volume cation Capacity	1.35 eq/L

The resin Amberlite IRC 748 comprises styrene divinyl-benzene chains with anchored iminodiacetic acid (IDA) as a functional group. Thus it has three donor atoms of amino nitrogen and two carboxylic oxygens, which can form coordinate bonds, as shown in Figure 2.5 (Zainol & Nicol, 2009b).

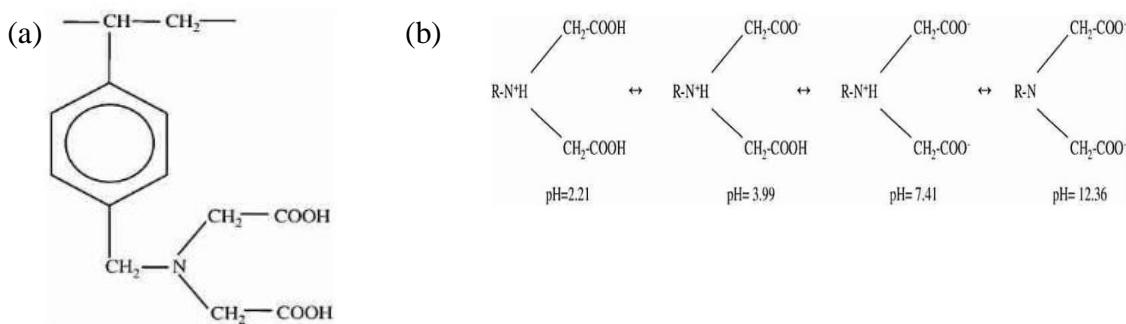
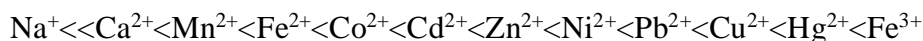


Figure 2.5. Amberlite IRC-748 (a) Chemical structure and (b) pH vs stability of Amberlite IRC 748 (Zainol & Nicol, 2009b)

According to Figure 2.5 (b), at pH values below 2.21, the resin is fully protonated, most likely obtained after acid conditioning to remove impurities. When the resin is washed with high pH distilled water, the first, second and third protons are neutralized at pH values of 3.99, 7.41 and 12.36, respectively.

According to the technical datasheet by Lenntech, the selectivity order of Amberlite IRC 748 for metals is as follows;



The affinity for H^+ is known to be in between Pb^{2+} and Cu^{2+} at pH 4. Therefore, the metals Ni^{2+} , Co^{2+} and Mn^{2+} will remove efficiently only at a pH above 4. Fe^{2+} and Cu^{2+} will be more selective and removed effectively at low pH values around 2.

2.11.2 Resin ion exchange

The metal sorption by the resin is denoted in equation 11 (Mendes & Martins, 2004):



Where M and R represent metal and resin, respectively, the selectivity of the exchanging metal ion species can be difficult to predict in the presence of interfering metal ions in the black mass leachate solution. However, studies conducted by (Mendes & Martins, 2004) have indicated the selectivity of Ni^{2+} over Co^{2+} in a simulated solution.

2.12 Metal-organic frameworks

Metal-organic frameworks (MOFs) are a class of porous crystalline materials known for their large surface area exceeding $6000 \text{ m}^2 \text{ g}^{-1}$, adjustable surface properties and tunable pore size (Zhou et al., 2012). It consists of inorganic metal ions or clusters and organic linkers connected using coordination bonds (Farha & Hupp, 2010). Studies on MOFs and the predictions of their

structure have paved the way for the development of their reticular chemistry. These properties of MOFs lead to applications such as separation of molecules, gas storage, chemical catalysis, chemical sensing, ion exchange, and drug delivery (Farha & Hupp, 2010).

The MOFs are formed into a crystalline structure by joining metals which are inorganic secondary building units (SBUs), using organic linkers, which are the nodes of the cluster. A vast number of SBU and linker combinations are identified to be possible to form with diverse properties physically and chemically (Øien-Ødegaard et al., 2017). A modulator is used in excess to slow down the synthesis to obtain good quality and controlled crystal growth (Gutov et al., 2016).

2.12.1 Zirconium based MOFs

The discovery of UiO-66 MOF paved the way to focus more on Zr- MOFs with large surface area and unprecedented stability (Cavka et al., 2008). The bond strength between the linker and the inorganic metal determines the stability. The Zr-MOFs have gained more stability due to their structure, where each metal unit is connected by 12 ditopic linkers. The deviations from the saturated 12 –coordinated SBU lead to catalytic and adsorptive properties in MOFs due to vacant and accessible metal sites (Aunan et al., 2021). The defect-free structures of UiO-66, NU-1000 and MOF-808 are illustrated in Figure 5, where zirconium, oxygen and carbon are indicated by green, red and grey, respectively, in the Figure 2.6.

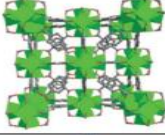
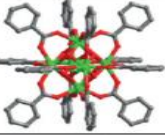
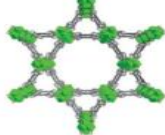
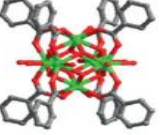
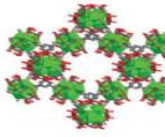
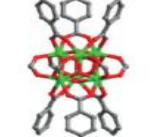
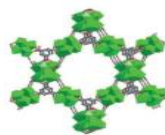
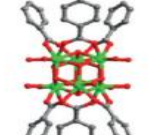
MOF and formula ¹⁴¹ (connectivity of the nodes)	Structure	Node
UiO-66 $Zr_6(\mu_3-O)_4(\mu_3-OH)_4(BDC)_6$ (12-connected)		
NU-1000 $Zr_6(\mu_3-O)_4(\mu_3-OH)_4(OH)_4(H_2O)_4(TBAPy)_2$ (8-connected)		
MOF-808-as synthesized $Zr_6(\mu_3-O)_4(\mu_3-OH)_4(HCOO)_6(BTC)_2$		
MOF-808-activated $Zr_6(\mu_3-O)_4(\mu_3-OH)_4(OH)_6(H_2O)_6(BTC)_2$ (6-connected)		

Figure 2.6. Structures and formulas of common zirconium MOFs (Moon et al., 2015)

The MOF-808 considered in this study is 6 coordinated. Hence it has structural vacancies to incorporate post-synthetic functional groups to enhance adsorption properties. MOF-808 was first synthesized in a study on water adsorption in porous materials (Furukawa et al., 2014). MOF-808 has an octahedral crystal structure connected with tritopic Benzenetricarboxylic (BTC) as the linker. The inorganic SBUs are connected with 6 linkers, and each linker is connected to 3 SBUs. The modulator anions used complete the coordination by connecting 6 modulator ligands to the SBU and balancing the charge. Thus, MOF-808 is comprised of a three-dimensional framework with a 6,3 connected spn topology (Furukawa et al., 2014).

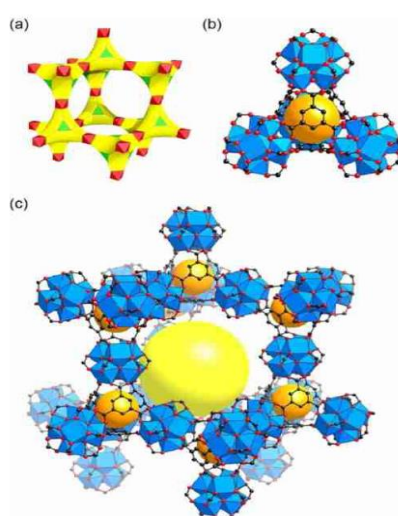


Figure 2.7. MOF-808 structures (a) octahedral and triangular units (b) large adamantane pore in orange (c) Atomic structure C, black: O, red: Zr, blue: yellow and orange are pores (Furukawa et al., 2014)

As shown in Figure 2.7, there are two types of pore shapes in MOF-808: a pore within each tetrahedral unit and a large adamantane pore. This geometry directs each ligand pointing towards the large pore. The ligand positions in the MOF-808 structure provide space for new functional groups by solvent assisted ligand exchange (SALE) and facilitates guest molecules. Thus the MOF-808 has been studied with various incorporated functional groups from its first synthesis based on functionalities such as superacidity (J. Jiang et al., 2014) and proton conductivity (Meng et al., 2019). Due to the diverse applications, the MOF-808 class is selected to experiment with metal adsorption capacities by introducing different potential functional groups in this study.

2.12.2 MOF-808 and its functionalized analogues

MOF-808 has diverse properties based on the non-structural ligands. Figure 2.8 shows the composition and structures of the MOF-808 family members. The spheres in orange and yellow indicate the void spaces, zirconium in blue, carbon in black and oxygen in red.

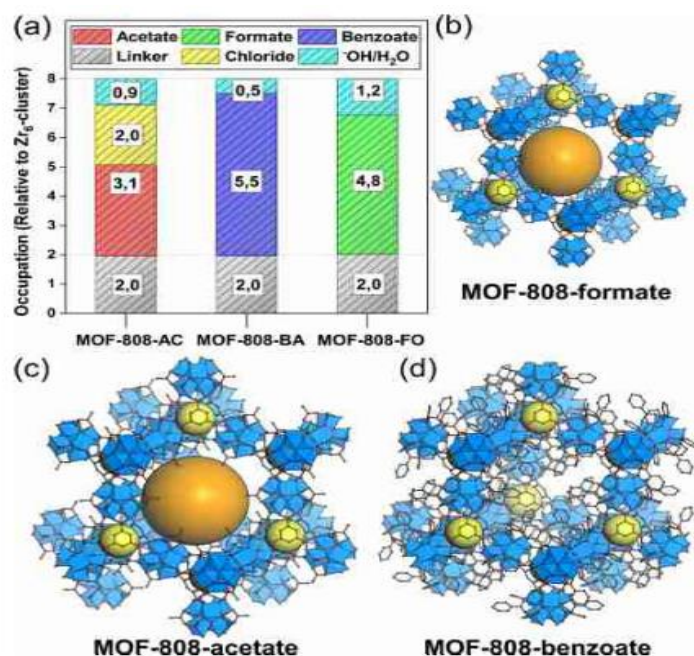


Figure 2.8. (a) MOF-808 composition indicating linker, modulator and solvent. Structures of (b) MOF-808-formate (c) MOF-808-acetate (d) MOF-808-benzoate (Aunan et al., 2021).

The phenyl group in MOF-808-benzoate changes the properties such as hydrophobicity, surface area and capacity. The large phenyl groups have reduced both surface area and capacity compared to the MOF-808-acetate.

2.12.3 Metal adsorption by MOF-808

MOF-808, selected in this study as the adsorption material, has excellent stability, high adsorption capacity, and is easily modifiable with functional groups according to the previous studies. Ethylenediaminetetraacetic acid (EDTA) grafted MOF-808 was one of the interesting functionalized analogues of MOF-808 which showed a higher removal efficiency and adsorption capacity in the previous studies (Xinyu Chen et al., 2020; Y. Peng et al., 2018). . EDTA has six binding sites including four carboxyls and pair of tertiary amine groups as shown in Figure 2.9 which allows it to bind with various heavy metal species. Therefore, MOF-808

EDTA was synthesized in the study by immobilizing EDTA on porous MOF-808 to enhance the active sites for metal capture.

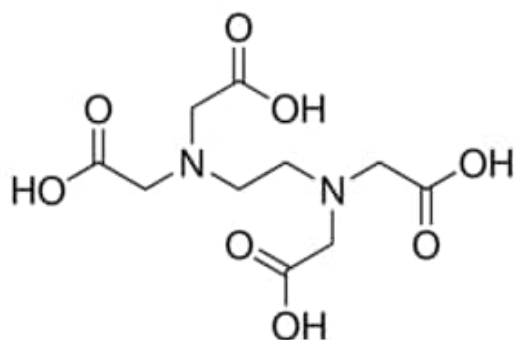


Figure 2.9. Structure of EDTA

The existing MOF based adsorbents have some drawbacks in performance due to their low density and improper functional group distribution, which affects affinity towards metals and the metal uptake capacity. As a solution to this issue, Peng et al. suggested a broad-spectrum heavy metal ion trap (BS-HMT) which has the properties such as high metal affinity by strong metal chelation, highly loaded chelating group distribution at the atomic level, ensuring properly distributed high-density active sites for binding, and multiple-use by regeneration by washing with EDTA-2Na (Y. Peng et al., 2018). Figure 2.10 illustrates the concept of BS-HMT graphically.

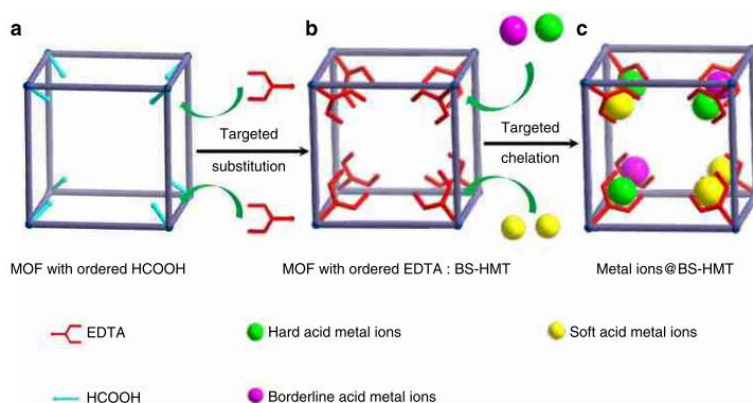


Figure 2.10. Concept of BS-HMT for MOF-808-EDTA

In order to compare the properties and performance, 3,4-dihydroxybenzoic acid and 3,5-diaminobenzoic acid were also considered for grafting into MOF-808. Figure 2.11 shows the arrangement of carboxyl, hydroxyl and amino groups in the phenyl ring which acts as binding sites in the grafted MOF-808.

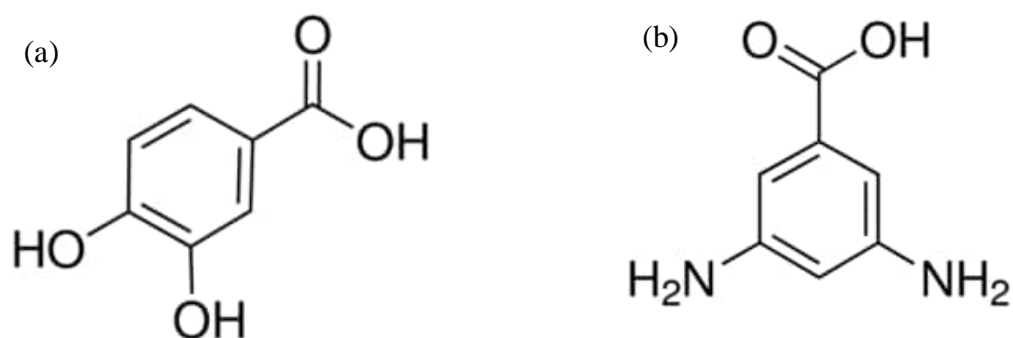


Figure 2.11. Functional groups in the structures of (a) 3,4-dihydroxybenzoic acid (b) 3,5-diaminobenzoic acid

The previous adsorption studies conducted on adsorption recovery of metals using MOF-808 and its functionalized analogues are shown in Table 2.10.

Table 2.10. Studies on adsorption recovery of metals using MOF-808

Material	Mass of adsorbent (mg)	Adsorbate volume (mL)	Metal concentration	Adsorption capacity/efficiency	Reference
MOF-808-EDTA	95	10	19 heavy metals- 5 mg/L	>99 %	(Y. Peng et al., 2018)
MOF-808	20	30	Cd, Zn -20 ppm	Cd- 225.05 mg/g Zn-287.06 mg/g	(Efome et al., 2018)
MOF-808-SH (thioglycollic functionalized)	MOF-808-SH 10	50	Hg- 5-200 mg/L	977.5 mg/g	(Ji et al., 2022)
MOF-808	10	50	As-5 mg/L	24.83 mg/g	(Li et al., 2015)
MOF-808	500	100	Hg -200 mg/L	343.6 mg/g	(Liu et al., 2019)
MOF-808	10	20	Pd- 10, 500 mg/L	163.9 mg/g	(Lin et al., 2019)

The MOF synthesis is often associated with defect engineering, which engineers the defects due to missing ligands and clusters. These defects can lead to enhanced adsorption capacity in MOFs due to the opening up of metal sites and yielding large pore sizes in case of missing ligand and cluster, respectively (Winarta et al., 2020). Figure 2.12 illustrates these effects graphically.

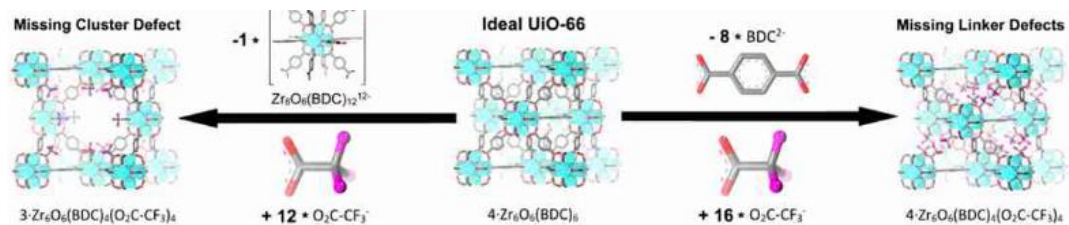


Figure 2.12 – Missing cluster and missing linker defects (Winarta et al., 2020)

However, these defects adversely affect reducing the stability of the MOFs, lowering crystallinity and increasing hydrophilicity (Shearer et al., 2016; Winarta et al., 2020). Therefore, it is not reliable to depend on MOF defects to enhance the adsorption capacity.

2.13 Proposed process flow for the recovery process

The proposed recovery process based on the studies is shown in Figure 2.13.

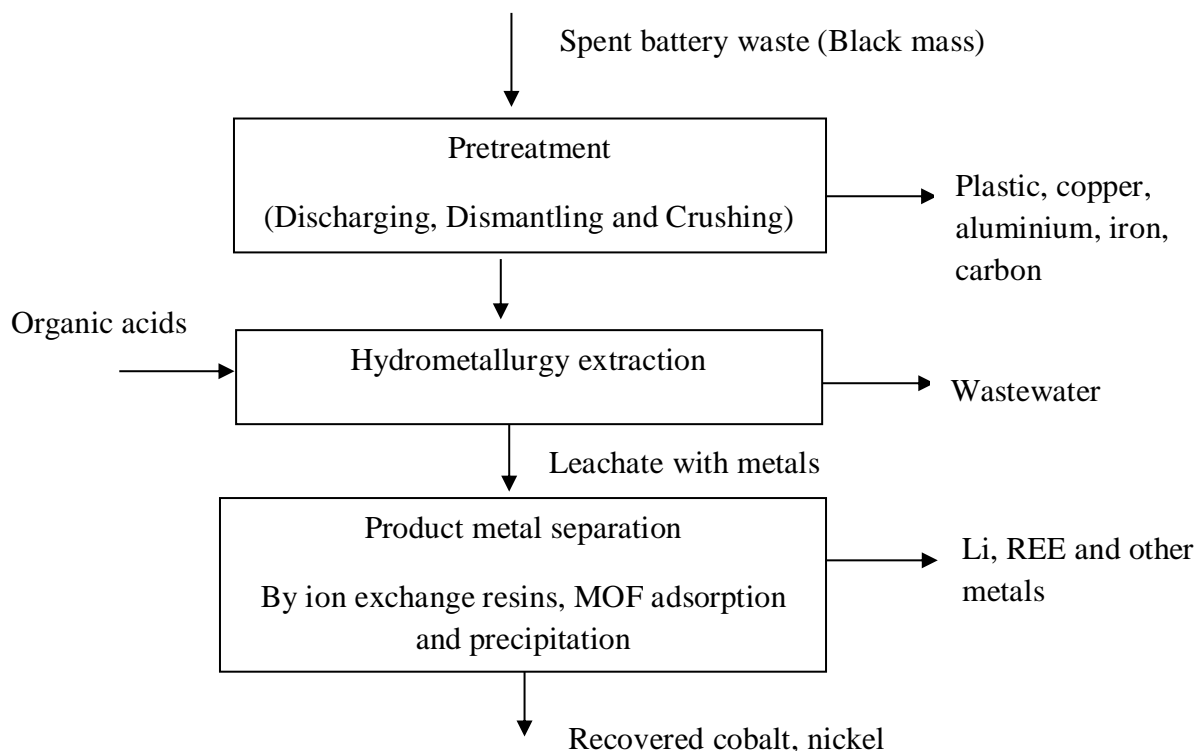


Figure 2.13 Proposed process flow diagram for nickel and cobalt recovery

2.14 Research gap

Recovery of metals from spent battery waste electrode materials is a timely topic of interest. Much research has been conducted to leach and recover most of the elements from the electrode material. The leaching efficiencies reached 100 % at optimized conditions, but the separation efficiencies of the metals such as cobalt, nickel and manganese from the leachates are still at a lower level. The studies and processes are focused on cathode metal recycling by impurity removal in the black mass, but it ends up in cathode materials with different compositions and electrochemical performance. Therefore, the research area to investigate an efficient, environmentally sustainable metal recovery process to provide raw materials to synthesize a high-quality cathode material is still an open and challenging study to work on.

2.15 Objectives of the study

The objectives of the Master's thesis were formulated by the research gap identified to separate the black mass metal leachate efficiently.

1. Investigating the potential of MOF-808 and its modified groups in selectively uptaking the cobalt and nickel from the black mass metal leachate solution.
2. Investigating the potential and properties of the resin Amberlite IRC 748 as an adsorbent in selectively uptaking cobalt and nickel from black mass metal leachate solution.
3. Characterizing MOF-808 and Amberlite IRC-748.
4. Black mass composition analysis and metal leaching using an efficient and environmentally benign leaching media.

3. MATERIALS AND METHODS

Experiments in laboratory scale were conducted to investigate the efficacy of resin Amberlite IRC-748 and functionalized MOF-808 in recovering Nickel and cobalt from the black mass metal leachate solution. The experiments of synthesizing MOF-808, characterizing, and analyzing metal recovery methods were carried out in the university laboratories.

3.1 Materials

A thermally treated black mass containing both cathode and anode material was provided by Glencore Nikkelverk AS. Phosphoric acid (85 %, Supelco), citric acid monohydrate (VWR) and tartaric acid ($C_4H_6O_6$, 99.5%, Merck) were used as leaching agents, Hydrochloric acid (35.7 %, VWR) and Nitric acid (65 %, Supelco) for digestion solution, and H_2O_2 (35 %, Merck) as the reducing agent. The resin Amberlite IRC 748 in sodium form was purchased from Thermo scientific, and MOF-808 and its functionalized analogues were synthesized in the laboratory and were used as the adsorbents. Trimesic acid (H_3BTC , 95%, Sigma Aldrich), Zirconyl chloride octahydrate ($ZrOCl_2 \cdot 8H_2O$, 98%, Sigma Aldrich), acetic acid, 3,4-dihydroxybenzoic acid ($C_7H_6O_4$, 98%, Tokyo Chemical Industry), 3,5-diaminobenzoic acid ($C_7H_8N_2O_2$, 98%, Thermo scientific), Ethylenedinitrilotetraacetic acid-EDTA ($C_{10}H_{16}N_2O_8$, Supelco) were used in the synthesis of MOF-808 and its functionalized analogues. Sulphuric acid (90-91%, Supelco) was used for resin pretreatment and elution. NaOH (98.7 %, VWR) and HCl (35.7 %, VWR) were used for the pH adjustments. The simulated metal solutions were prepared from the chemicals $NiCl_2 \cdot 6H_2O$, $CoCl_2 \cdot 6H_2O$, $MnCl_2 \cdot 4H_2O$ and LiCl in solid form.

3.2 Characterization methods

The characterization method's conditions and procedures are explained in detail with a brief summary of the theoretical background related to the analysis.

3.2.1 X-ray powder diffraction (XRD)

XRD was used to analyze the material crystallinity and especially to confirm the crystallinity of newly synthesized MOF by comparing it with known samples. The principle of the analysis is constructive interference of monochromatic X-rays when conditions of Bragg's law ($n\lambda = 2d \sin \theta$) is satisfied. The cathode ray tube generated X-rays are filtered into monochromatic radiation, concentrated by collimation and directed to the sample. The sample is scanned along with a range of 2θ angles, and the diffracted X-rays are detected and counted to produce the intensity values with the 2θ angle.

The procedure for conducting XRD analysis was as follows. Samples were finely ground using a mortar and pestle. Samples with a quantity of more than 0.5 g were used in powder form and placed on a sample holder (PMMA, 8.5 mm height, and Ø 25 mm sample reception). Powdered samples were distributed evenly on the sample holder using a blade and sample surface was smoothed using a thin glass plate. Samples with a lower quantity were made into a slurry using ethyl alcohol, added dropwise to the sample holder (Ø 51.5 mm, Ø 24.5 mm Si crystal), and dried until a thin powder film was formed. The sample holders were mounted on the sample stage of D8 Advance- Bruker XRD and scanned from 2° to 70° 2θ with a scan speed of $5.77^{\circ} \text{ min}^{-1}$ for short-run and $1.19^{\circ} \text{ min}^{-1}$ for the long run. The analysis was conducted using a radiation source of Cu-K α of a wavelength of 1.5418 Å. A voltage of 40 kV with a current of 25 mA was used to energize the X-ray tube. The data was obtained in XY-file format and plots were prepared using QtiPlot.

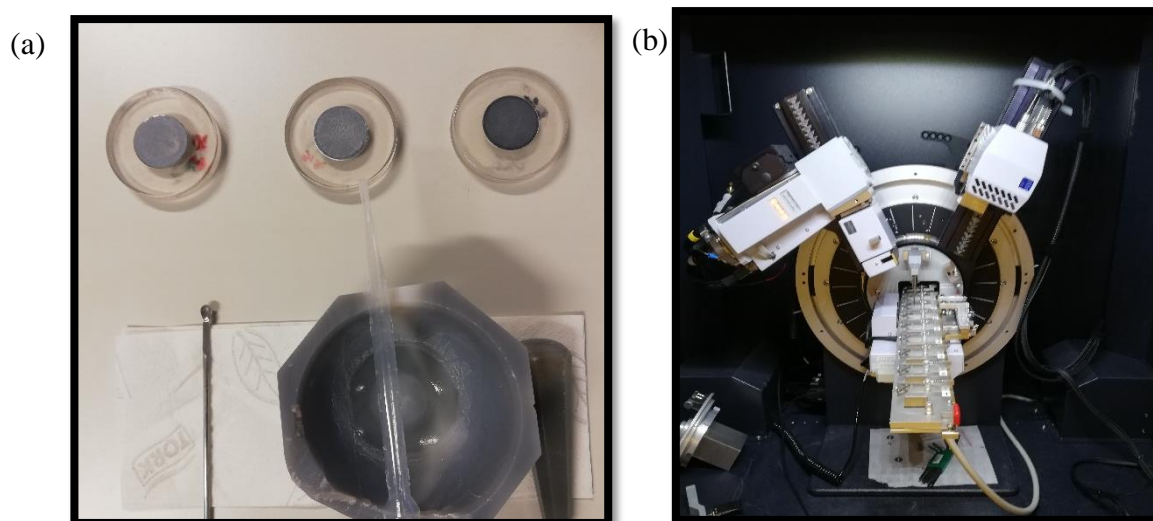


Figure 3.1. (a) Slurry form XRD sample preparation (b) XRD instrument

3.2.2 Thermogravimetric Analysis (TGA)

TGA analysis was performed to identify the thermal behaviour of properties such as the mass of the sample by using Mettler Toledo TGA/DSC 3+ STARe system by varying the sample temperature. The sample mass variation with temperature is useful in determining the sample moisture content, component decompositions and removals.

The procedure for conducting TGA analysis was as follows. First, the empty 70 μL alumina oxide crucible was placed on the sample position and tared. Approximately 20 mg of sample were placed into the alumina crucible. The sample surface in the alumina crucible was levelled and packed by tapping the crucible on a table. The analysis was conducted at a heating rate of $5^{\circ} \text{ C min}^{-1}$ from 25° C to 900° C in 20 mL min^{-1} synthetic airflow. The first weight measurement

was taken as the sample weight. The data was obtained in XY-file format and plots were prepared using QtiPlot.



Figure 3.2. TGA instrument showing sample positions

3.2.3 Attenuated Total Reflection- Infrared spectroscopy (ATR-IR)

ATR-IR spectra were collected to analyze functional groups with Agilent Cary 630 ATR-IR Spectrometer. It quantifies the change in the internally-reflected infrared beam after contact with the sample. A high refractive index crystal with a set angle creates the evanescent wave that reaches the sample. This wave gets attenuated when the sample absorbs energy from the region of IR. The IR beam passes through the opposite end of the crystal, where a detector records the signals to generate the IR spectrum.

The procedure for conducting TGA analysis was as follows. Before each measurement, a blank background spectrum was obtained on the cleaned crystal surface. A small quantity of finely ground powdered samples was placed on the crystal. After recording the spectra, the crystal surface was cleaned with soft paper. The reflectances were recorded from wavenumbers 600 cm^{-1} to 4000 cm^{-1} , and the data was obtained in .xls format and plots were prepared using QtiPlot.



Figure 3.3. ATR-IR instrument

3.2.4 Scanning electron microscope-energy dispersive spectrometer (SEM-EDS)

The particle morphology and elemental composition of the samples were analyzed with SEM, Gemini SUPRA 35VP (ZEISS) (Carl Zeiss, Jena, Germany) with EDAX energy dispersive X-ray spectroscopy (EDS). SEM-EDS analysis is a non-destructive analytical technique where the sample is irradiated with electrons to emit the characteristic X-rays of the elements. The emitted energies are depicted in a spectrum with peaks indicating the intensity of elements.

The procedure for conducting the analysis was as follows. The finely ground samples were pasted on a carbon tape fixed on the sample holder. The samples were placed in the instrument and examined using SEM under a magnification of 500- 5000, and several spots and areas were analyzed for elemental composition using EDS. The SEM and EDS data were obtained in the image file and doc file format, respectively.

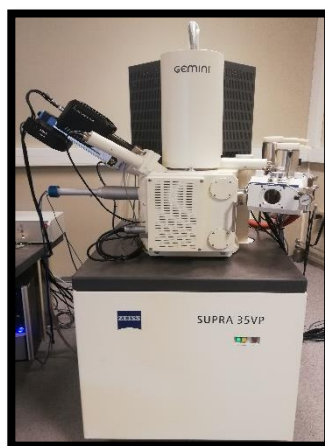


Figure 3.4. SEM-EDS instrument

3.2.5 Nitrogen sorption at 77 K

Nitrogen sorption was performed to analyze the surface area by Micromeritics TriStar II Plus. The analysis is carried out by measuring nitrogen uptake at 77 K with the increasing relative pressure upto 1 bar. The surface area was calculated using BET theory. Due to the weak interaction of gases and solids, the solid to be analyzed is cooled using a cryogenic liquid such as liquid nitrogen.

Figure 3.7 indicates the gas adsorption isotherms that can be commonly observed depending on the physicochemical conditions of the interactions.

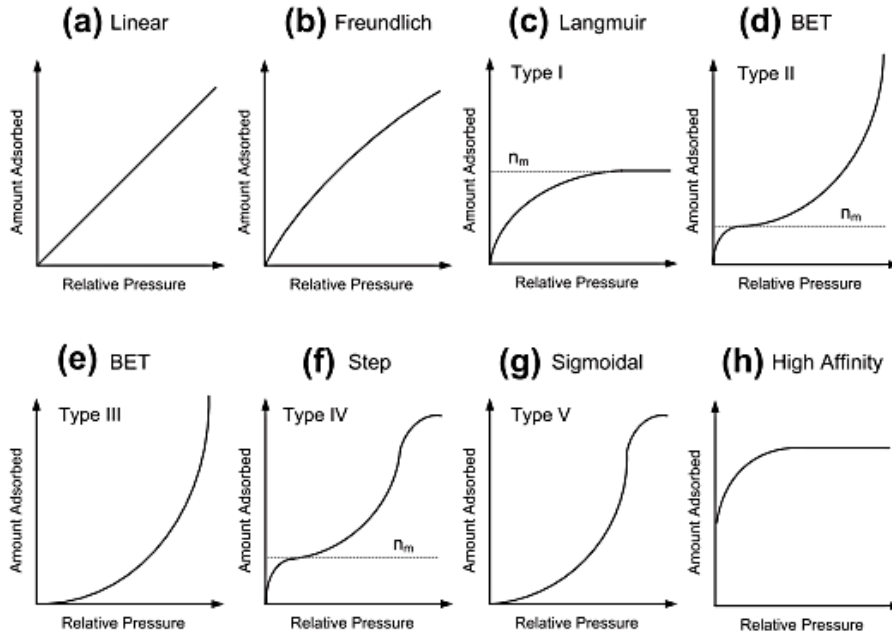


Figure 3.5. Types of adsorption isotherms (Naderi, 2015)

The isotherms depicted by type I-V are classified as IUPAC gas adsorption isotherms. The linearized BET equation as shown in equation 12 was used to calculate the BET surface area from the nitrogen adsorption isotherm.

$$\frac{\left(\frac{P}{P_0}\right)}{V_a \left(1 - \frac{P}{P_0}\right)} = \frac{c-1}{V_m c} \left(\frac{P}{P_0}\right) + \frac{1}{V_m c} \quad (12)$$

Where P and P_0 are the equilibrium and saturation pressure of the adsorbate, respectively. V_a is the amount of gas adsorbed in $\text{cm}^3(\text{STP}) \text{g}^{-1}$. V_m is the volume of gas required to form a monolayer on the adsorbent in $\text{cm}^3(\text{STP}) \text{g}^{-1}$. C is the BET constant.

The selection of the relevant relative pressure range is critical when plotting the linearized BET curve. The criteria considered by previous studies were as follows.

Selected pressures should be in the range where $V_a \left(1 - \frac{P}{P_0}\right)$ shows a continuous increment as a function of relative pressure $\left(\frac{P}{P_0}\right)$. The monolayer forming relative pressure should be within the selected relative pressure range. The BET constant calculated from the linear plot must be positive. The relative pressure range thus obtained according to the above criteria is optimized to get the highest correlation factor (R^2) which gives the best linear fit for the linearized BET curve (Shearer et al., 2016).

Monolayer volume and the BET constant are calculated from the gradient and intercept of the linearized BET curve, and the BET surface area is finally calculated from the equation 13.

$$\text{BET surface area} = \frac{N_a P V_m}{RT} \sigma_0 \quad (13)$$

Where N_a is Avagadro's constant, P is atmospheric pressure, R is the universal gas constant, T is standard temperature and σ_0 is the cross-sectional area of the adsorbate, which is $1.62 \times 10^{-19} \text{ m}^2$ for nitrogen (Naderi, 2015; Shearer et al., 2016).

The procedure for conducting BET analysis was as follows. The mass of the empty tube with a rubber cap was recorded. Approximately 0.12 - 0.14 g of sample was measured and inserted into the tube. The tube with samples was activated at different temperatures under a vacuum in the degassing unit. Resins were activated for 3 hours at 60 °C, and Zr-MOF-808 was activated for 3 hours at 160 °C. The activated sample was capped using the rubber cap, and the mass was recorded. The dewar flask was filled with liquid nitrogen to a level between lower end and hole in the metering tool. The tubes were inserted into the slots of BET instrument and nitrogen sorption experiments were performed at 77 K. The data were obtained in .xls file format and plotted in the application Microsoft excel.

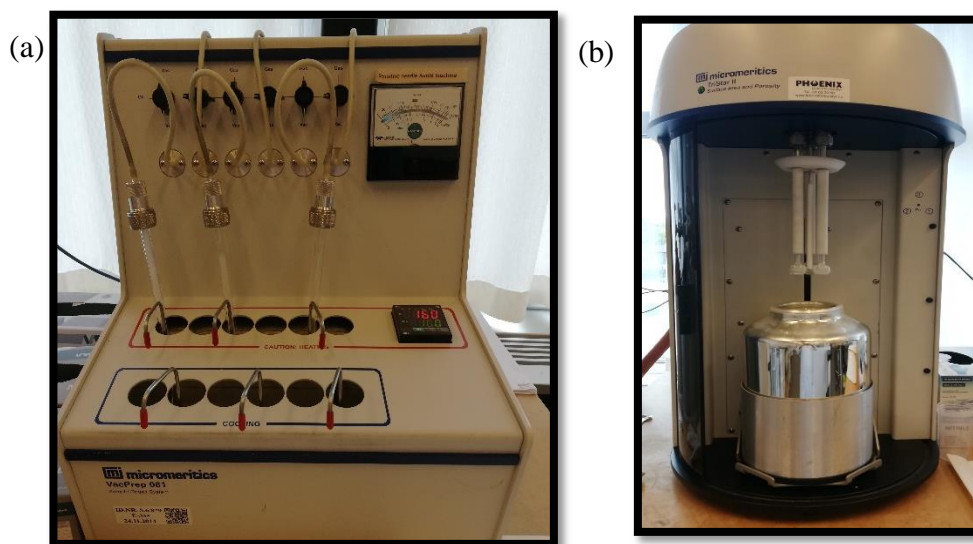


Figure 3.6. (a) Degassing unit with samples placed on heating positions (b) N_2 sorption instrument with samples inserted for analysis

3.2.6 X-Ray Fluorescence spectroscopy (XRF)

The XRF analysis is non-destructive, simple, and fast with lower equipment costs and no recalibration requirement. The portable XRF analyzer used in this study has the added advantage of in-situ analysis to select an operation area by considering the effect of associated

radiation. The portable XRF is generally used as a surface analyzer. The X-rays generated from the Rhodium anode excite the elements to produce fluorescence X-rays based on their characteristic energies. The detection of elements is carried out by a silicon drift detector. Finally, signal processing is required to resolve the matrix interference caused by the effects between closely related elements in terms of Fluorescence energy. However, it is problematic to analyze the elements with low atomic numbers by XRF because of the attenuation of fluorescence in the air.

The procedure for conducting XRF analysis was as follows. The ground battery samples were placed on the detection window and quantitatively analyzed by handheld XRF spectrometer Tracer 5 (Bruker). The excitation source was a Rhodium thin window X-ray tube consisting of an X-ray generator of operator adjustable voltage and current of 6-50kV and 4.5-195 μ A, respectively, with maximum 4W output power. The detector used was a 20mm² silicon drift detector with a detector window of 1 μ m graphene and a signal detection time of 90 s. The analysis spot size was kept at 8 mm by adjusting the source collimator.

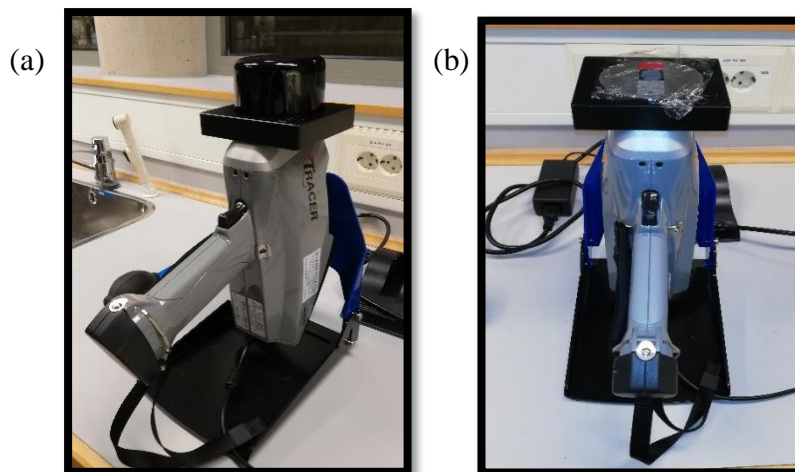


Figure 3.7. (a)XRF instrument (b) Solid samples placed on sample plate for XRF analysis

Geo exploration application oxide 3 phase method and a high voltage of 50 kV, current 28 μ A, Bayesian deconvolution method were used for determining the weight percentage and peak area respectively. The data was obtained in XY format and analyzed using Excel software.

3.2.7 Inductively coupled plasma - optical emission spectrometry (ICP-OES)

ICP-OES is used to detect multi-elements from liquid samples simultaneously by atomizing and exciting the atoms with hot plasma. Therefore, the metal ions in black mass digestion and leachates can be analyzed to determine the elemental composition.

The procedures and conditions for the analysis were as follows. Samples were filtered using a 0.2 μm pore size syringe filter and diluted with 5 % HNO_3 to 1:10 or 1:100 before the analysis. The Perkin Elmer Optima 4300 DV instrument was used for the analysis and consists of a quartz torch. Analysis was conducted in a wavelength range from 167 to 852 nm with 6000×6000 pixels Segmented-array Charge-coupled Device (SCD) detection, which detects 79 spectral lines per mm.

3.2.8 Nuclear magnetic resonance (NMR)

NMR was used to quantify the exchange and loading of the ligands into MOF-808-acetate. The analysis was conducted by Jeol 400Hz NMR Spectrometer. 20mg of MOF sample was weighed into a centrifuge tube and 1mL of freshly prepared 1M NaOH in D_2O was added. The centrifuge tube was shaken with IKA MS basic shaker, and the centrifuge tubes were kept for 24 h for digestion. This procedure ensures that the organic compounds leaches out of the MOF whereas the inorganic part settles at the bottom. After 24 h, the mixture was then centrifugated to separate the suspension and transferred into the NMR tube for the analysis. The data were processed using TopSpin software, the peaks were integrated, and the protons were normalised in accord to the protons of trimesic acid.

3.3 Digestion of black mass using aqua regia

Black mass was digested to dissolve the metals into the leachate. 20 mL of Aqua regia of HCl to HNO_3 in 3:1 volume ratio was added to 1 g of black mass and digested at 80 $^\circ\text{C}$ for 2h, and following the addition of 2 mL of H_2O_2 , the mixture was digested further for 0.5 h. The supernatant obtained after centrifuging at 4000 rpm for 15 min was analyzed using an inductively-coupled plasma optical emission spectrometer (ICP-OES, Perkin Elmer Optima 4300 DV).

3.4 Characterization of black mass

Black mass and its solid residues after the digestion in aqua regia with and without H_2O_2 were subjected to XRF to determine the cobalt, manganese, and nickel content. The structure and the thermal behaviour were analyzed by XRD and TGA respectively. Morphologies and elemental compositions were analyzed using SEM-EDS.

3.5 MOF-808 Synthesis and ligand exchange

Initially, MOF-808-acetate was synthesized, and the ligand exchange was carried out to form MOF-808-benzoate, MOF-808-DHBA, and MOF-808-EDTA.

3.5.1 Synthesis of MOF-808-acetate

In a round bottom flask, 3.0 g (1 eqv.) of $ZrOCl_2 \cdot 8H_2O$ was dissolved in 10 mL (60 eqv.) of distilled water. A 26 mL (50 eqv.) of acetic acid was added to the above solution and stirred. Once a clear solution is obtained 0.67 g (0.34 eqv.) of H_3BTC was added and the reaction mixture was heated for 72 h at $95^\circ C$. The solid product was isolated by centrifugation for 15 min at 4000 rpm after the reaction mixture was cooled down to room temperature. The solid product was thoroughly washed 3-5 times in distilled water and dried in an oven overnight at $60^\circ C$ (Aunan et al., 2021).

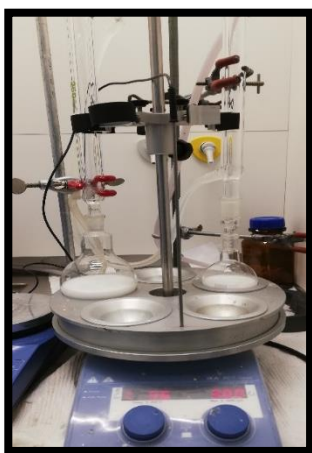


Figure 3.8. Experimental setup for synthesis of MOF-808-acetate

3.5.2 Ligand exchange to form derivatives of MOF-808

MOF-808-acetate was subjected to solvent-assisted ligand exchange (SALE) to form MOF-808-X (X= Benzoate, 3,4-dihydroxybenzoate) and graft the functional groups from benzoic acid and 3,4-dihydroxybenzoic acid. Aqueous solutions of benzoic acid, and 3,4-dihydroxybenzoic acid were prepared, and MOF-808-acetate was dispersed in the quantities shown in Table 3.1. The mixture was heated at $60^\circ C$ for 20 h in a condenser fitted flask and stirred at 200 rpm. The powder was separated by filtration while hot and washed initially using hot water at $60^\circ C$ followed by acetone. The resulting powder was oven dried at $120^\circ C$ overnight.

Table 3.1. Quantities of chemicals required for ligand exchange

Ligand	Mass of MOF-808-acetate (g)	Mass of ligand (g)	Volume of water (mL)
Benzoic acid	0.5	0.60	50
3,4-dihydroxybenzoic acid	0.5	0.77	50



Figure 3.9. Experimental setup for ligand exchange

3.5.3 Synthesis of MOF-808-EDTA.

EDTA-2Na solution was prepared by dissolving 22.32 g EDTA and 5.3082 g of NaOH in 600 mL of distilled water. MOF-808-EDTA was prepared by following the procedure reported in (Y. Peng et al., 2018). 1.2 g of activated MOF-808-acetate was added to the prepared EDTA-2Na solution. The solution was heated at 60 °C for 24 h in a 1 L capped glass bottle. The solution was filtered to obtain a white powder and washed several times with water to remove unreacted EDTA, followed by acetone several times to exchange water in MOF-808-EDTA pores. The powder was then dried in an oven overnight at 60 °C.

3.6 MOF-808 characterization

The synthesized MOF-808-acetate and its derivatives were characterized using the methods such as XRD, TGA, ATR-IR, SEM-EDS, N₂ sorption, and NMR for crystal structure, thermal stability, surface functional groups, particle morphology-elemental composition, surface area, and the loading of functional group respectively.

3.7 Characterization of resins

The resins in its as received and treated (section 3.12.1) forms were characterized using the methods such as ATR-IR and N₂ sorption for determining surface functional groups and the surface area, respectively.

3.8 Leaching of black mass

Different acids such as phosphoric acid, tartaric acid and citric acid were used to leach the metals from black mass according to the optimized conditions as mentioned in the following studies.

Table 3.2. Optimized conditions used for black mass leaching

Leachate	Temperature (°C)	Time (min)	Liquid-solid ratio (mL g ⁻¹)	Efficiency (From Literature)	Reference
Phosphoric acid 0.8 M + 4 % (v/v) H ₂ O ₂	70	60	20	Ni- 12.54%, Co- 1.63%, Mn- 1.70%, and Li- 98.94%	(Xiangping Chen et al., 2018)
Tartaric acid 0.5 M+ 4 % (v/v) H ₂ O ₂	70	30	59	-	(He et al., 2017)
Citric acid 2M + 2 % (v/v) H ₂ O ₂	80	90	30	Ni- 98%, Co- 97%, Mn-98%, and Li-89%	(Xiangping Chen & Zhou, 2014)
Sulphuric acid 2 M + 5 % (v/v) H ₂ O ₂	75	30	10	Co-93 %, Li- 94%	(Ahn et al., 2019)

The recovery efficiencies in leaching media for different metals were calculated according to equation 14.

$$LE = \frac{C \times V}{m \times w} \times 100\% \quad (14)$$

where LE is the leaching efficiency of metal in percentage, C (g L⁻¹) is the leachate metal ion concentration, V (L) is the volume of leaching solution, m (g) is the mass of black mass sample leached and w is mass to mass fraction for the respective metal in black mass digested using aqua regia.



Figure 3.10. Experimental setup for black mass leaching

3.9 Determination of acid stability of MOF-808

A volume of 20 mL of acids were used with leached metals or without metals, and pH was adjusted using 1 M NaOH and 1 M HCl by adding appropriate volumes according to the pH meter reading. 100 mg of MOF-808 was added to pH adjusted solutions and stirred at 200 rpm for 24 h. The solution was centrifuged at 4000 rpm for 15 min, and the solid residue was dried in an oven at 60 °C overnight. The residue was analyzed by XRD and TGA and compared with the initial form to determine the stability.

3.10 Preparation of simulated solutions.

2000 mgL⁻¹ of Ni²⁺, 600 mgL⁻¹ of Co²⁺ and a mixed solution of both metal ions, which corresponds to 1:5 diluted aqua regia digestion solution metal concentrations were prepared using 2.0876 g and 0.6057 g of NiCl₂·6H₂O and CoCl₂·6H₂O respectively in 250 mL of distilled water. The leachate metal concentrations 350 mgL⁻¹ of lithium and 500 mgL⁻¹ of manganese obtained by the analysis mentioned above were used in addition to nickel and cobalt to prepare the mixed simulated solution of 4 metal ions. For Mn²⁺ and Li⁺, distilled water solutions of 250 mL were prepared using 0.4503 g and 0.5345 g of MnCl₂·4H₂O and LiCl respectively.

3.11 Preparation of UV-visible spectrometer calibration curves

Initially, 100 mL of 2500 mgL⁻¹ of Co²⁺ solution and 10000 mgL⁻¹ of Ni²⁺ were prepared using 1.0094 g CoCl₂·6H₂O and 4.1751 g NiCl₂·6H₂O, respectively in distilled water. A series of concentrations 250, 500, 1000, 1500, 2000, and 2500 mgL⁻¹ of Co²⁺ and 500, 1000, 2000, 3000, 4000, 5000, 6000 mgL⁻¹ of Ni²⁺ were prepared by diluting the initial Co²⁺ and Ni²⁺ solutions with distilled water. A volume of 2.5 -3.0 mL of the prepared solutions was taken into a quartz cuvette and measured using UV-1600PC Spectrophotometer to record the spectra from 190 nm to 900 nm wavelength. The absorbance of the peaks at 511 nm and 394 nm were recorded corresponding to Co²⁺ and Ni²⁺ respectively, to prepare the calibration curves of concentration vs absorbance.

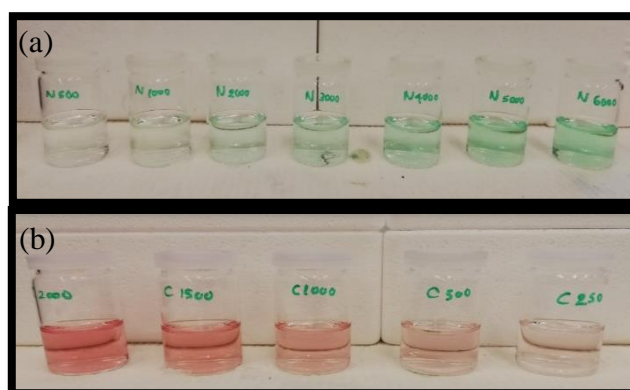


Figure 3.11. Solutions prepared for preparing calibration curve (a) nickel (b) cobalt

3.12 Resin batch adsorption experiments

Simulated nickel and cobalt solutions were prepared using distilled water. Sorption was studied by varying experimental parameters, such as solution initial pH, temperature, contact time, initial metal concentration, and liquid-solid (metal solution-resin) ratio.

3.12.1 Pretreatment of resins

The resin, Amberlite IRC 748, was used in as received (Sodium) form and treated (hydrogen) form for the adsorption experiments. Resins in Sodium form were first stirred at 70 rpm with 1M H₂SO₄ for 1 h and washed with pH 5 distilled water to remove impurities to convert the resin to the hydrogen form.

3.12.2 Determination of the effect of resin form and pH

The batch adsorption experiments at a temperature of 20 °C were conducted in 50 mL glass vials by adding 0.5 g resin in both as received and treated form into 25 mL of individual metal (Ni²⁺ or Co²⁺), mixed metals (Ni²⁺ and Co²⁺) solution, and mixed metals (Ni²⁺, Co²⁺, Mn²⁺ and Li⁺) solution with pH adjusted to 2, 4, and 6. pH was measured using pH meter (VWR PH 1100L). A 70 rpm stirring was provided using a magnetic stirrer for adequate mixing with minimal physical damage to the resin beads. After 24 h, the solution was filtered to separate adsorbents using qualitative filter paper of 5-13 μm particle retention and 90 mm diameter. The filtrate obtained was filtered again using PVDF syringe filters of pore size 0.2 μm and analyzed by UV-visible spectrophotometer to determine the metal concentrations using the prepared calibration curve.

3.12.3 Determination of the effect of temperature

The temperature effect on resin adsorption was evaluated by conducting batch adsorption experiments at 20 °C, 30°C and 40 °C at the selected pH values of 3 and 4 for synthetic solutions of Ni²⁺ and Co²⁺, respectively.

3.12.4 Determination of adsorption kinetics

The kinetic parameters and effect of contact time on resin adsorption were evaluated by conducting separate batch adsorption experiments, which were filtered at time intervals of 0.5 h, 1 h, 2 h, 3 h, 4 h, and 6 h at 20 °C temperature and pH values of 3, 4 and 6 for synthetic solutions of Ni²⁺, Co²⁺ and mixed metal ion solution respectively.

3.12.5 Adsorption isotherm experiment

The batch adsorption experiments were conducted at different concentrations for Ni²⁺ (500, 1000, 2000, 3000, 4000, 5000, 6000 mgL⁻¹) and, Co²⁺ (250, 500, 1000, 1500, 2000, 2500

mgL⁻¹) for 3 h until it reached equilibrium concentrations. The experiments were conducted at 20 °C temperature and pH values of 3 and 4 for synthetic solutions of Ni²⁺ and Co²⁺ respectively.

3.12.6 Determination of the effect of liquid-solid ratio

The batch adsorption experiments were conducted at different liquid-solid ratios of 10, 20, 30, 40, and 50 mL g⁻¹ for 3 h until equilibrium. The experiments were conducted at 20 °C temperature and pH values of 3, 4 and 6 for synthetic solutions of Ni²⁺, Co²⁺ and mixed metal ion solution, respectively.

3.12.7 Determination of the effect of liquid-solid ratio in the presence of Mn²⁺ and Li⁺

The batch adsorption experiments were conducted at different liquid-solid ratios of 10, 20, 30, 40, and 50 mL g⁻¹ for 3 h until equilibrium. The experiments were conducted at 20 °C temperature and pH 6 for simulated mixed metal ion solution of Ni²⁺, Co²⁺, Mn²⁺ and Li⁺.

3.12.8 Regeneration of resins

The metal loaded resin beads were eluted using 1M H₂SO₄ for 24 h, and the eluate was analyzed for Ni²⁺ and Co²⁺ using a UV visible spectrophotometer. The resins after elution were washed using distilled water, 1 M NaOH and again by distilled water and dried overnight at room temperature.

3.13 Resin column breakthrough experiment

5.0 g of as received resin was packed into a column with height 20 cm and internal diameter 1.5 cm. The resin bed height was about 4 cm. The top of the resin bed was covered by a layer of glass wool to ensure uniform liquid distribution. Simulated mixed metal ion solution of Ni²⁺, Co²⁺, Mn²⁺ and Li⁺ adjusted to pH 6 at 20 °C was poured manually, maintaining a constant liquid level in the column. The average solution flowrate was 0.67 mL min⁻¹. The solution from the column outlet was collected at 10 min time intervals and filtered using PVDF syringe filters of pore size 0.2 µm and analyzed by UV visible spectrophotometer to determine the Ni²⁺ and Co²⁺ concentrations using the prepared calibration curves.

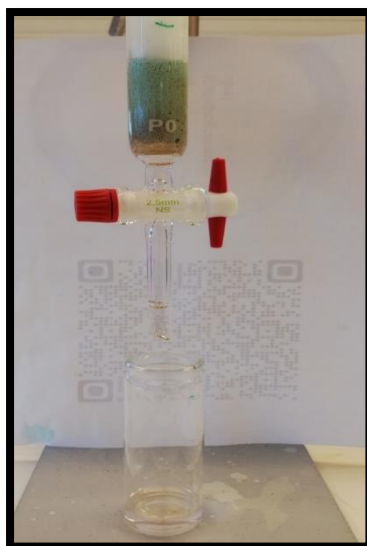


Figure 3.12. Resin breakthrough column experimental setup

3.14 Characterization of regenerated resins

The regenerated resins were characterized using the methods such as ATR-IR and N₂ sorption for determining surface functional groups and the surface area, respectively.

3.15 MOF-808 batch adsorption experiments

Simulated solutions of Ni²⁺ and Co²⁺ were prepared using distilled water, and sorption was studied by varying experimental parameters, such as solution initial pH and liquid-solid (metal solution-resin) ratio.

3.15.1 Determination of the effect of pH

The batch adsorption experiments were conducted in 50 mL glass vials at 20 °C temperature by adding 0.1 g MOF-808-acetate, MOF-808-benzoate, MOF-808-DHBA, and MOF-808-EDTA into 20 mL of individual metal (Ni²⁺ or Co²⁺), mixed metals (Ni²⁺ and Co²⁺) solution, and mixed metals (Ni²⁺, Co²⁺, Mn²⁺ and Li⁺) solution with pH adjusted to 2, 4, and 6. pH was measured using pH meter (VWR PH 1100L). After 24 h stirring at 200 rpm, the solution was centrifuged at 4000 rpm for 15 min. The supernatant obtained was filtered using PVDF syringe filters of pore size 0.2 μm and analyzed by UV visible spectrophotometer to determine the metal concentrations using the prepared calibration curve.

3.15.2 Determination of the effect of liquid-solid ratio

The batch adsorption experiments were conducted for MOF-808-acetate and MOF-808-EDTA at different liquid-solid ratios of 50, 100, 150, 200, and 250 mL g⁻¹ for 24 h until equilibrium. The experiments were conducted at 20 °C temperature and a pH of 6 for a simulated mixed metal ion solution of Ni²⁺ and Co²⁺.

3.15.3 Determination of the effect of liquid-solid ratio in the presence of Mn^{2+} and Li^+

The batch adsorption experiments were conducted for MOF-808-EDTA at different liquid-solid ratios of 50, 100, 150, 200, and 250 mL g^{-1} for 24 h until equilibrium. The experiments were conducted at 20 °C temperature and pH of 6 for simulated mixed metal ion solution of Ni^{2+} , Co^{2+} , Mn^{2+} and Li^+ .

3.15.4 Regeneration of MOF-808-EDTA

The metal loaded MOF-808-EDTA was regenerated using 0.22 M 2Na-EDTA and washed using distilled water, dried overnight at 60 °C temperature, and then used for another adsorption cycle to determine the adsorption capacity and solution metal removal.

3.16 Characterization of regenerated MOF-808-EDTA

The regenerated MOF-808-EDTA were characterized using the methods such as XRD, TGA, ATR-IR, N_2 sorption, and EDS for crystal structure, thermal stability, surface functional groups, surface area, and the elemental composition, respectively.

3.17 Batch adsorption experiments in black mass citric acid leachate

The batch adsorption experiments were conducted in 50 mL glass vials at 20 °C temperature by adding 0.1 g MOF-808-acetate, MOF-808-benzoate, MOF-808-EDTA, and as received resin into 20 mL of pH 6 adjusted citric acid leachate. After 24 h stirring at 200 rpm, the solution was centrifuged at 4000 rpm for 15 min. The supernatant obtained was filtered using PES membrane syringe filters of pore size 0.2 μm and analyzed by ICP-OES to determine the metal concentrations. The solid adsorbent residues were characterized by XRD to determine chemical stability.

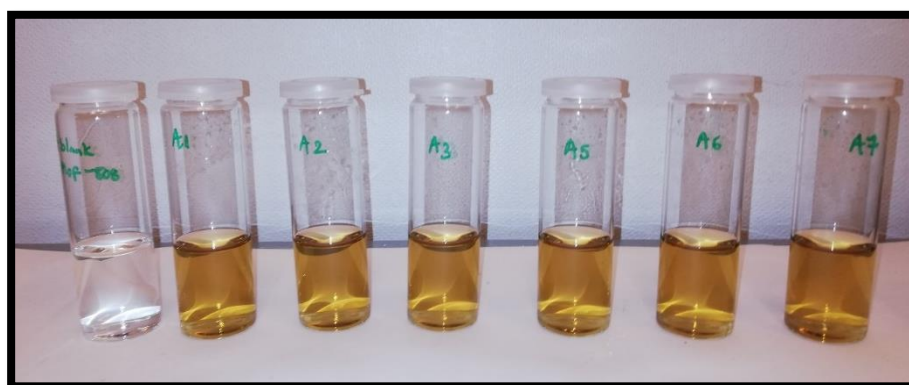


Figure 3.13. Black mass leachate solutions after adsorption experiments

4. RESULTS AND DISCUSSION

This section presents the results of all the characterization parts and adsorption experiments, including a detailed discussion of the results. The data and calculations relevant to the tables and figures in this section are included in the appendix.

4.1 Characterization of black mass and black mass leached residue

The black mass analysis from XRF, ICP-OES, XRD, TGA, and SEM-EDS were adopted to obtain the characterization results.

4.1.1 Determination of the composition of black mass

The composition of black mass samples analyzed by XRF and ICP-OES is illustrated in Tables 4.1 and 4.2, respectively. The analysis was conducted in duplicates and triplicates for each sample, and the mean weight percentage of each element in the battery samples with standard deviation was indicated (Appendix 1 and Appendix 2). The composition values of the two analysis methods were significantly different due to the physical state of the samples analyzed. XRF determined the composition of the solid black mass sample. Thus it should indicate the total quantity of the metals in it. Still, for metals of interest such as Co, Mn, Fe, Cu and Al, XRF gave lower quantities indicating the error of using it for quantification purposes of elements having spectral interference and samples with a high degree of heterogeneity. When considering ICP-OES results, even though it is considered that aqua regia digestion digests the metals 100 %, the results obtained for nickel indicated that it was not as expected.

Table 4.1. XRF analyzed composition for black mass

Element	MgO	Al ₂ O ₃	SiO ₂	P	S	Ca	Cr	Mn	Fe	Co	Ni	Cu	Zn	Zr	Mo
% (w/w)	0.89± 0.31	3.6± 0.72	1.91± 0.32	0.1± 0.01	0.35± 0.07	0.38± 0.09	0.16± 0.05	3.36± 0.66	0.41 ±0.1	1.75± 0.47	48.57± 5.38	3.83± 0.62	0.28± 0.08	0.11± 0.05	0.02± 0.01

Table 4.2. ICP-OES analyzed composition for digested solution

Element	Al	Co	Cu	Fe	Li	Mn	Ni	Ca	Cr	K	Mg	Zn
% (w/w)	4.45±0.21	6.25±0.35	5.55±0.35	0.9	3.3	5.3±0.28	20.3±1.27	0.4	0.1	0.2	0.5	0.5

Figure 4.1 shows the elements present in Aqua regia leachate in a graphical format as determined by ICP-OES. Nickel was the most abundant element, while aluminium, cobalt, copper, manganese and lithium were in significant quantities in 1- 6 % (w/w).

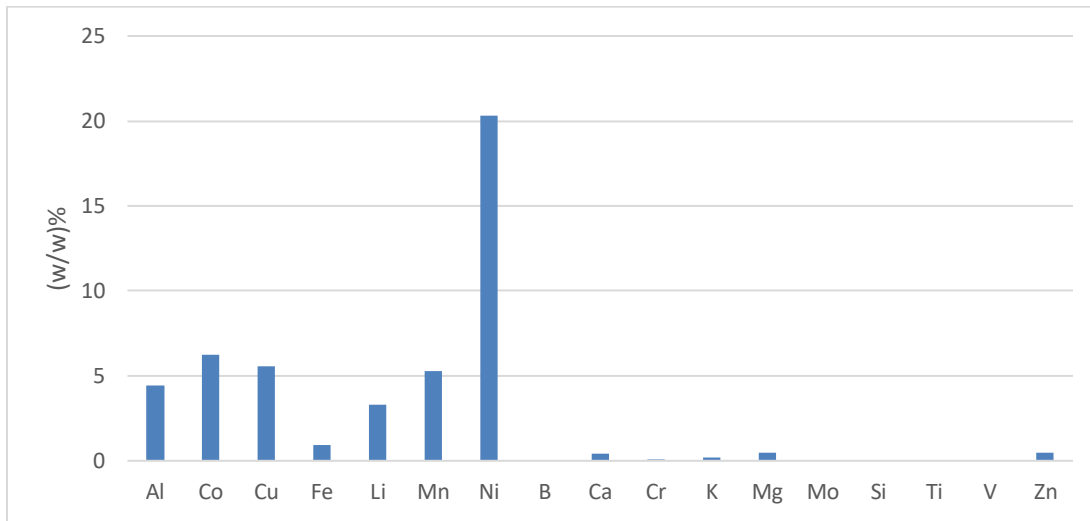


Figure 4.1. ICP-OES determined composition of digestion solution

According to the composition of nickel, manganese and cobalt, a configuration of NMC 722 was obtained (Appendix 3). Therefore, the black mass can be considered a mixture of NMC 622 and NMC 811.

The mean values for the leaching by both analysis methods were tabulated in Table 4.3.

Table 4.3. Mean leachate metal weight percentages

Sample	Metal %(w/w)- ICP- OES			Metal %(w/w)- XRF		
	Co	Mn	Ni	Co	Mn	Ni
Mean of Aqua regia leached	5.50.85	4.7±0.85	18.05±2.62	1.84±0.19	4.76±0.21	31.74±5.51
Mean of Aqua regia + H ₂ O ₂ leached	6.25±0.35	5.3±0.28	20.3±1.27	1.95±0.2	4.81±0.27	33.34±5.5

Comparison between ICP-OES and XRF results for the leached weight percentages of metals when subjected to Aqua regia leaching and Aqua regia + H₂O₂ leaching were tabulated in table 4.3. The ICP-OES analysis results were converted from the metal concentration of leachate to the percentage of metals leached. In XRF, the difference between the black mass and leached black mass residue metal weight percentage was used to calculate each sample's leached metals' weight percentages.

The results obtained by analysis of leachate solution by ICP-OES resulted in higher values for cobalt and manganese and lower values for nickel compared to the material balance calculation conducted for black mass to determine the metal weight percentages in leachates using XRF analysis results.

However, cobalt weight percentage resulted in a higher difference in results for the two analysis methods compared to manganese and nickel, possibly due to the spectral interference of cobalt and iron in XRF analysis. Also, the ICP-OES analyzed metal concentrations in leachate have decreased when subjected to Aqua regia +H₂O₂ leaching, which should have been increased according to the other studies which indicated the enhancement of leaching efficiency by using a reducing agent such as H₂O₂.

4.1.2 Black mass XRD analysis

Figure 4.2 demonstrates the XRD of black mass sample. The highest intensity characteristic peak was observed around 18-19 degrees 2 theta for the pristine cathode material. XRD spectra similar to black mass before thermal treatment was not observed in the spectra in this study due to the use of thermally treated black mass where the reducing heating pretreatment transforms LiNi_xCo_yMn_zO₂ into phases of Ni, Co, MnO and Li₂CO₃ (H. Wang et al., 2017). Several characteristic peaks of raw black mass have attenuated due to leaching. New peaks have appeared, indicating the formation of new products during leaching, dissolving the existing compounds (Xiangping Chen et al., 2019).

Furthermore, most of the changes in peaks are similar in leached residues except for the aqua regia digestion sample, indicated that almost similar chemical compounds result from tartaric, phosphoric, and citric acid leaching. The most sustaining and intensified characteristic peak in all the leached residue samples around 26-28 degrees 2 theta was considered to be from graphite (X. Zeng et al., 2015).

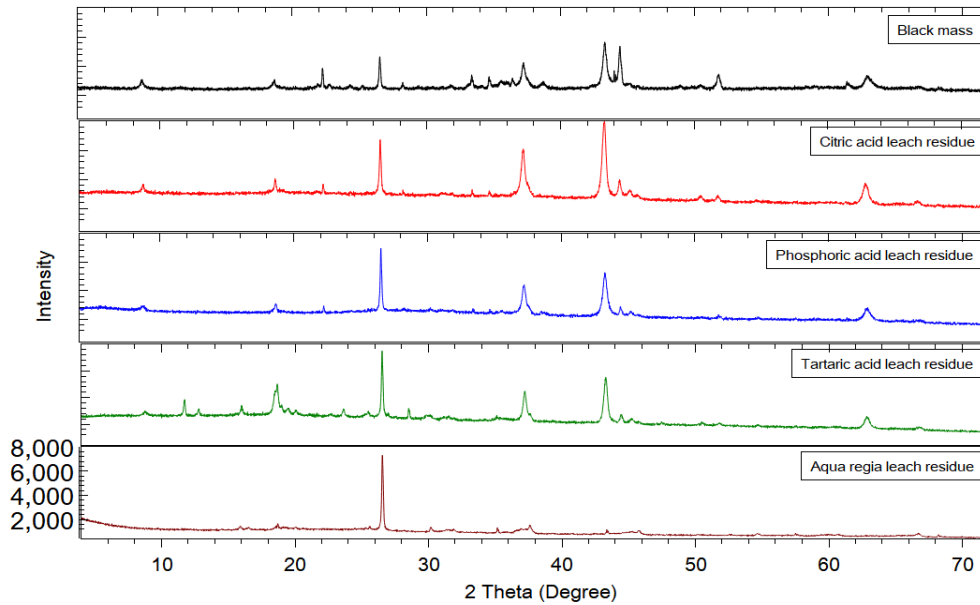


Figure 4.2. X-ray diffraction patterns of black mass and black mass leach residues of acids

4.1.3 Black mass SEM-EDS analysis

Figure 4.3 displays SEM images of black mass (b) and the black mass residue after citric acid leaching (d) and their corresponding EDS elemental contents. It can be observed that black mass particles were irregular shaped and consisted of particles of different sizes, but in citric acid leach residue, the irregular shaped particles were smaller in size and distributed in lower size distribution. This indicated a removal process that happened during citric acid leaching, which confirmed the elemental analysis results through EDS. The weight percentages of nickel, cobalt and manganese have reduced. But in the case of nickel, a weight percentage of 10.64 % remained even after citric acid leaching due to its higher abundance in black mass. It should also be noted that the black mass had diversified elemental compositions due to its heterogeneous distribution of components, as indicated by the presence of aluminium and carbon in leach residue, which was not detected in the black mass sample analyzed. These SEM-EDS samples were not taken from the same sample amount for the analysis. Therefore, it may have affected the quantitative values obtained in elemental composition analysis from EDS. However, the trend in the metal removals was as expected due to leaching. In order to get the exact overview of the leaching process, it is important to use the same sample to analyze before and after leaching.

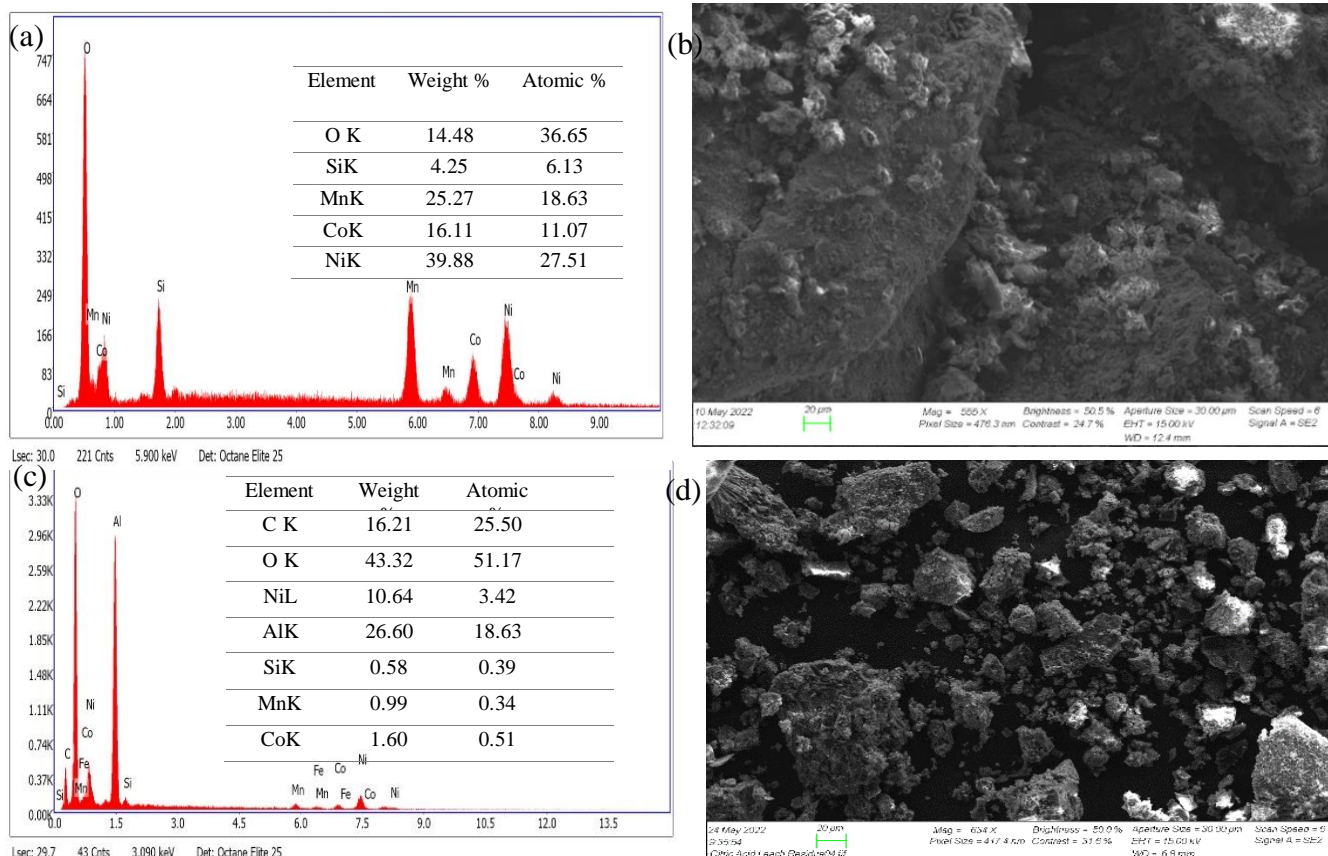


Figure 4.3. SEM-EDS analysis: (a) EDS and (b) SEM of black mass. (c) EDS and (d) SEM for black mass after citric acid leaching

4.1.4 Black mass TGA analysis

Figure 4.4 presents the TGA curves for black mass and citric acid leach black mass residue when heated in the air from 25 °C to 1000 °C. According to the TGA, the black mass was a thermostable material in the analyzed temperature range, showing a slight weight loss of 4% and a weight gain that may be due to oxide formations when heated above 700 °C. However, the citric acid leached black mass residue showed a 38 % weight loss in the considered temperature range. The free and bound water in the residue is expected to be removed until 150 °C, which accounts for a 4 % weight loss. The remaining weight loss can be considered to be due to the oxidation and calcination of the citric acid leach residue. When heated above 350 °C, the citric acid leach residue had an approximately constant weight with a weight loss of less than 5 %.

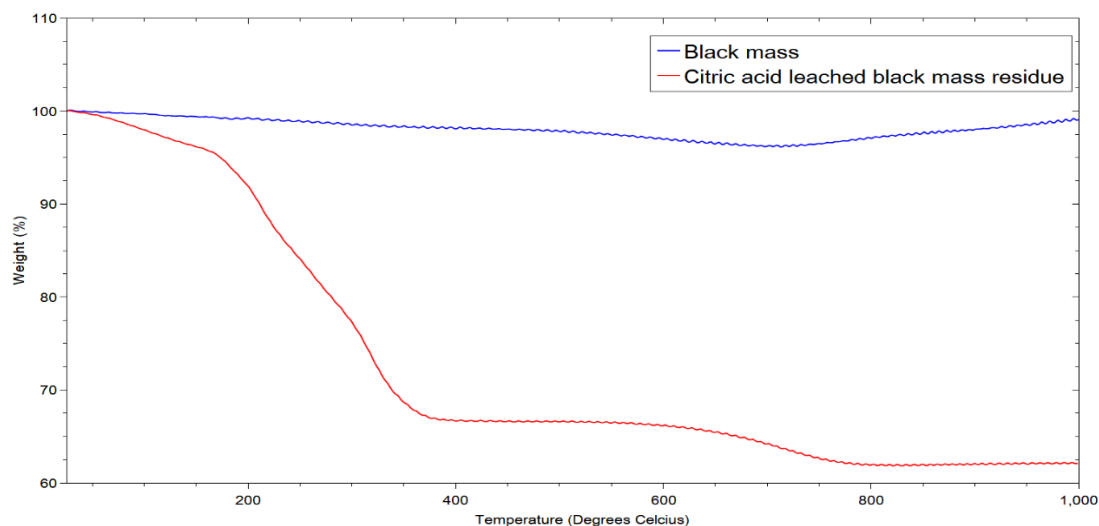


Figure 4.4. TGA for black mass and black mass after citric acid leaching.

4.1.5 Black mass ATR-IR analysis

Figure 4.5 shows ATR-IR spectra of black mass and the citric acid leached black mass residue. The spectra were divided into two regions known as the characteristic and fingerprint regions. The characteristic region comprised chemical bonds and groups of organic compounds, and the fingerprint region consisted of metal oxide bonds. The two curves showed similar behaviour from $3600-3200\text{ cm}^{-1}$, which was related to the stretching vibration of O-H of water molecules. At wavenumber 1580 cm^{-1} , citric acid leach residue had a lower reflectance indicating the presence of amide groups (Olsztyńska-Janus et al., 2018). Peaks in $1300-1000\text{ cm}^{-1}$ were mainly due to C-O and C-H stretching vibrations. At wavenumbers, 610 cm^{-1} and 560 cm^{-1} peaks were shown by vibrations of Li-O and Co-O, respectively (Xiangping Chen et al., 2019). But the spectra in this study were only recorded for wavenumbers above 650 cm^{-1} .

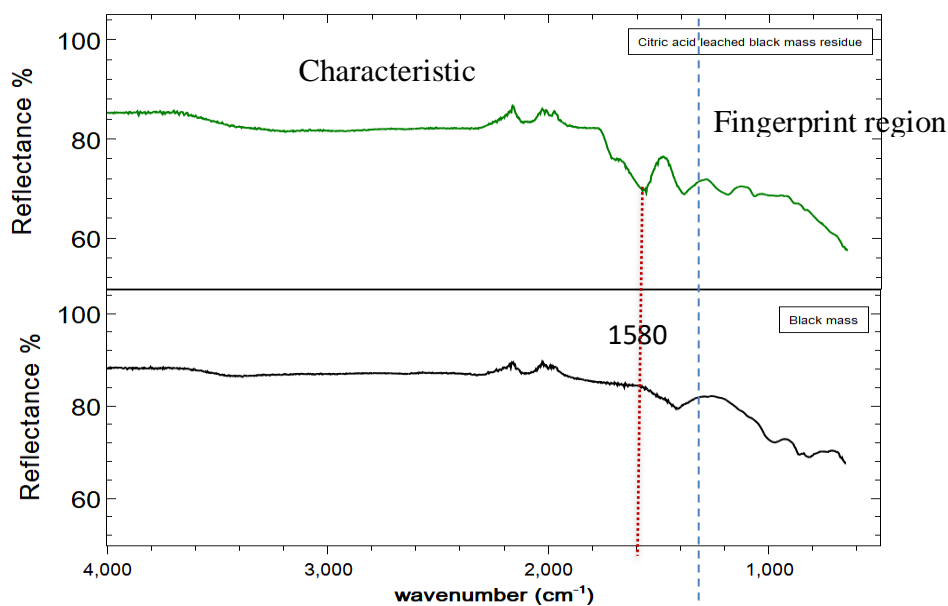


Figure 4.5. ATR-IR for black mass and citric acid leached black mass residue

4.2 Synthesis of MOF-808-acetate and ligand exchange

Several batches of MOF-808-acetate were synthesized based on the water-based protocol by (Aunan et al., 2021). The synthesis was conducted for 72 h to ensure the quality of the product and to get a higher yield. It was noted that the solids got firmly attached to the tube during centrifugation. Therefore, the attached solids were loosened and crushed using a spatula and taken to the solution phase to enhance the efficiency of the washing process.

The mass of the experimental product was calculated based on the TGA determined solvent and unreacted modulator removal percentage, which accounted for 19.34 % of the as-synthesized product yield. According to the theoretical yield calculation (Appendix 3), the experimental MOF-808-acetate yields were converted to yield % values as follows in Table 4.4.

Table 4.4. MOF-808-acetate yields for the synthesized batches.

MOF-808-acetate batch	Mass of ZrOCl ₂ .8H ₂ O (g)	Mass of experimental MOF-808-acetate (g)	Yield %
1	1.815	0.9945	74.77
2	1.500	0.7363	66.99
3	1.500	0.7439	67.68
4	3.000	1.6689	75.92
5	3.000	1.6823	76.53
6	3.000	1.5486	70.45
7	1.500	0.811	73.78
8	3.000	1.6529	75.19
9	1.500	0.8686	79.02

The yield percentages were in the range of 67 % - 79 %. This variation was due to the product loss during separation and distilled water washing of the samples. The separation was carried out by centrifuging at 4000 rpm for 15 min. But still, the supernatant had a slightly milky colour indicating the availability of a certain amount of products in suspension. Also, removing the linker and modulator from the MOF-808-acetate in the solvent and unreacted modulator removal region may have affected the accurate yield of the experimentally obtained product.

The ligand exchange reactions were conducted with synthesized MOF-808-acetate. First, the ligand to be exchanged was dissolved in water to form an aqueous solution. The added quantities of ligands were not soluble in the used amount of distilled water at room temperature. Therefore, the solutions were heated to the reaction temperature of ligand exchange in order to dissolve the ligands. The ligand exchanged MOF-808 was separated by filtration while it was hot to avoid retaining unreacted ligands with MOF.

4.3 Characterization of MOF-808

The MOF-808 –acetate and its modified MOFs such as MOF-808-benzoate, MOF-808-EDTA and MOF-808-3,4-dihydroxybenzoate were characterized by XRD, TGA, N₂ sorption, IR, NMR, and SEM-EDS.

4.3.1 XRD analysis

XRD was conducted to confirm the proper synthesis of the MOFs by considering their crystallinity. Figure 4.6 (a) and Figure 4.6 (b) show the XRD for simulated MOF-808 (Trickett et al., 2019) and synthesized MOF-808 in two forms, slurry and powder, respectively. The XRD patterns of the experimental MOF-808-acetate were normalized to the simulated curve. The XRD spectra of synthesized MOF-808 were consistent with the simulated spectra as there were no considerable difference in corresponding peaks of the spectra.

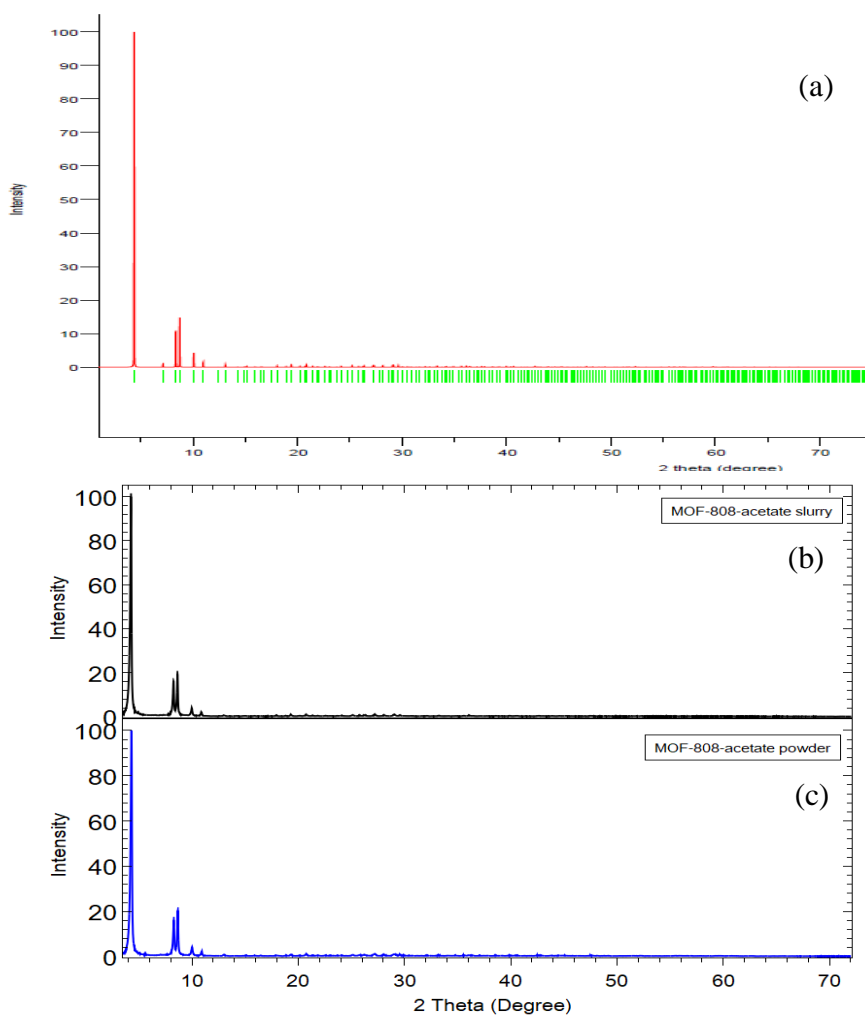


Figure 4.6. Normalized X-ray diffraction patterns for (a) simulated MOF-808 (b) MOF-808-acetate slurry (c) MOF-808-acetate powder

The MOF-808 samples synthesized in a single batch were around 1 g. The powder XRD required a significant amount of the synthesized samples, and also, the sample sizes used in adsorption applications were 0.1 g which was insufficient for powder XRD. Therefore, slurry samples were prepared for MOF-808 XRD. Figure 4.6 confirmed that the XRD patterns were the same for both slurry and powder samples.

Figure 4.7 shows the normalized XRD patterns of grafted groups to MOF-808-acetate. When comparing the grafted MOF-808 with MOF-808-acetate, it can be concluded based on observation of corresponding peaks that these MOFs had peaks at nearly the same 2θ angles which confirmed the unchanged crystallinity after the modification processes.

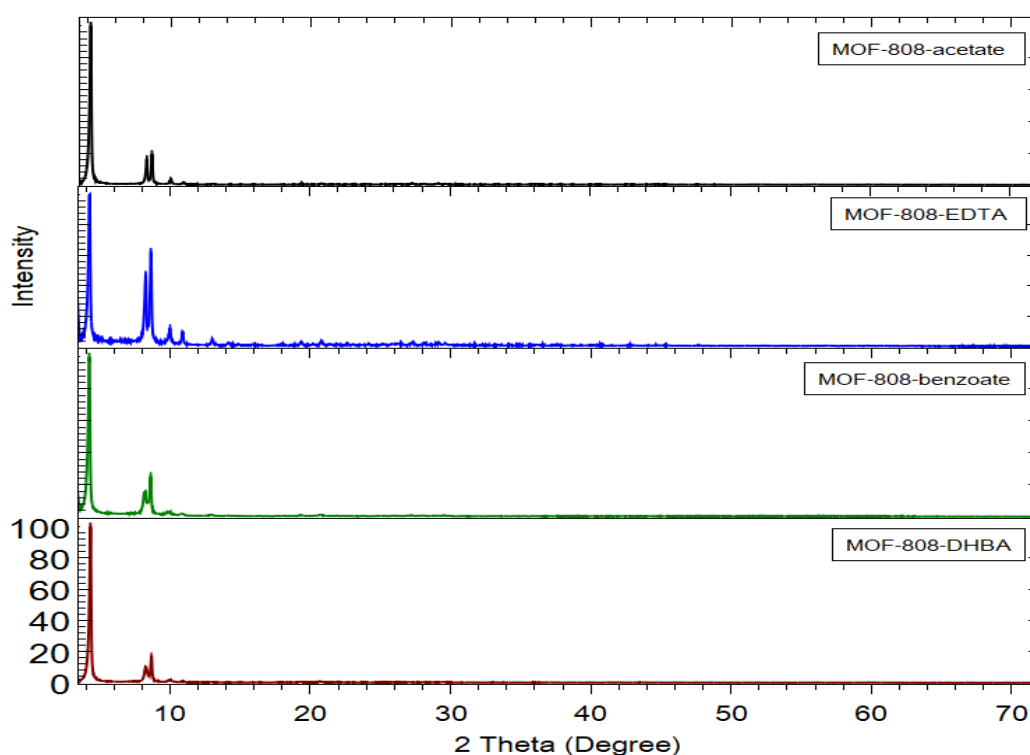


Figure 4.7. Normalized X-ray diffraction patterns for MOF-808

4.3.2 ATR-IR spectra

Figure 4.8 shows the ATR-IR spectra of MOF-808-acetate and its modified MOFs. After the exchange of ligands with MOF-808-acetate, several additional peaks were recorded. In MOF-808-EDTA, a peak closer to 1580 cm^{-1} was observed due to the C-N bond of the EDTA group. The three modified MOF-808 showed intense peaks closer to 1600 cm^{-1} and 1400 cm^{-1} due to the higher number of C=O bonds than MOF-808-acetate, confirming a structural modification in the samples of MOF-808 by EDTA, benzoic acid, and DHBA. All the curves showed

similar behaviour from 3600-3200 cm^{-1} , which represents the stretching vibration of O-H of water molecules.

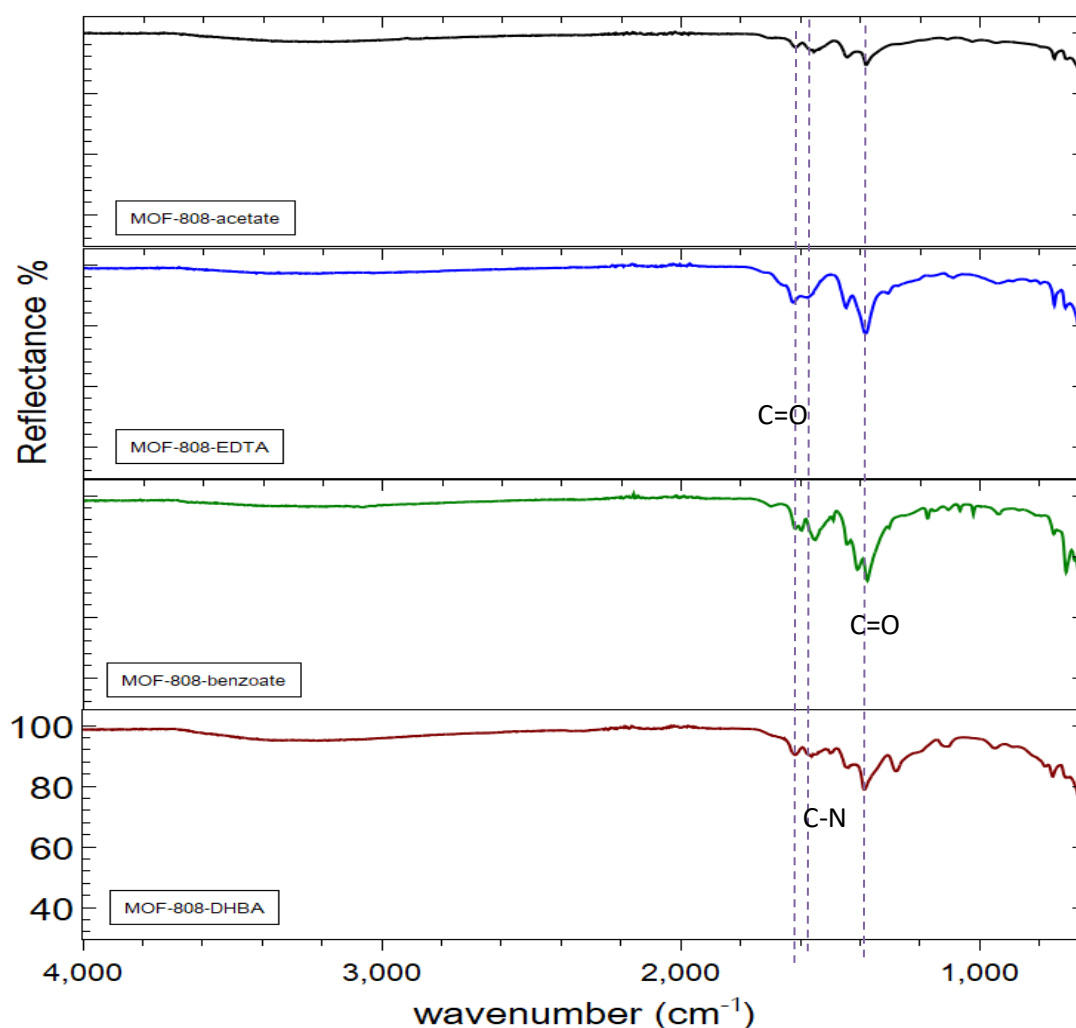


Figure 4.8. ATR-IR spectra of MOF-808

4.3.3 TGA analysis

Figure 4.9 shows the TGA for MOF-808-acetate. Three distinct regions observed can be described based on the study (Winarta et al., 2020). As shown in Figure 4.10, region 1 corresponded to the mass loss due to removing solvent and unreacted modulators in the pores. The mass loss in region 2 represented the dehydroxylation of metal nodes. It was assumed that regions 3 and 4 represent the mass losses due to the removal of the modulator and linker, respectively.

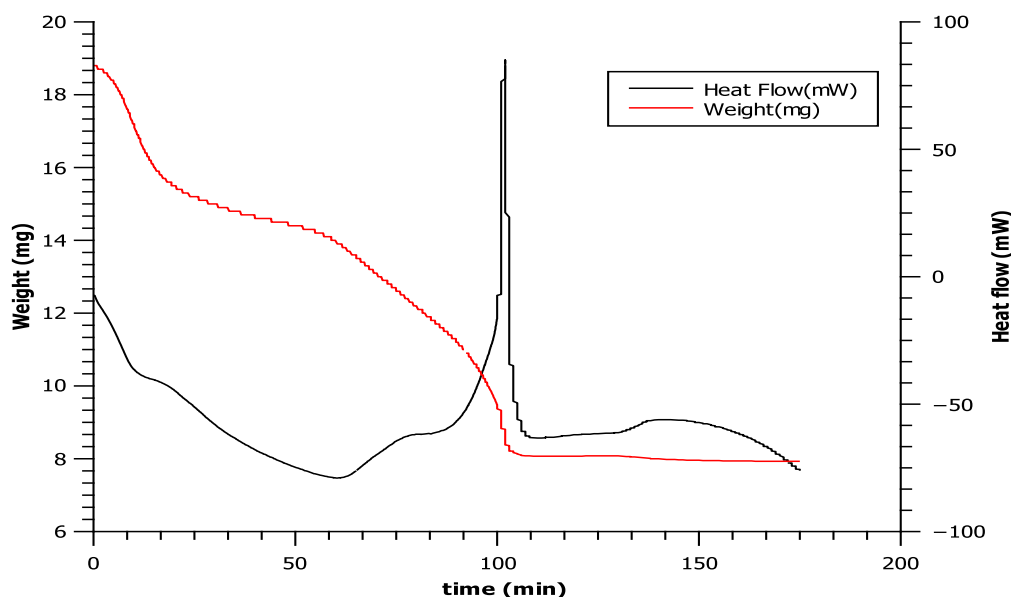


Figure 4.9. Variation of weight and heat flow with time for MOF-808-acetate

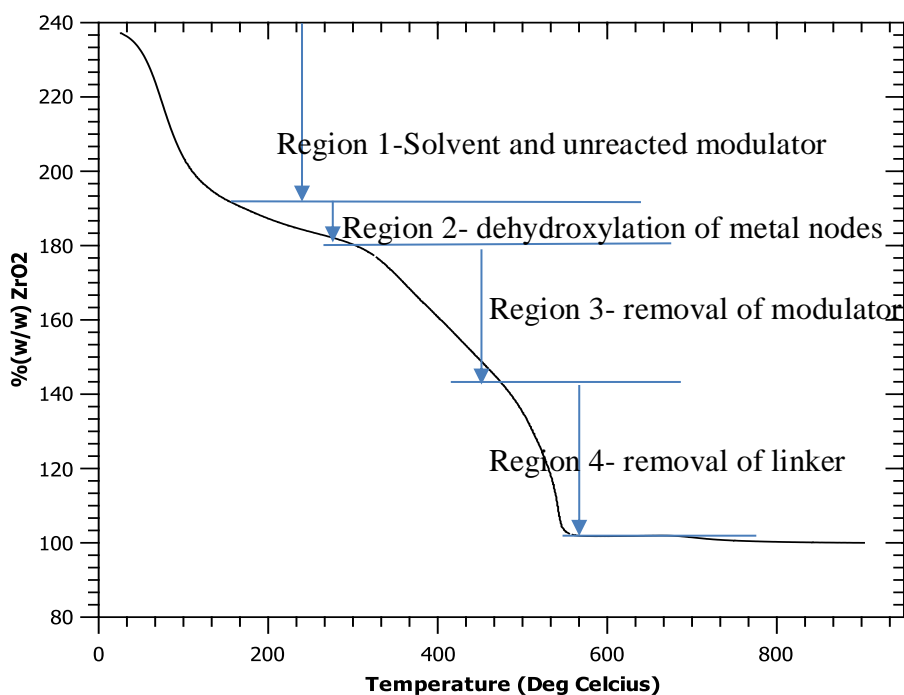


Figure 4.10. Regions of TGA curve of MOF-808-acetate

The theoretical mass loss percentages can be calculated as follows with respect to the weight of 6ZrO_2 .

$$\text{Theoretical weight \% of } \text{Zr}_6\text{O}_6\text{BTC}_2 = \frac{\text{Zr}_6\text{O}_6\text{BTC}_2}{6\text{ZrO}_2} = \frac{1057.54 \text{ g/mol}}{6 \times 123.22 \text{ g/mol}} = 143.04 \%$$

$$\text{Theoretical weight loss \% due to linker removal} = 143.04 \% - 100\% = 43.04 \%$$

$$\begin{aligned} \text{Theoretical weight \% of } \text{Zr}_6\text{O}_6\text{BTC}_2(\text{CH}_3\text{COO})_6 &= \frac{\text{Zr}_6\text{O}_6\text{BTC}_2(\text{CH}_3\text{COO})_6}{6\text{ZrO}_2} = \frac{1411.78 \text{ g/mol}}{6 \times 123.22 \text{ g/mol}} \\ &= 190.96\% \end{aligned}$$

Theoretical weight loss % due to modulator removal = 190.96% - 143.04 % = 47.92 %

$$\begin{aligned} \text{Theoretical weight \% of } \text{Zr}_6\text{O}_4(\text{OH})_4\text{BTC}_2(\text{CH}_3\text{COO})_6 &= \frac{\text{Zr}_6\text{O}_4(\text{OH})_4\text{BTC}_2(\text{CH}_3\text{COO})_6}{6\text{ZrO}_2} \\ &= \frac{1447.82 \text{ g/mol}}{6 \times 123.22 \text{ g/mol}} \\ &= 195.83\% \end{aligned}$$

Theoretical weight loss % due to de-hydroxylation of metal node = 195.83% - 190.96%
= 4.87%

The experimentally determined weight removal percentages were indicated in Figure 4.11.

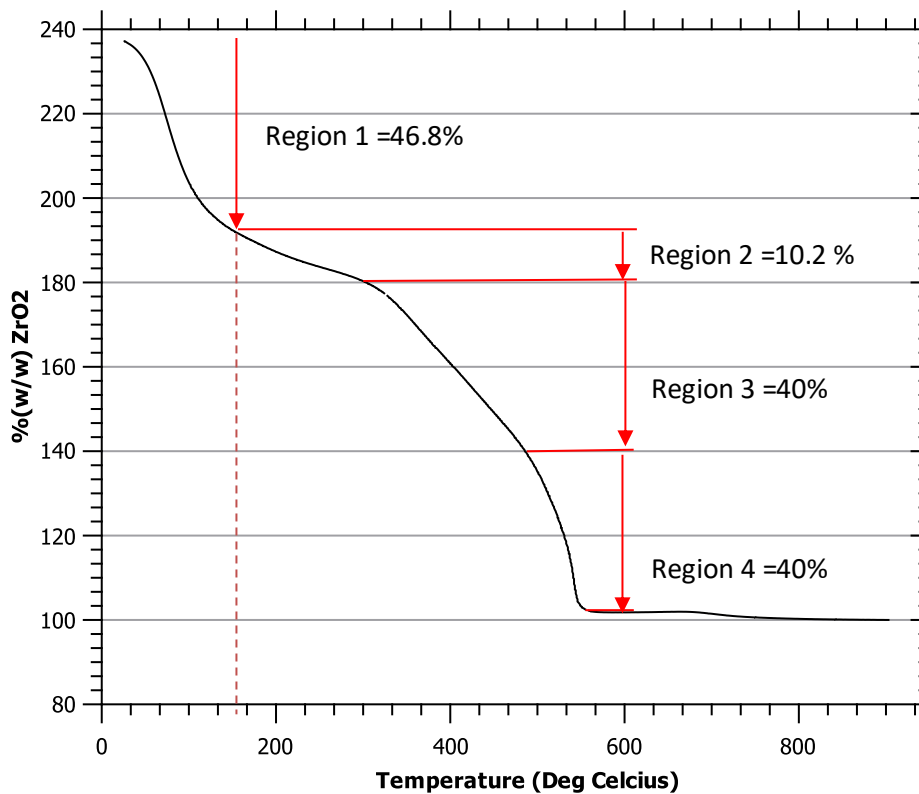


Figure 4.11. Calculation of experimental weight % of regions for MOF-808-acetate

The theoretical and experimental results can be compared to identify the defects in the synthesis as shown in Table 4.5. The theoretical weight losses due to linker and modulator removals were slightly higher than that of respective experimental removals, indicating less linker and modulator in MOF-808. The experimental de-hydroxylation was higher than the theoretical, indicating that other components such as associated chlorides modulators had also decomposed in the considered region. According to the TGA, the activation temperature for MOF-808-acetate was considered 160 °C, which removes the solvent and unreacted modulator content in the pores, which is 46.8 % with respect to the ZrO₂ weight.

Table 4.5. Comparison of theoretical and experimental weight loss percentages.

Removing component	Theoretical weight loss %	Experimental weight loss %
Linker	43.04	40
Modulator	47.92	40
de-hydroxylation in metal node	4.87	10.2

Figure 4.12 shows the TGA for several batches of MOF-808-acetate, which gave consistent TGA curves overlapping with each other with slight variations in solvent and unreacted modulator removing region (region 1).

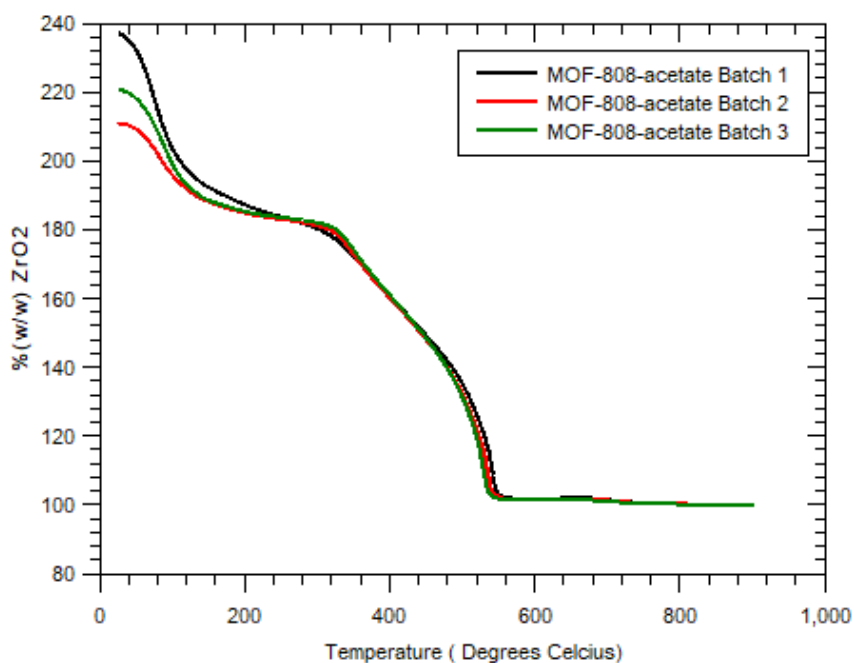


Figure 4.12. TGA curves for synthesized MOF-808-acetate batches

Figure 4.13 displays the TGA curves for the modified MOF-808. The linker removal (region 4) was the only similar region in the modified MOF-808. At the same time, the rest of the curves deviated, showing different thermal properties due to the difference in solvent amounts and the type of modulator. According to the TGA curves, the thermal stability of all the MOFs were maintained until 200 °C. MOF-808-EDTA lost its thermal stability around 200 °C, MOF-

808-benzoate and MOF-808-DHBA around 280 ° C and finally MOF-808-acetate around 350 °C, indicating the difference of modulators present in MOF-808.

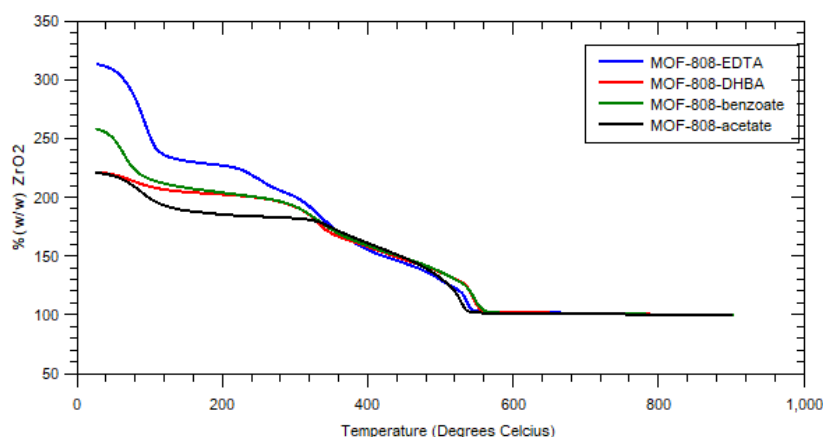


Figure 4.13. TGA curves for MOF-808 types

4.3.4 SEM analysis

Figure 4.14 displays the SEM images at a magnification of around 5000 for MOF-808-acetate before the adsorption experiment and MOF-808-acetate, MOF-808-EDTA, and MOF-808-benzoate after the adsorption experiment in citric acid leaching media. These images indicated that the MOF-808 varieties possessed the same octahedral morphology even after the adsorption experiment. However, a floc formation was observed in the samples after adsorption.

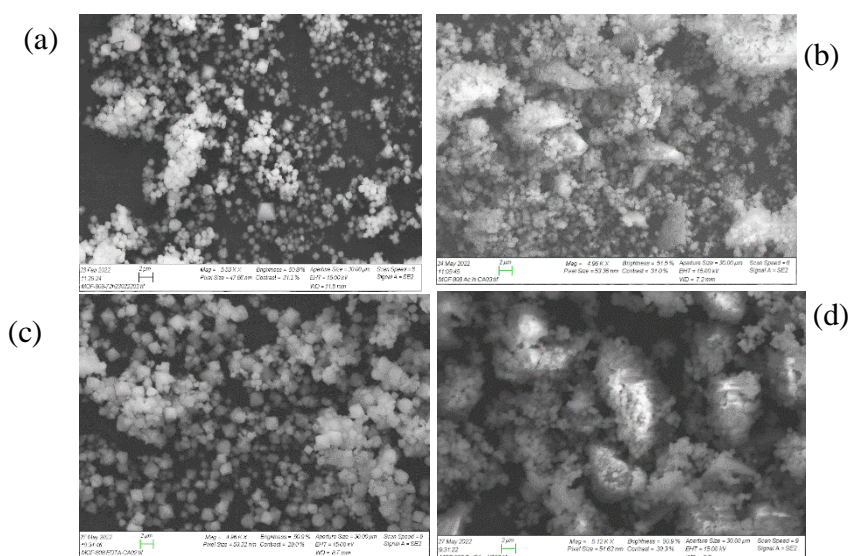


Figure 4.14. SEM images for MOF-808-acetate (a) as synthesized (b) after adsorption in citric acid black mass leachate. MOF-808-EDTA (c) as synthesized (d) after adsorption in citric acid black mass leachate

4.3.5 Nitrogen sorption analysis

Figure 4.15 shows nitrogen adsorption (filled marker) and desorption isotherms (non filled marker) for MOF-808-acetate and modified MOFs. The curves are in IUPAC type I (Langmuir) isotherm. However, MOF-808-acetate showed two steps slightly deviating from type I isotherm due to the presence of both mesopores (2-50 nm) and micropores (< 2 nm). It was considered that zirconium precursor modified the average mesopore size of MOF-808 (Ardila-Suárez et al., 2019). When the MOF-808-acetate was subjected to modifications by ligand exchange by more bulky groups, the large adamantane-shaped pores got partially filled, resulting in pore sizes in the range of micropores (Aunan et al., 2021). Therefore, the modified MOF-808 followed the type I adsorption isotherm well.

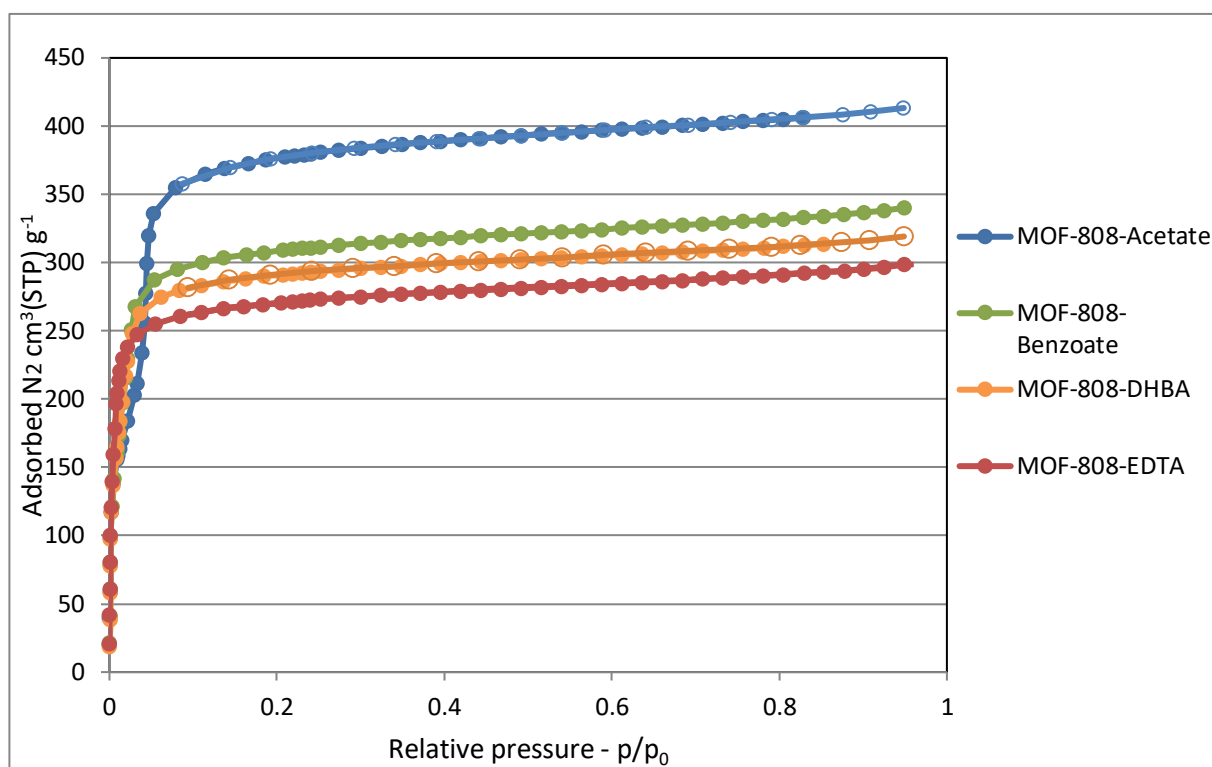


Figure 4.15. Nitrogen sorption isotherms for MOF-808

Table 4.6 summarized the results obtained by calculating BET surface area, total pore volume, and monolayer pore volume for the four adsorbents (Appendix 5). The BET surface area was used here for comparison purposes, but the BET surface area was not a meaningful term for microporous adsorbents (Rouquerol et al.). According to the previous studies, MOF-808 was reported with a BET surface area of over 2000 m²/g (Furukawa et al., 2014; Liu et al., 2019; Y. Peng et al., 2018). The deviation of BET surface area was possibly due to the insufficient degassing and inaccuracy of plotting the BET curve with three points. However, the MOF-808-

EDTA resulted in a closer BET surface area value, as reported in (Y. Peng et al., 2018). Compared to MOF-808-acetate, the modified MOFs had lower BET surface area and pore volumes due to the bulky ligands introduced. Due to the attached hydroxyl groups, the BET surface area and pore volumes of MOF-808-DHBA were lower than MOF-808-benzoate.

Table 4.6. Calculated properties from BET curve equation of MOF-808

Adsorbent	BET surface area (m ² /g)	Total pore volume (cm ³ /g) at 0.94 P/P _o	Monolayer pore volume (V _m) (cm ³ (STP)/g)	Correlation coefficient
MOF-808-acetate	1548	0.637	356	0.9977
MOF-808-EDTA	1101	0.459	253	0.9995
MOF-808-DHBA	1175	0.491	270	0.9995
MOF-808-benzoate	1262	0.523	290	1.0000

4.3.6 NMR analysis

The molar ratios of species present in MOFs such as linker, modulator and the functional groups (ligands) were summarized as follows in Table 4.7. The detailed calculations and the spectra are included in appendix 6.

Table 4.7. Summary of NMR quantified molar ratios for MOF-808

Sample	Linker	Modulator (Mod.)	Functional group (FG)	$\left(\frac{\text{Mod.}}{\text{BTC}}\right)m_R$	$\left(\frac{\text{FG}}{\text{BTC}}\right)m_R$	Total m_R
MOF-808-acetate	Trimesic acid (BTC)	Acetic acid		2.28		
MOF-808-benzoate	Trimesic acid (BTC)	Acetic acid	Benzoic acid	0.14	2.55	2.69
MOF-808-EDTA	Trimesic acid (BTC)	Acetic acid	EDTA-2Na		2.61	2.61

4.4 Characterization of resins

The resin in as received and pretreated forms were characterized by N₂ sorption, IR, and SEM-EDS.

4.4.1 Nitrogen sorption (BET) analysis

Figure 4.16 shows the nitrogen adsorption (filled marker) and desorption isotherms (non-filled marker) of resin in as received and acid-treated forms. The curves were in IUPAC type II isotherm, where it formed a monolayer and then changed into a multi-layer. The two isotherms consisted of similar variation, with acid-treated resin having a slightly higher BET surface area, as shown in Table 4.8. The BET surface area of the resin was recorded as 19.68 m² g⁻¹ previously in (Wan et al., 2014), which is lower than the results obtained in this study. The difference is possibly due to the inaccuracy in selected points in the BET curve.

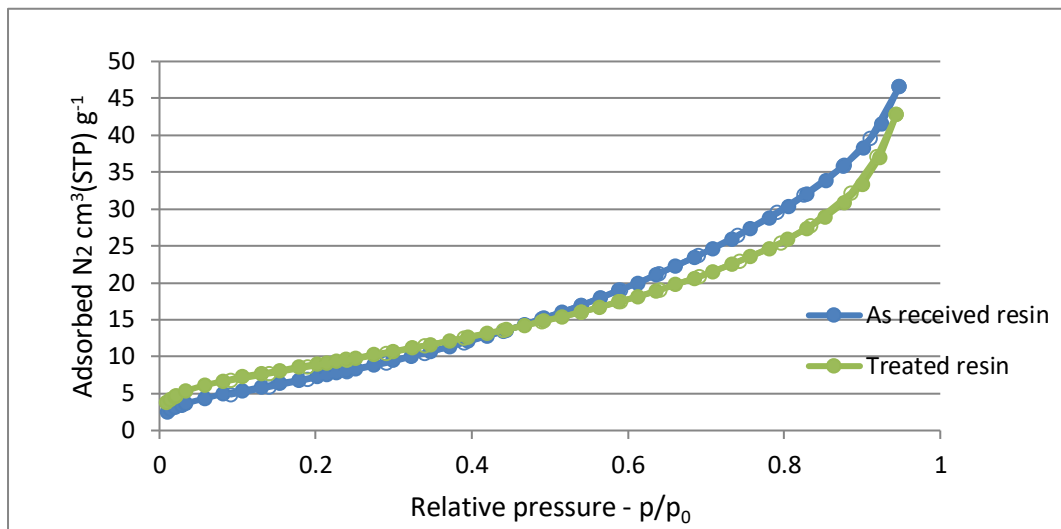


Figure 4.16. Nitrogen sorption isotherms for resins as received and treated

Table 4.8. Calculated properties from BET curve equation for resins

Adsorbent	BET surface area (m ² /g)	Total pore volume (cm ³ /g) at 0.94 P/P _o	Monolayer pore volume (V _m) (cm ³ (STP)/g)	Correlation coefficient
Amberlite IRC 748(as received)	29	0.064	7	0.9977
Amberlite IRC748 (acid-treated)	34	0.057	8	1.0000

4.4.2 IR analysis

Figure 4.17 shows ATR-IR spectra of as received resin and acid-treated resin. The wavenumbers 1580, 1400, and 1300 with intense peaks were assigned to C-N, C=O, and C-H, respectively, which are the characteristic bonds present in the iminodiacetic acid group resin. According to the spectrum for acid-treated resin, the functional groups of resins have been reduced drastically due to the 1 M H₂SO₄ pretreatment. Also, the region 3600-3200 cm⁻¹ corresponding to the stretching vibration of O-H of water molecules and carboxylic groups were absent in the acid-treated resin.

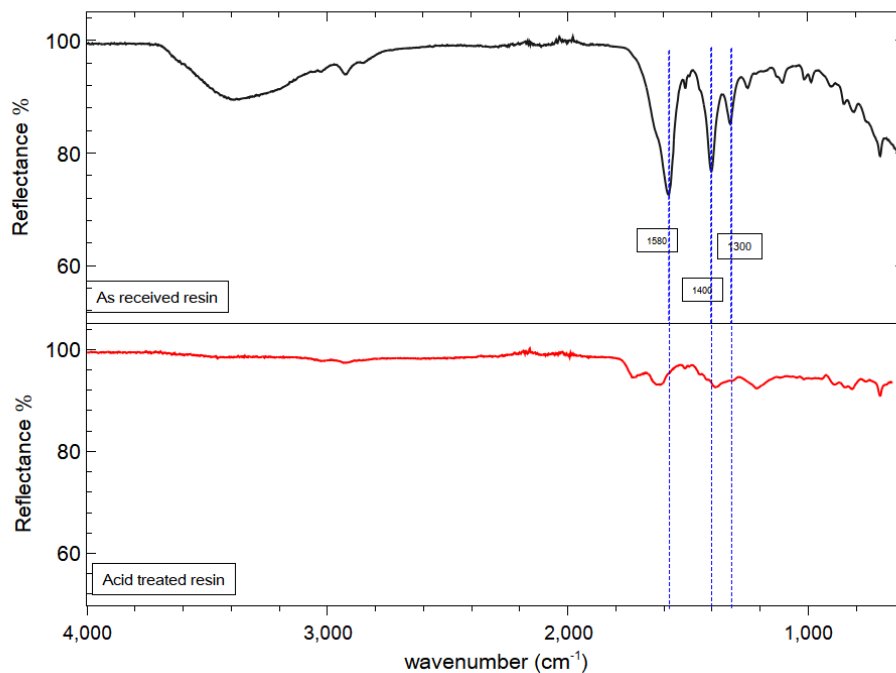


Figure 4.17. ATR-IR spectra for resins

4.5 Black mass leaching experiments

The composition of black mass leachates obtained from different acids and pH profiles of some acids are analyzed here.

4.5.1 Leachate compositions and leaching efficiencies

Table 4.9 illustrates the black mass metal composition in weight percent - % (w/w) with respect to the weight of black mass for different leaching media. A common unit with respect to the black mass amount used was necessary to compare among the leaching media because different solid to liquid ratios were used for the leaching. According to previous studies, aqua regia digestion was considered to be leaching the metals totally into the liquid phase (Xiangping Chen et al., 2019; Dorella & Mansur, 2007). Therefore, the leachate compositions were compared

with aqua regia digestion to have an overview of the percentage efficiency of leaching as tabulated in Table 4.10.

Table 4.9. Metal composition of black mass leachates from acids

Leaching media	Al	Co	Cu	Fe	Li	Mn	Ni	B	Ca	K	Mg	Si	Zn
	%(w/w)												
Aqua regia	4.45	6.25	5.55	0.9	3.3	5.3	20.3	0	0.4	0.2	0.5	0	0.5
H ₃ PO ₄ (0.8 M)	1.8	2.3	2.1	0.3	2.4	3	4.5	0	0.2	0.1	0.2	1	0.3
H ₃ PO ₄ (0.6 M)	2	2.6	2.3	0.2	2.6	3.3	4.8	0	0.2	0.1	0.2	1	0.3
Tartaric acid (C ₄ H ₆ O) (0.5 M)	3.05	2.5		0.45	3.15	5.05	4.95	0	0.35	0.1	0.35	1.35	0.25
Sulfuric acid (H ₂ SO ₄) (2.0 M)	4.9	5		0.7	3.6	5.5	12.6	0	0.5	0.2	0.6	0.1	0.5
Citric acid (2.0 M)	2.8	3.2		0.5	3.3	4.7	6.3						

Table 4.10. Metal leaching efficiencies of black mass leachates from acids

Leaching media	Al	Co	Cu	Fe	Li	Mn	Ni	Ca	K	Mg	Zn
	Efficiency %										
H ₃ PO ₄ (0.8 M)	40.4	36.8	37.8	33.3	72.7	56.6	22.2	50	50	40	60
H ₃ PO ₄ (0.6 M)	44.9	41.6	41.4	22.2	78.8	62.3	23.6	50	50	40	60
Tartaric acid (C ₄ H ₆ O) (0.5 M)	68.55	40		50	95.45	95.25	24.4	87.5	50	70	50
Sulfuric acid (H ₂ SO ₄) (2.0 M)	110.1	80		77.8	109.1	103.8	62.1	125	100	120	100
Citric acid (2.0 M)	62.9	51.2		55.6	100	88.7	31				

Sulphuric acid leachate resulted in 100 % leaching efficiencies for metals except copper, nickel, iron, and cobalt. The leaching efficiencies for sulphuric acid were higher than 100 % for some metals, which indicated aqua regia digestion was not leaching out total metal quantity from black mass confirming the presence of residual metals in digested and leached residues as indicated by XRF. The H₃PO₄ leaching with a concentration of 0.6 M gave better efficiencies for all the considered metals. However, by considering the ability to optimize the media's leaching efficiency and environmental sustainability, citric acid and tartaric acid were used in further analysis. Figure 4.18 displays a bar graph of leaching efficiency percentage metals of significant quantities in black mass with respect to the selected leaching media. Both citric and

tartaric acids gave leaching efficiencies closer to each other. Citric acid showed higher leaching efficiencies with cobalt, iron, lithium and nickel, while tartaric acid showed higher leaching efficiencies with aluminium and manganese. However, the leaching efficiencies can be further enhanced in both organic acids by varying leaching parameters such as concentration of acid, time, temperature, and solid-liquid ratio.

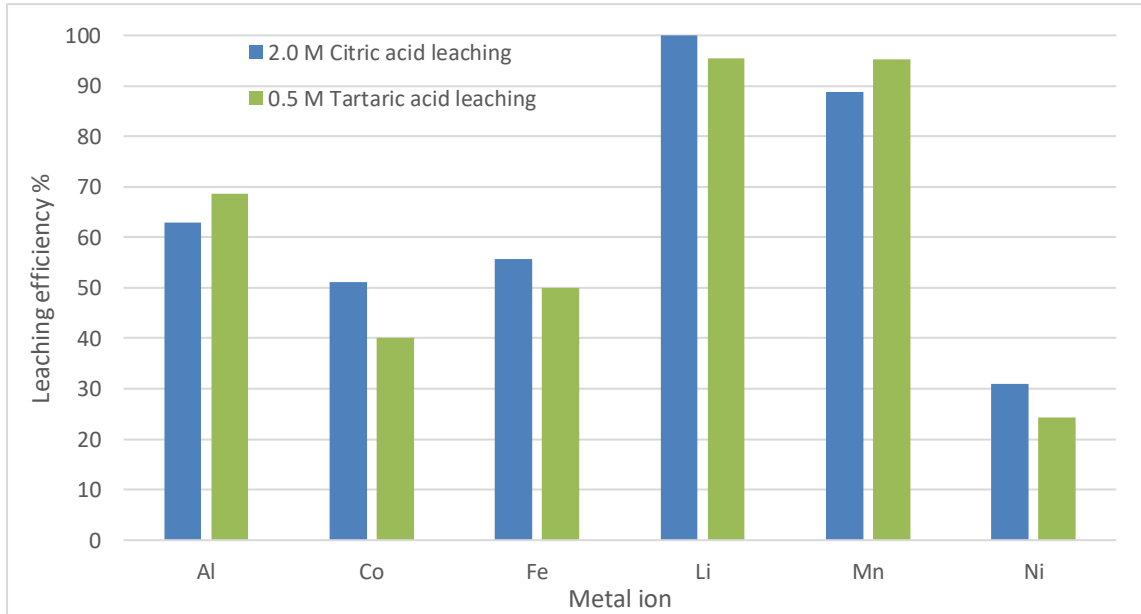
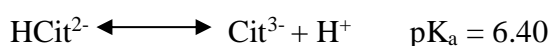


Figure 4.18. Black mass leaching efficiency of citric and tartaric acid

4.5.2 Acid pH profiles

Figures 4.19 to 4.21 indicate the pH profiles obtained when adding 1 M NaOH to 20 mL of acid solutions used at their respective concentrations used in black mass leaching.

Figure 4.19 shows the pH profile of citric acid with the volume of 1 M NaOH added. The initial pH of 2 M citric acid was 1.86. Volumes of 2 mL, 40 mL and 80 mL of 1 M NaOH were required to make the acid solution pH 2, 4 and 6, respectively. This pH adjustment increased the amount of sodium ions in the acid solution, which may have affected the transition metal adsorption from the leachate. The higher base volume consumption in citric acid was expected due to the existence of following equilibrium dissociations (Xiangping Chen et al., 2016).



There was no precipitate observed until pH 11, where a slight precipitation started to form.

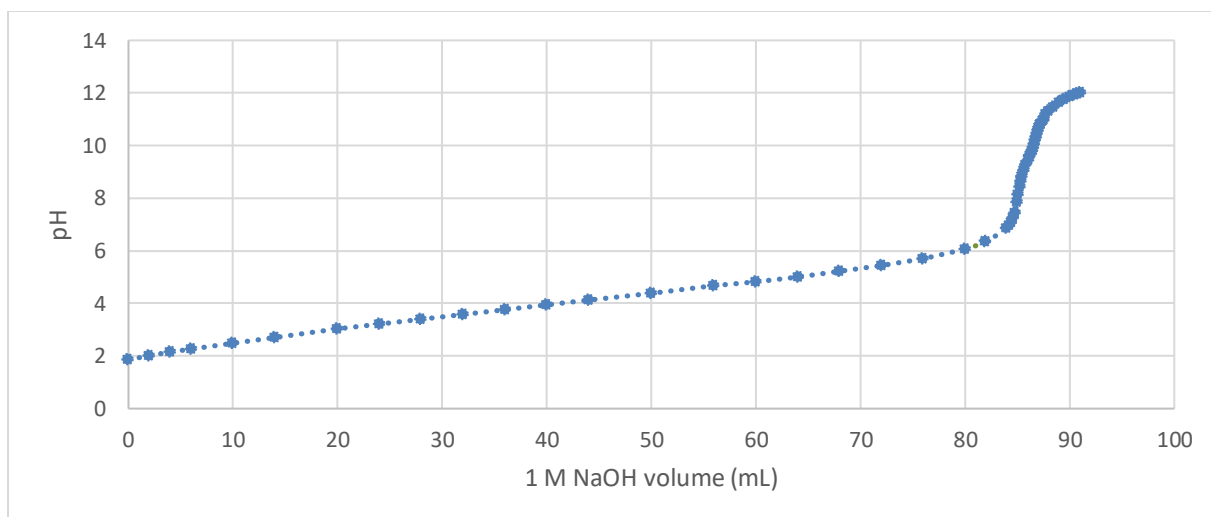


Figure 4.19. pH profile for citric acid with volume of 1 M NaOH

Figure 4.20 shows the pH profile of tartaric acid with the volume of 1 M NaOH added. Tartaric acid showed quicker responses in pH when the base was added compared to citric acid. A colour change was observed at pH 8, but no precipitate resulted. Slight sedimentation was observed when the final pH 12 adjusted tartaric acid solution was kept overnight.

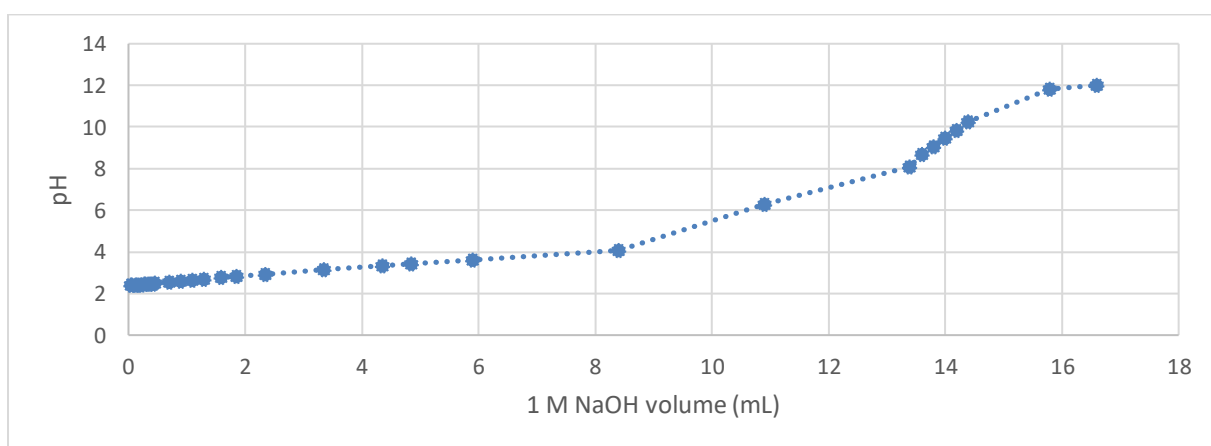


Figure 4.20. pH profile for tartaric acid with volume of 1 M NaOH

Figure 4.21 shows the pH profile of phosphoric acid with the volume of 1 M NaOH added. From the initial drop of base added, there was a precipitate formation. The acid solution pH reached 6 with 5.5 mL of NaOH using the lowest amount of base with respect to the other two acids.

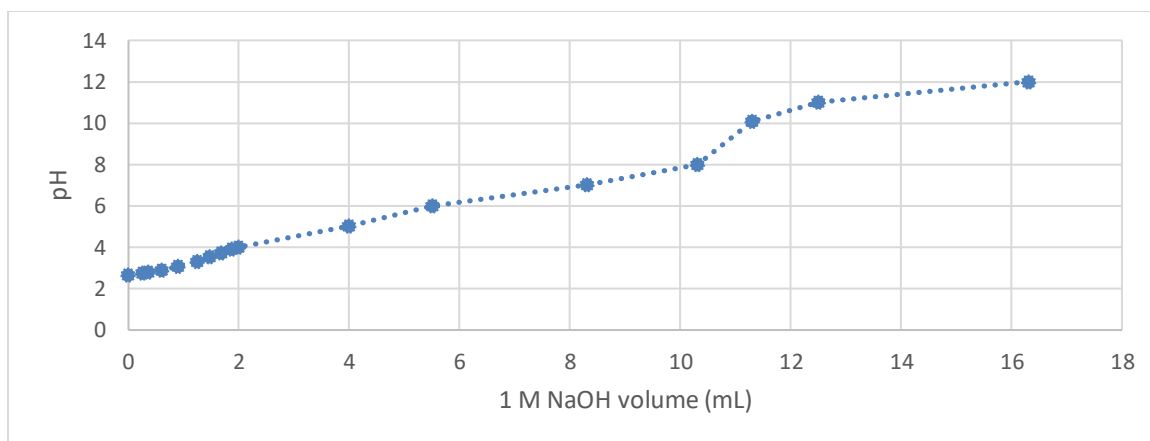


Figure 4.21. pH profile for phosphoric acid with volume of 1 M NaOH

However, to decide the best leaching media, the chemical stability of adsorbent in acids was the critical factor to be considered.

4.6 MOF chemical stability in black mass leachates

Figure 4.22 shows the XRD spectra used to determine the chemical stability of MOF-808-acetate in acid concentrations used for leaching of black mass. The XRD spectra of as-synthesized MOF-808-acetate were compared with the spectra of MOF-808-acetate after 24 h stirring with the acids to determine the stability.

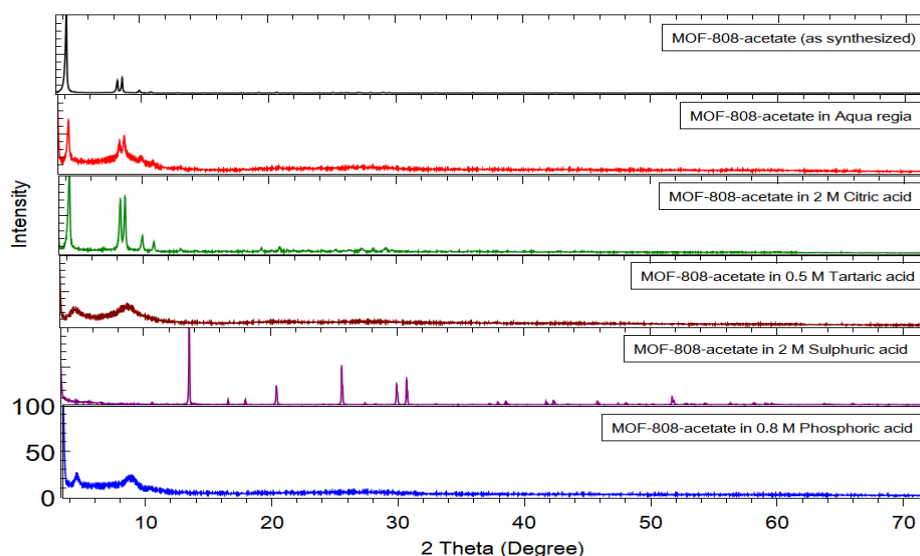


Figure 4.22. XRD of MOF-808-acetate after adsorption experiments in black mass leachates

According to the spectra, all the acid stirred MOF-808-acetate samples except citric acid resulted in different spectral lines forming new peaks or completely removing peaks compared to as-synthesized MOF-808-acetate. Therefore, according to XRD analysis, only the MOF-

808-acetate sample stirred in citric acid was chemically stable. Therefore, citric acid black mass leachate was selected for adsorption experiments.

Figures 4.23 show the normalized XRD spectra of MOF-808-acetate in citric acid without metals and with metals, respectively, at different pH values adjusted using 1 M NaOH. The XRD spectrum of as-synthesized MOF-808-acetate was compared with the spectra of MOF-808-acetate after 24 h of stirring with the pH-adjusted citric acid (without metals) and citric acid black mass leachate (with metals) to determine the stability. All the spectra except MOF-808-acetate in pH 11 adjusted black mass citric acid leachate showed peaks similar to the MOF-808-acetate as synthesized sample in the region less than 12° of 2θ . However, the relative intensities between peaks in the same spectrum were different for all the samples compared to MOF-808-acetate as synthesized sample. At higher 2θ values, a spectral noise was observed, which was much higher in the samples with metals, indicating the effect of the presence of metals for the analysis.

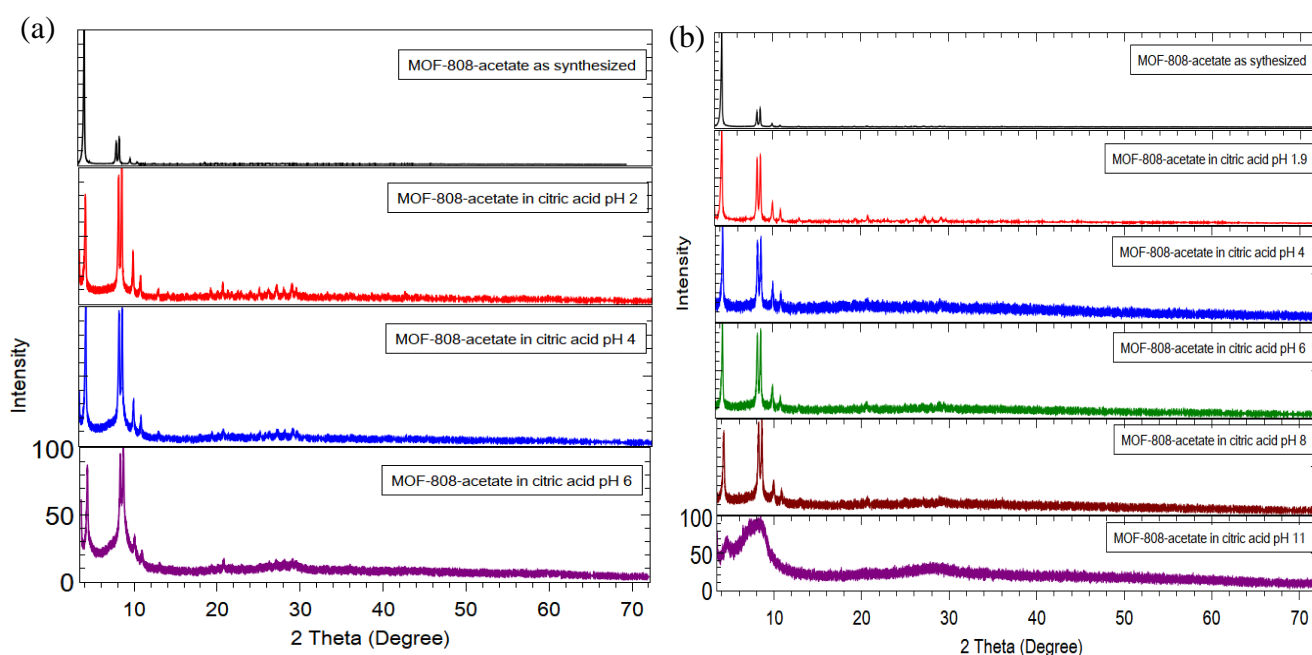


Figure 4.23. XRD spectra of MOF-808-acetate after 24 h stirring in pH adjusted (a) citric acid without metals (b) citric acid leached black mass metal solution

The chemical stability of MOF-808-acetate in pH-adjusted samples were difficult to determine only by XRD analysis. Therefore, more data from N_2 sorption, TGA and NMR analysis were required to conclude chemical stability.

4.7 Adsorption experiments

This section presents and discusses the nickel and cobalt uptake results of resins and MOFs in simulated metal solutions by adsorption and ion exchange.

4.7.1 Calibration curves

The UV-visible spectrophotometer was used to analyze cobalt and nickel from the metal ions present in the black mass. Manganese also resulted a detectable peak with UV-visible spectrophotometer, but the concentration range of the leached metal solutions were resulting low absorbance values without significant difference to distinguish between them.

4.7.2 Cobalt calibration curves

Figure 4.24 (a) and 4.24 (b) show the UV-visible spectra and the calibration curve, respectively, for cobalt. The spectra showed a clear peak for cobalt at 511 nm. A calibration curve was prepared from the absorbance at 511 nm. A linear trendline was drawn to fit the data set, which gave a correlation coefficient of 0.99999.

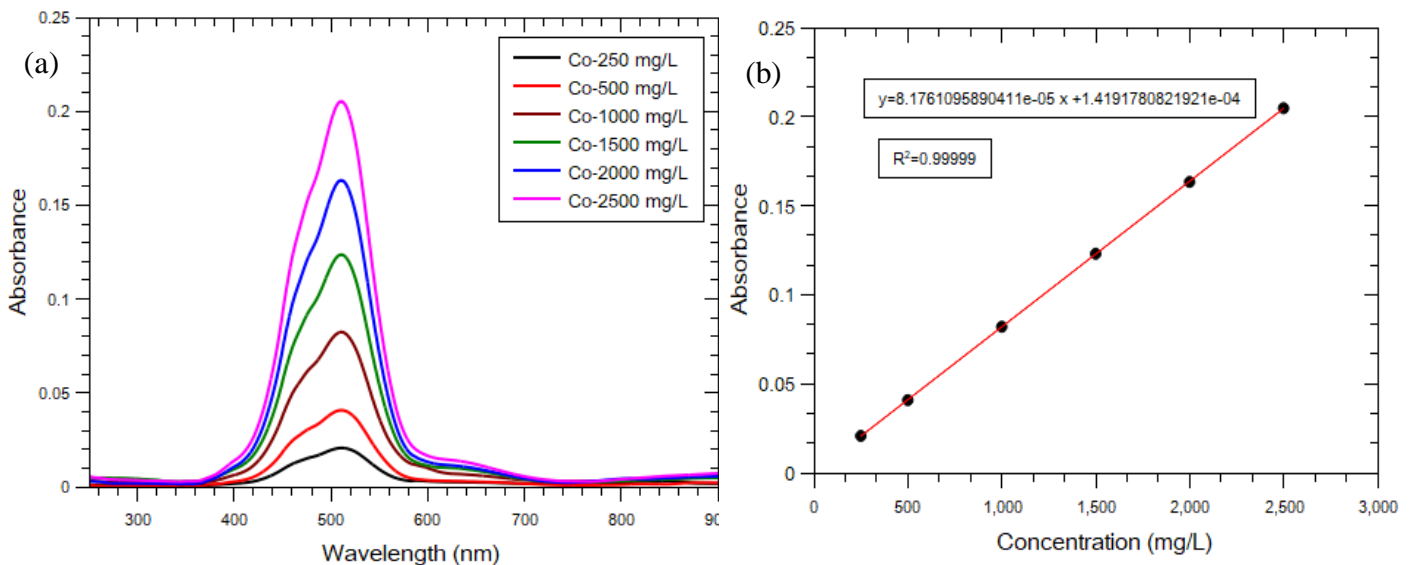


Figure 4.24. (a) UV-visible spectra for cobalt (b) Calibration curve for absorbance vs concentration for cobalt in concentration range 250-2500 mgL^{-1}

The equation 15 derived from the linear trendline equation was used to convert the absorbance values obtained in experiments to the cobalt concentrations.

$$\text{Co}^{2+} \text{ concentration } \left(\frac{\text{mg}}{\text{L}} \right) = \frac{(\text{Absorbance at } 511 \text{ nm} - 0.0001419178)}{0.0000817611} \quad (15)$$

4.7.3 Nickel calibration curves

Figure 4.25 (a) and 4.25 (b) show the UV-visible spectra and the calibration curve, respectively, for nickel. The spectra showed the highest peak for nickel at 394 nm. A calibration curve was prepared from the absorbance at 394 nm. A linear trendline was drawn to fit the data set, which gave a correlation coefficient of 0.99996.

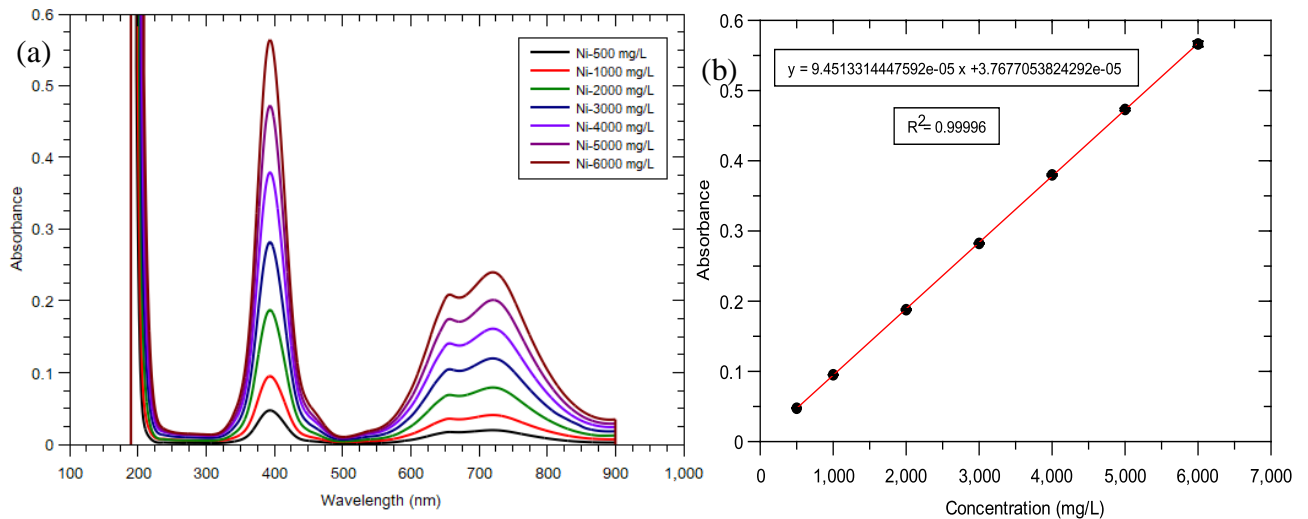


Figure 4.25. (a) UV-visible spectra for nickel (b) Calibration curve for absorbance vs concentration for nickel in concentration range 500-6000 mgL⁻¹

The equation 16 derived from the linear trendline equation was used to convert the absorbance values obtained in experiments to the nickel concentrations.

$$Ni^{2+} \text{ concentration } \left(\frac{mg}{L} \right) = \frac{(Absorbance \text{ at } 394 \text{ nm} - 0.00003767705)}{0.00009451331} \quad (16)$$

4.8 Ion-exchange experiments for resins in single metal solutions

Batch experiments were carried out in nickel and cobalt separate solutions to determine the effect of pH, time, temperature, and liquid-solid ratio. The factor relative selectivity between two metal ions was not discussed in this section because the metal ions were tested as single-component systems.

4.8.1 Effect of variation of pH

Figures 4.26 (a) and 4.26 (b) show the adsorption capacity of treated resins and resins in as received form at pH values 2, 3, 4 and 5. The adsorption capacity of Ni²⁺ was higher at all the considered pH values than Co²⁺. The resins in as received form showed relatively high adsorption capacities compared to treated resins showing that the ion exchange was enhanced

when the resin was in sodium form. It could be noted that at pH 6, as received resins showed the maximum difference between Ni^{2+} and Co^{2+} adsorption capacities.

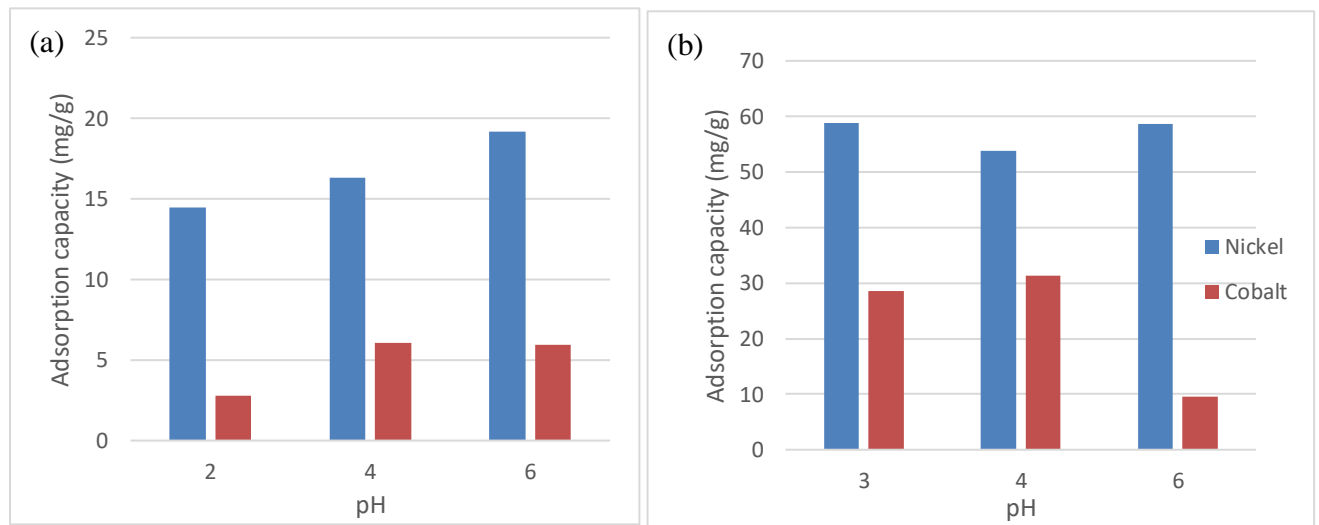


Figure 4.26. (a) Variation of adsorption capacity with pH (a) for treated resins (b) as received resin

Figure 4.27 shows the metal ion removal percentages of Ni^{2+} and Co^{2+} with treated resins and resins in as received form. It was observed that resins in as received form showed a better metal uptake than treated resins. The reduction in metal uptake in treated resins was due to the removal of functional groups during the acid treatment, as shown in ATR-IR spectra in section 4.4.2.

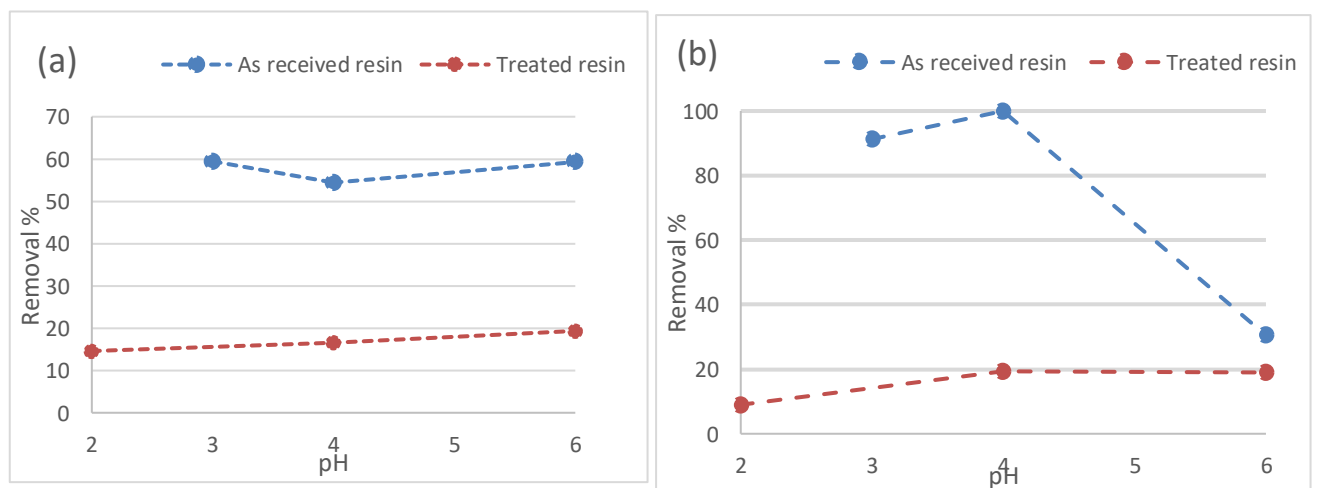


Figure 4.27. Variation of removal percentage with pH (a) for nickel and (b) cobalt for treated and as received resins

Therefore, the resins in as received (Sodium) form were used to determine the effects of other factors. The pH values of 3 and 4, which results in the highest adsorption capacities, were used

for Ni^{2+} and Co^{2+} respectively, for the experiments conducted to determine adsorption kinetics and isotherms.

4.8.2 Effect of variation of temperature

Figure 4.28 (a) and 4.28 (b) show the adsorption capacity and metal ion removal percentage with temperatures of 20, 30, and 40 °C. The parameters did not show a significant variation in the temperatures considered. Therefore, room temperature of 20 °C was used in experiments conducted after this.

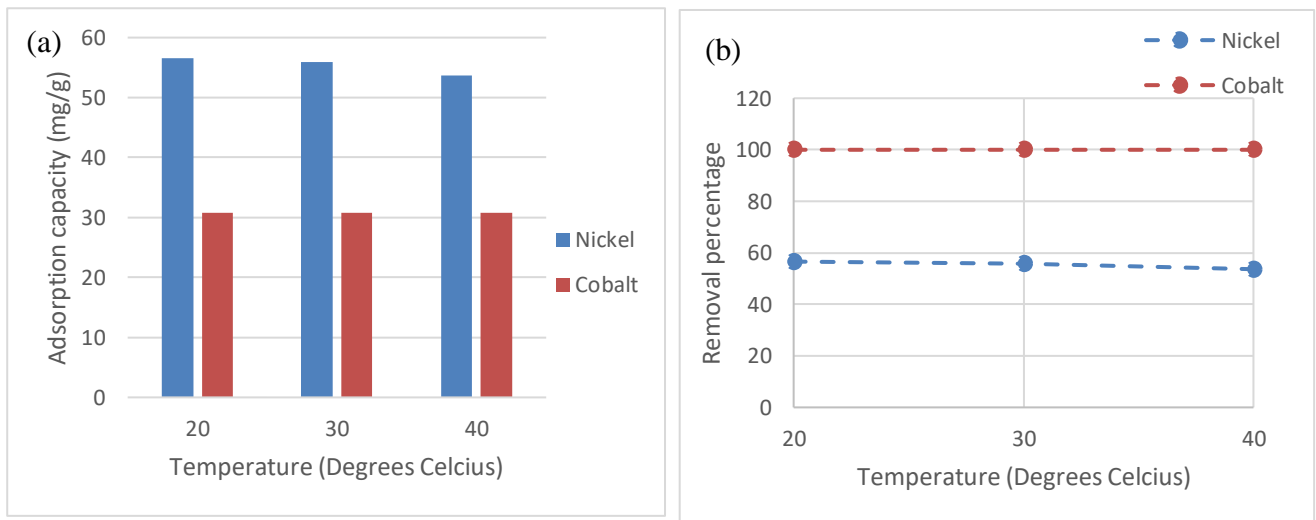


Figure 4.28. Variation of (a) adsorption capacity and (b) removal percentage of Ni^{2+} and Co^{2+} with temperature

4.8.4 Adsorption kinetics

When conducting full-scale experiments, it was necessary to know the rate of metal uptake and the time at which equilibrium conditions were reached. Adsorption kinetic studies were conducted based on pseudo first order and pseudo second order models to determine the parameters of kinetics.

Figure 4.29 (a) and 4.29 (b) show the variation of concentration and adsorption capacity of Ni^{2+} with time. The pH of Ni^{2+} solution was adjusted to 3, as discussed previously. The equilibrium conditions were achieved in 3 h.

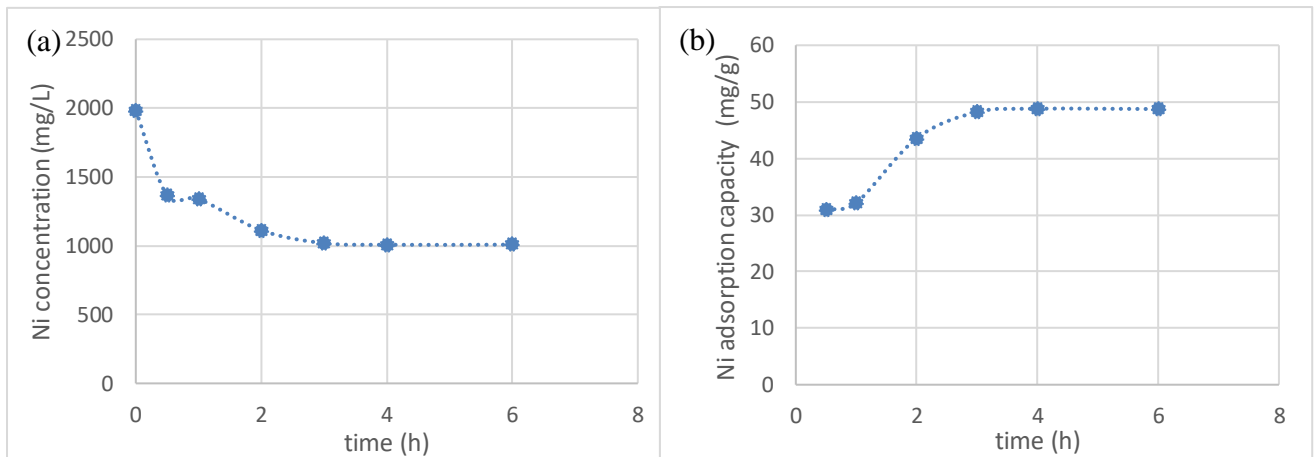


Figure 4.29. Variation of (a) Ni²⁺ concentration and (b) adsorption capacity of Ni²⁺ with time

Figures 4.30 (a) and 4.30 (b) show the plots for the pseudo first order and pseudo second order kinetic models for Ni²⁺ solution. The model equations 6 and 7 were used in plotting the data, and the kinetic parameters were tabulated in table 4.10. The pseudo second order kinetics showed a better correlation with the data points than pseudo first order kinetics.

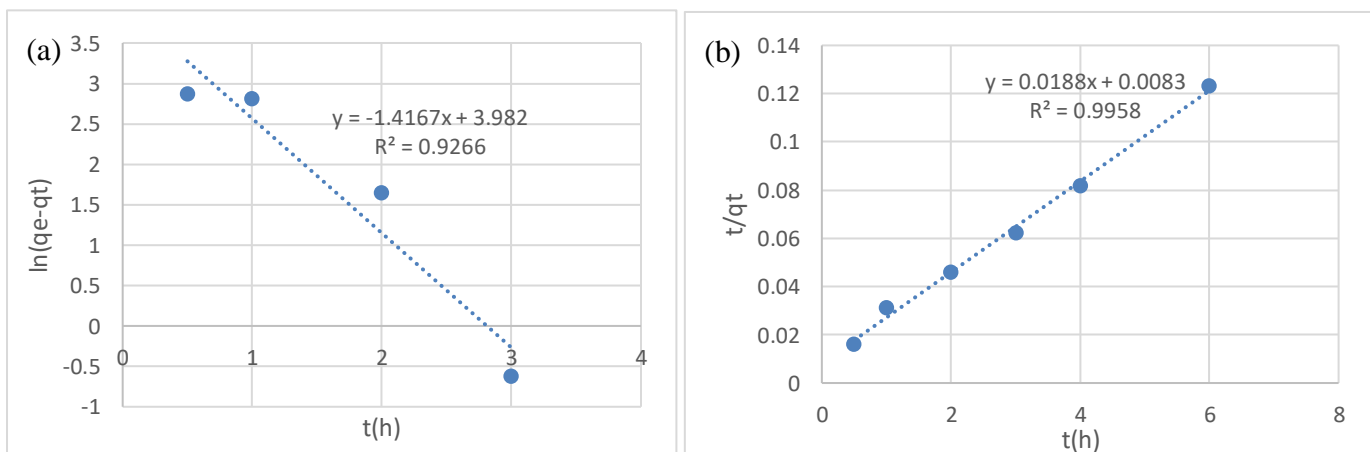


Figure 4.30. (a) Pseudo first order and (b) pseudo second order kinetic models for Ni²⁺

Figure 4.31 (a) and 4.31 (b) show the variation of concentration and adsorption capacity of Co²⁺ with time. The pH Co²⁺ solution was adjusted to 4, as discussed previously. The equilibrium conditions were achieved in 2 h.

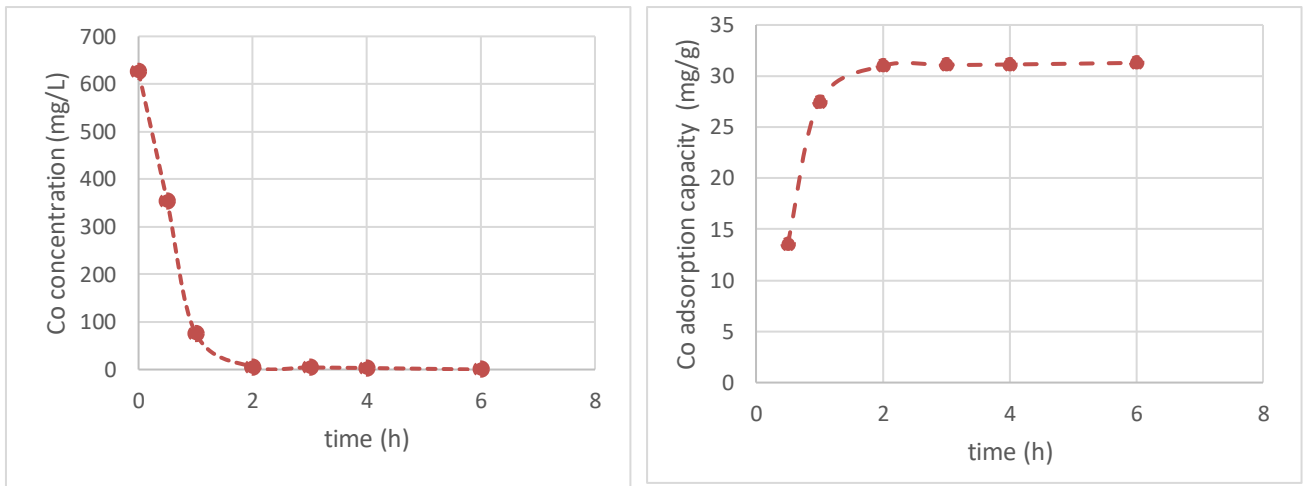


Figure 4.31. variation of (a) Co^{2+} concentration and (b) adsorption capacity of Co^{2+} with time

Figures 4.32 (a) and 4.32 (b) show the plots for pseudo first order and pseudo second order kinetic models for Co^{2+} solution. The model equations 6 and 7 were used in plotting the data, and the kinetic parameters were tabulated in table 4.10. The pseudo second order kinetics showed a better correlation with the data points than pseudo first order kinetics.

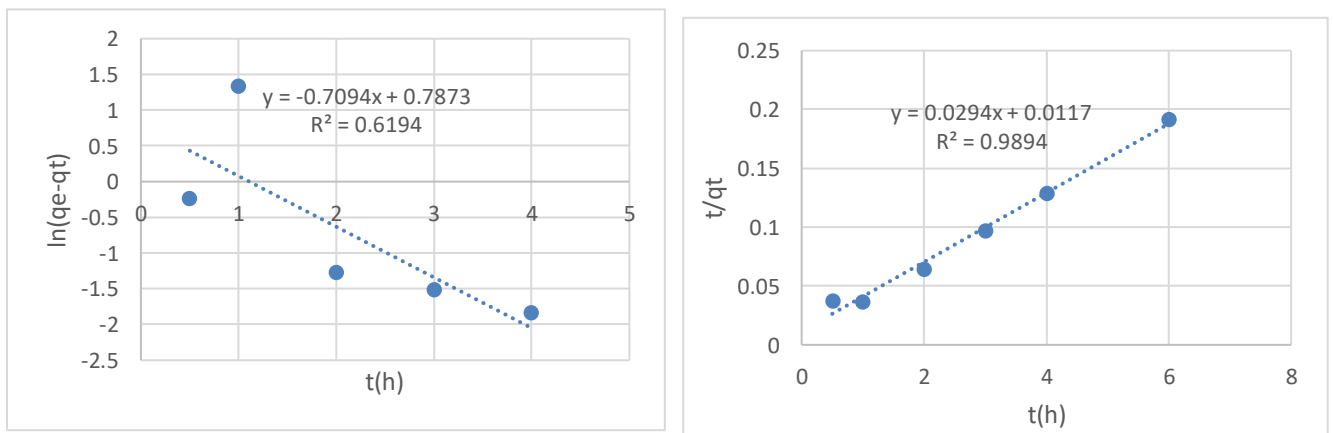


Figure 4.32 (a) Pseudo first order and (b) pseudo second order kinetic models for Co^{2+}

According to table 4.11, when considering better fitting pseudo second order kinetics, the second order rate constant for Ni^{2+} was lower than Co^{2+} indicating lower sorption rate in Ni^{2+} . However, the equilibrium adsorption capacity was higher in Ni^{2+} compared to Co^{2+} .

Table 4.11. Calculated parameters from the kinetic models

Metal ion	Pseudo first order			Pseudo second order		
	K_1 (h ⁻¹)	q_e (mg g ⁻¹)	R^2	K_2 (g mg ⁻¹ h ⁻¹)	q_e (mg g ⁻¹)	R^2
Ni ²⁺	1.4167	48.73	0.9266	0.0426	53.19	0.9958
Co ²⁺	0.7094	14.36	0.6194	0.0739	34.01	0.9894

4.8.5 Adsorption isotherms

When optimizing the adsorption process in resins, it is important to know the behaviour of metals in solution with the resins. The adsorption isotherms represent the residual metal concentrations in the solution with the adsorbed metal amount to the resin.

The adsorption experimental and model adsorption isotherms for Ni²⁺ were plotted in figure 4.33. The model equations of Langmuir and Freundlich were plotted using non-linear regression using the solver tool in excel by the least square method. Freundlich isotherm showed the best fit for the experimental isotherm. The sums of difference of squares were 87.3 and 252.1 for Freundlich and Langmuir isotherms, respectively, which confirmed that the Freundlich isotherm was the best fit among the two isotherms.

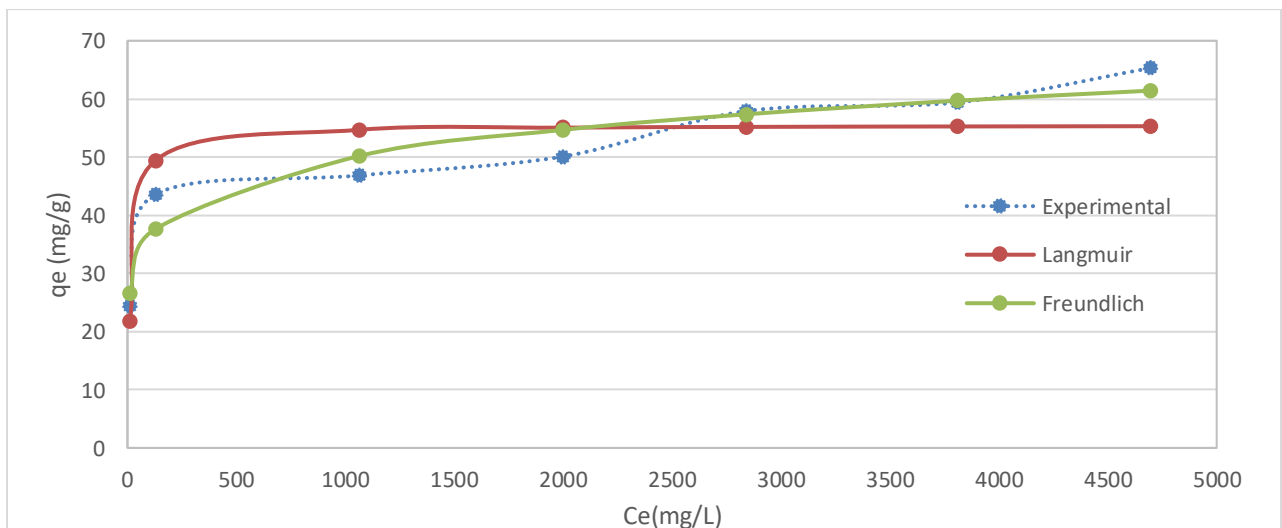


Figure 4.33. Experimental and model adsorption isotherms for Ni²⁺

Figure 4.34 (a) and 4.34 (b) represent linear regression plots of Langmuir and Freundlich isotherms, respectively. The Langmuir isotherm had a higher correlation coefficient than the Freundlich isotherm in the linear plots. In contrast, the Langmuir isotherm resulted in a lower fit in non-linear regression due to the unsteady maximum adsorption capacity obtained from experimental data.

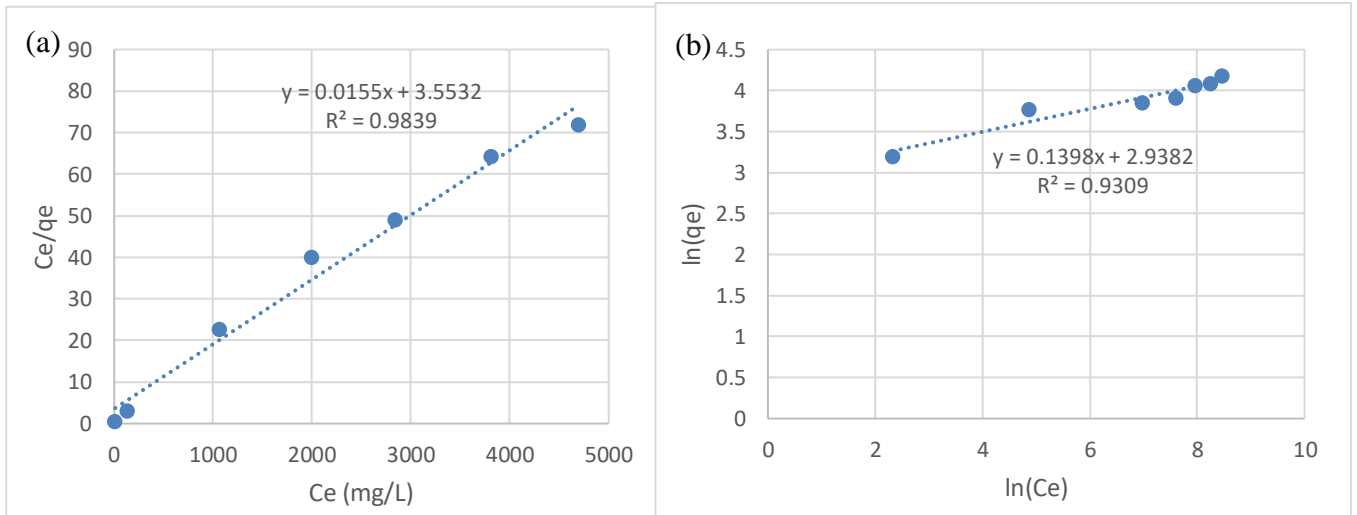


Figure 4.34. (a) Langmuir and (b) Freundlich isotherm linear plots for adsorption isotherms of Ni^{2+}

However, by considering the behaviour of the experimental adsorption isotherm, it was considered that the Langmuir isotherm represented the adsorption isotherm for resins in Ni^{2+} . Table 4.12 represents the parameters of model isotherms. A maximum Ni^{2+} adsorption capacity of 64.52 mg g^{-1} was obtained from the linear regression Langmuir model.

Table 4.12. Calculated parameters from Ni^{2+} adsorption isotherm models

Model	parameter	Nonlinear regression	Linear regression
Langmuir	$q_m \text{ (mg g}^{-1}\text{)}$	55.50	64.52
	$k_l \text{ (L mg}^{-1}\text{)}$	0.0632	0.0044
Freundlich	$k_f \text{ (mg g}^{-1} \text{ (L mg}^{-1}\text{)}^{1/n}\text{)}$	19.43	18.88
	$1/n$	0.1361	0.1398

The adsorption experimental and model adsorption isotherms for Co^{2+} were plotted in figure 4.35. The model equations of Langmuir and Freundlich were plotted using non-linear regression using the solver tool in excel by the least square method. Langmuir isotherm showed the best fit for the experimental isotherm. The sums of difference of squares were 524.8 and

324.2 for Freundlich and Langmuir isotherms, respectively, which confirmed that the Langmuir isotherm was the best fit among the two isotherms.

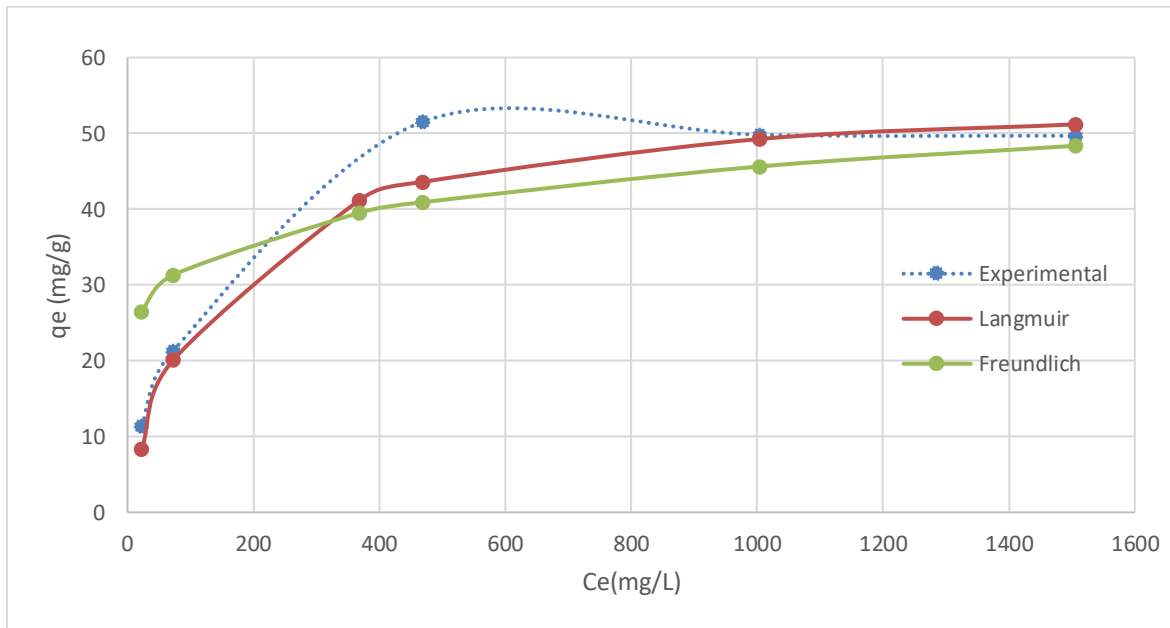


Figure 4.35. Experimental and model adsorption isotherms for Co^{2+}

Figure 4.36 (a) and 4.36 (b) represent linear regression plots of Langmuir and Freundlich isotherms, respectively. The Langmuir isotherm had a higher correlation coefficient than the Freundlich isotherm in the linear plots.

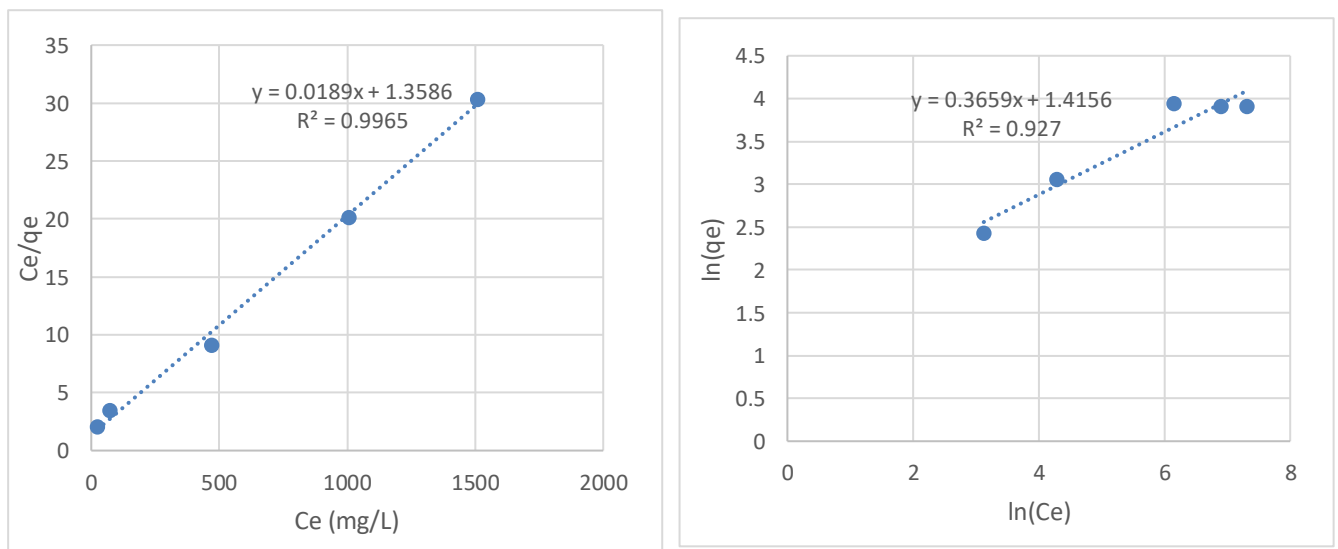


Figure 4.36. (a) Langmuir and (b) Freundlich isotherm linear plots for adsorption isotherms of Co^{2+}

Therefore, the Langmuir isotherm represented the adsorption isotherm for resins in Co^{2+} . Table 4.13 represented the parameters of model isotherms. A maximum Co^{2+} adsorption capacity of 52.91 mg g^{-1} was obtained from the linear regression Langmuir model.

Table 4.13. Calculated parameters from Co^{2+} adsorption isotherm models

Model	Parameter	Nonlinear regression	Linear regression
Langmuir	qm	55.56	52.91
	k_1	0.0078	0.0139
Freundlich	kf	16.95	4.12
	1/n	0.1433	0.3659

4.9 Ion-exchange experiments for resin in Ni^{2+} and Co^{2+} mixed simulated solution

Batch experiments were carried out in Ni^{2+} and Co^{2+} mixed solution to determine the effect of pH, time and liquid-solid ratio. The relative selectivity of Ni^{2+} with respect to Co^{2+} was reported and discussed in this section for the solution containing two metal ions and to determine the degree of selectivity.

4.9.1 Effect of variation of pH

Figures 4.37 (a) and 4.37 (b) show the adsorption capacity and metal ion removal percentages, respectively, for two adsorption cycles for resins in as received form at pH values 2, 3, 4, 5, 6, and 7. The adsorption capacity of Ni^{2+} was higher at all the considered pH values compared to Co^{2+} . The first adsorption cycle showed higher adsorption capacity and metal ion removal percentages. The drastic reduction in Ni^{2+} adsorption capacity was due to improper regeneration conditions. The regeneration of resins was carried out by eluting the adsorbed metals with 1 M H_2SO_4 and rinsing with distilled water. This regeneration process could not return the resin to its original sodium form. Therefore, a rinse with 1 M NaOH was recommended, followed by another distilled water wash. However, in Co^{2+} only a slight drop in adsorption capacity was observed. The reduction in adsorption capacity and the resin mass loss in the regeneration process caused the reduction in metal ion removal percentages.

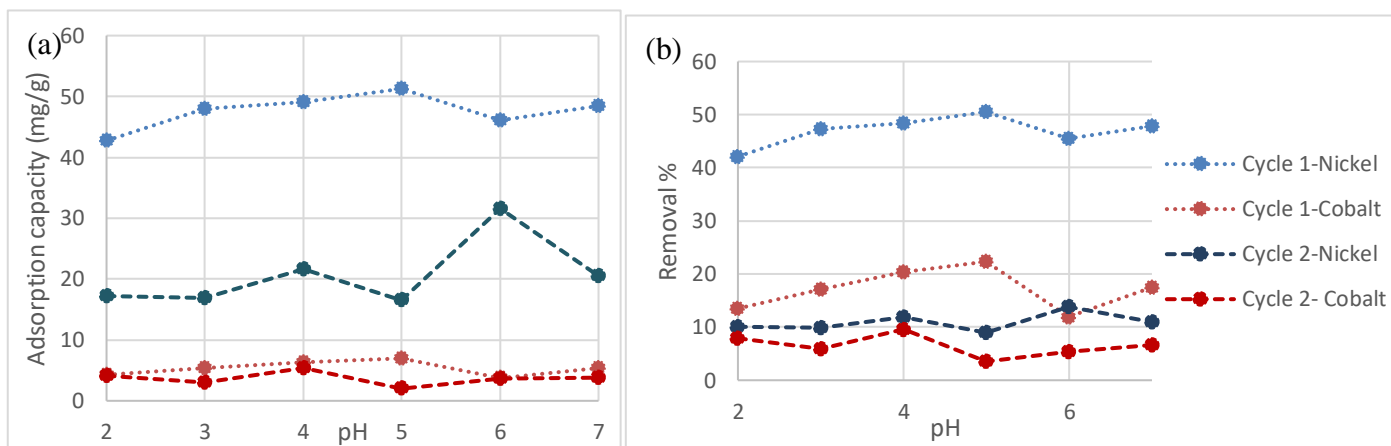


Figure 4.37 (a) adsorption capacity and (b) metal ion removal percentages for adsorption cycles with pH

Figure 4.38 shows the variation of relative selectivity with pH for the two adsorption cycles. Cycle 1 showed higher relative selectivity for Ni^{2+} compared to cycle 2 for all pH values except pH 5. pH 6 showed the highest relative selectivity in both the cycles. Therefore, pH 6 was considered for experiments conducted to determine the effects of other parameters.

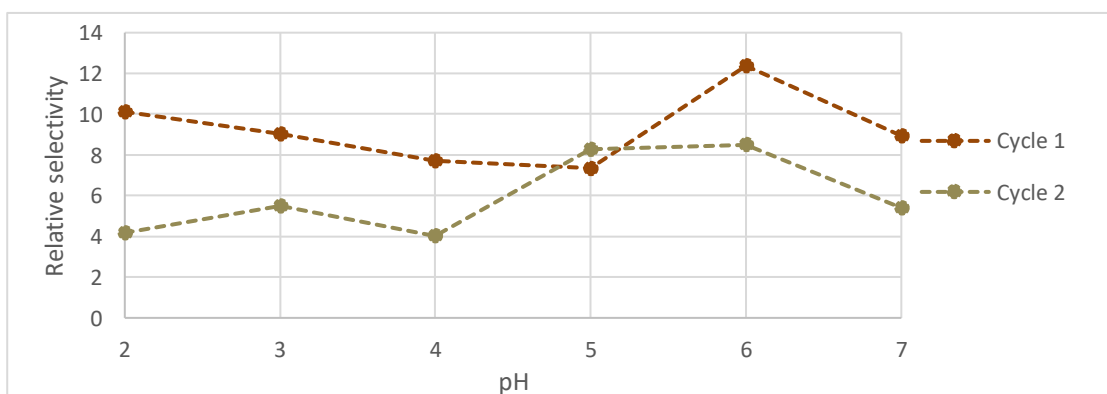


Figure 4.38. Variation of relative selectivity for Ni^{2+} compared to Co^{2+}

4.9.2 Elution of metals

The metal ions adsorbed by resins were eluted using 1 M H_2SO_4 for 2h. The concentration of eluted metal ion solution and the recovery percentages from adsorbed metal content were shown in Figure 4.39. The metal recovery percentages were above 65 % for all pH values considered. At pH 6, 68.7 % and 79.6 % of Ni^{2+} and Co^{2+} were recovered. It is expected that this recovery percentage could be enhanced by increasing the eluting acid volume and elution time.

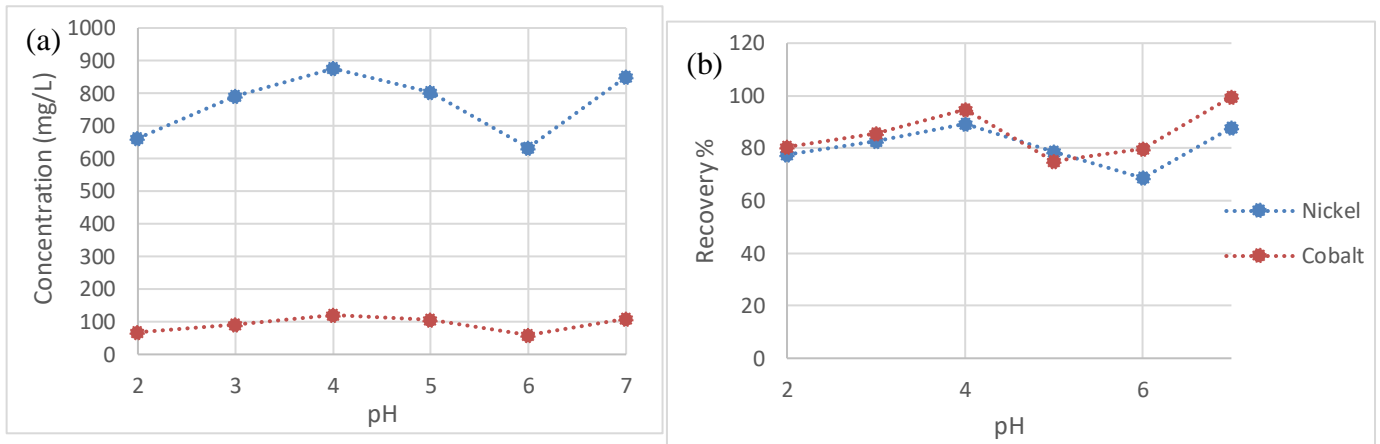


Figure 4.39. Variation of (a) eluted concentration (b) elution recovery efficiency for samples adsorbed at different pH values

4.9.3 Adsorption kinetics

Figure 4.40 (a) and 4.40 (b) show the variation of concentration and adsorption capacity of Ni^{2+} with time. The pH of Ni^{2+} and Co^{2+} mixed solution was adjusted to 6, as discussed previously. The equilibrium conditions were achieved within 1 h.

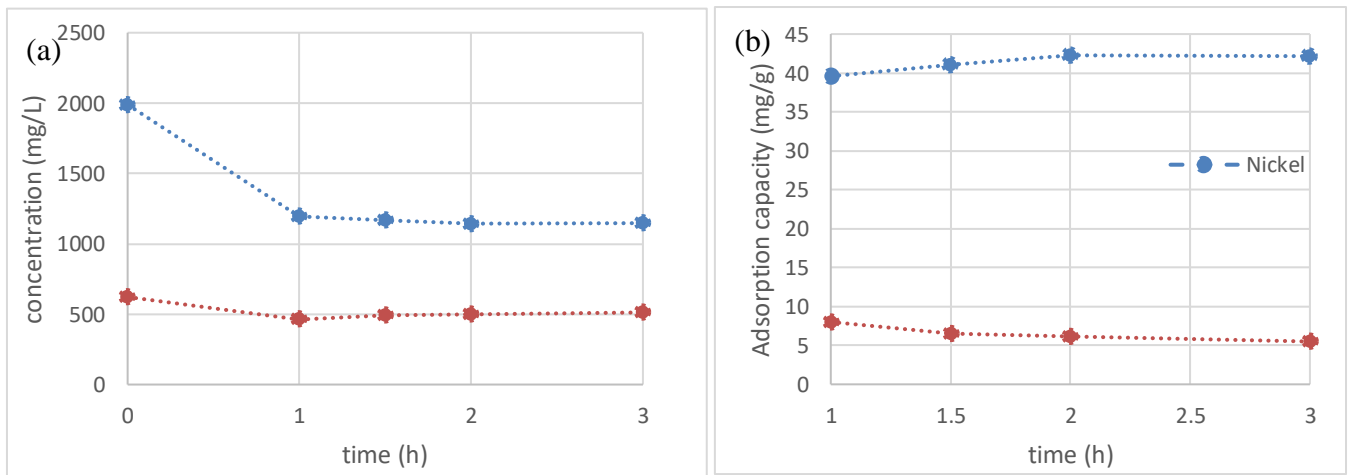


Figure 4.40. Variation of (a) metal concentration and (b) adsorption capacity of metals with time

Figures 4.41 and 4.42 show the plots for pseudo first order and pseudo second order kinetic models for Ni^{2+} and Co^{2+} mixed solution. The model equations 6 and 7 were used in plotting the data, and the kinetic parameters were tabulated in table 4.13. The pseudo second order kinetics showed a better correlation with the data points in both Ni^{2+} and Co^{2+} compared to pseudo first order kinetics.

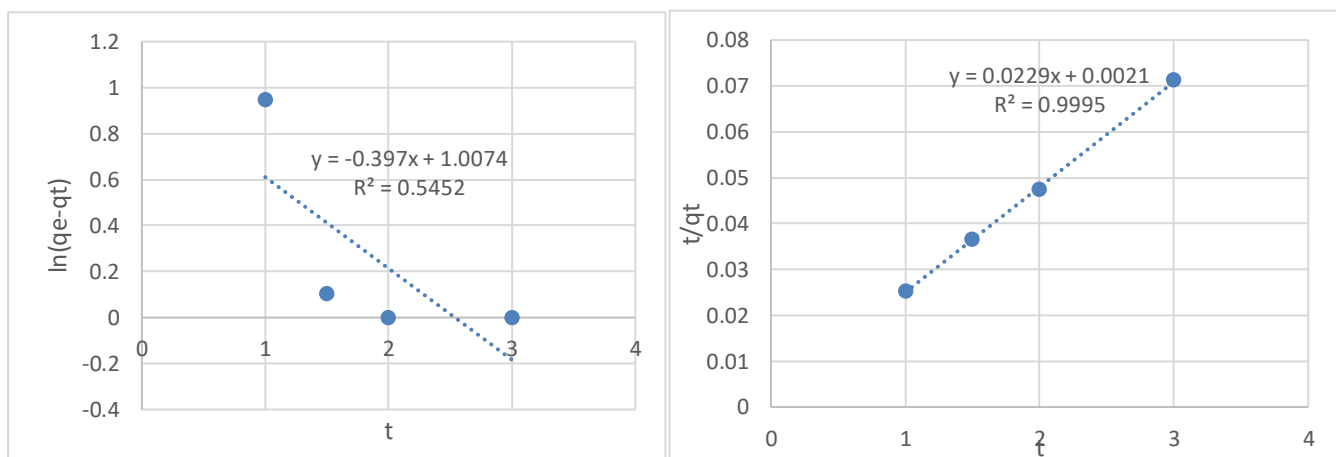


Figure 4.41. (a) Pseudo first order and (b) pseudo second order kinetic models for Ni^{2+}

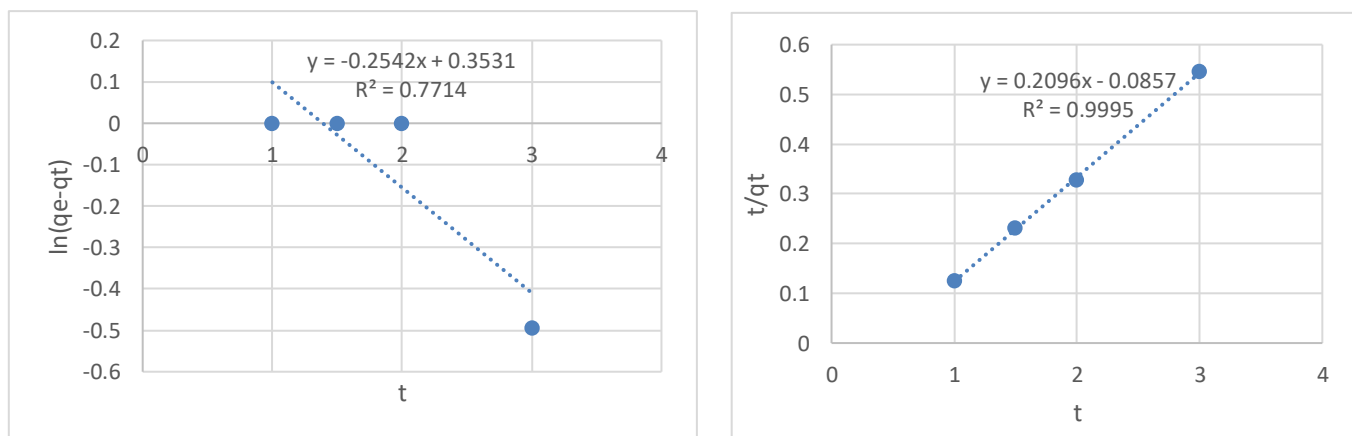


Figure 4.42. (a) Pseudo first order and (b) pseudo second order kinetic models for Co^{2+}

According to table 4.14, when considering better fitted pseudo second order kinetics, the second order rate constant and equilibrium adsorption capacity were higher in Ni^{2+} .

Table 4.14. Calculated parameters from adsorption kinetics models

Metals	Pseudo first order			Pseudo second order		
	K_1 (h^{-1})	q_e ($mg\ g^{-1}$)	R^2	K_2 ($g\ mg^{-1}\ h^{-1}$)	q_e ($mg\ g^{-1}$)	R^2
Ni^{2+}	0.397	2.74	0.5452	0.2497	43.67	0.9995
Co^{2+}	0.2542	1.42	0.7714	-0.0051	4.77	0.9995

4.9.4 Effect of variation of Liquid-Solid ratio

Figure 4.43 (a) and 4.43(b) show the removal percentage and adsorption capacity of Ni^{2+} and Co^{2+} in the mixed solution. The removal percentage of both metal ions was nearly 100 % for a liquid-solid ratio of 10 mL/g and then decreased gradually with the increase in liquid-solid ratio. The adsorption capacities reached a steady value when the liquid-solid ratio was increased.

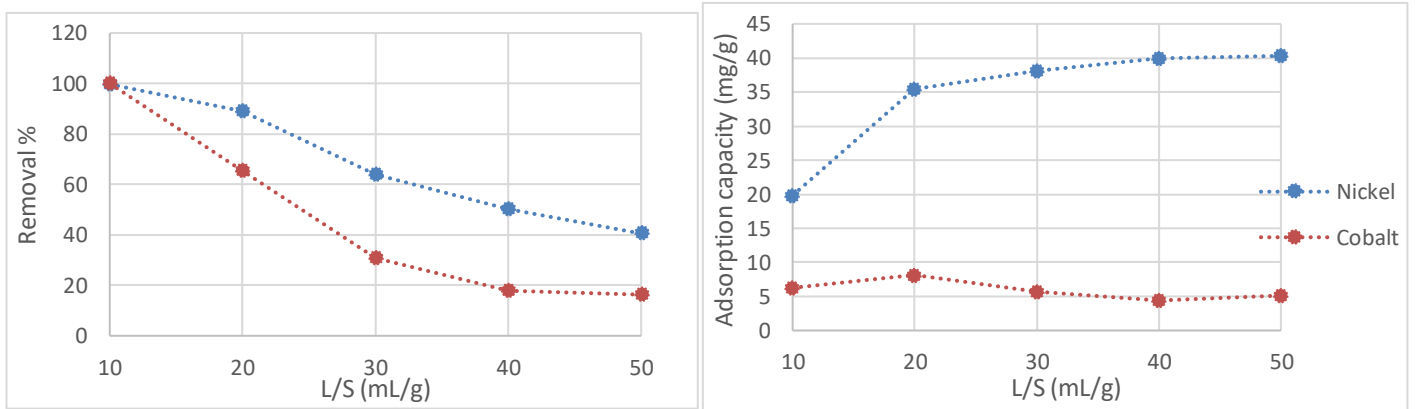


Figure 4.43 (a). Removal percentage and (b) adsorption capacity of Ni^{2+} and Co^{2+} in the mixed solution

Figure 4.44 shows the variation of relative selectivity of Ni^{2+} with liquid-solid ratio. The highest liquid-solid ratio was obtained at 40 mL/g.

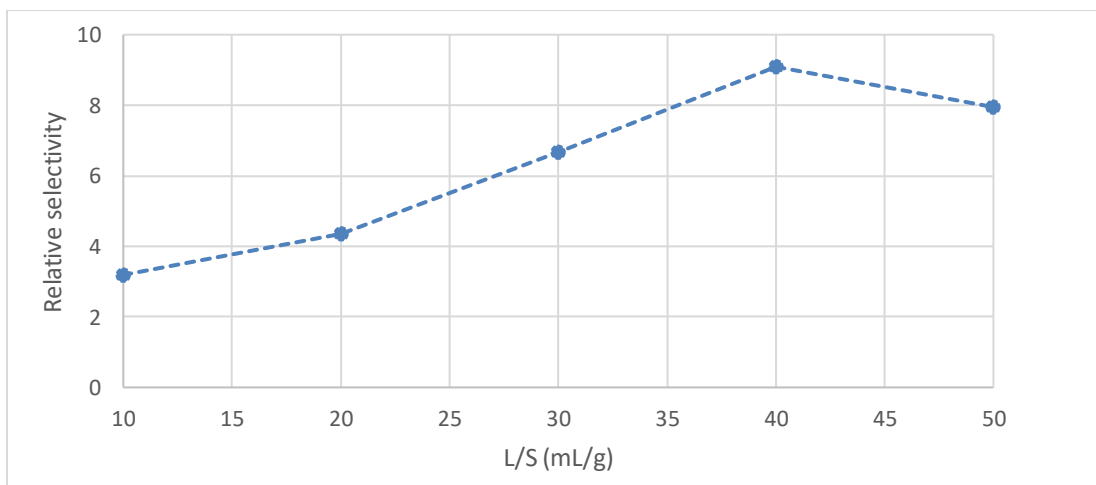


Figure 4.44. Variation of relative selectivity for Ni^{2+} compared to Co^{2+} with liquid-solid ratio

Therefore, higher metal removal was shown at lower liquid-solid ratios while the relative selectivity of Ni^{2+} was enhanced at higher liquid-solid ratios.

4.10 Ion-exchange experiments for resin in Ni²⁺, Co²⁺, Mn²⁺ and Li⁺ simulated mixed solution to determine the liquid-solid ratio.

Batch experiments were conducted in Ni²⁺, Co²⁺, Mn²⁺ and Li⁺ mixed solution to determine the effect of the liquid-solid ratio. The optimum pH values and temperatures determined in previous experiments were used. The relative selectivity of Ni²⁺ with respect to Co²⁺ was reported and discussed to determine the possibility of separating the two metal ions.

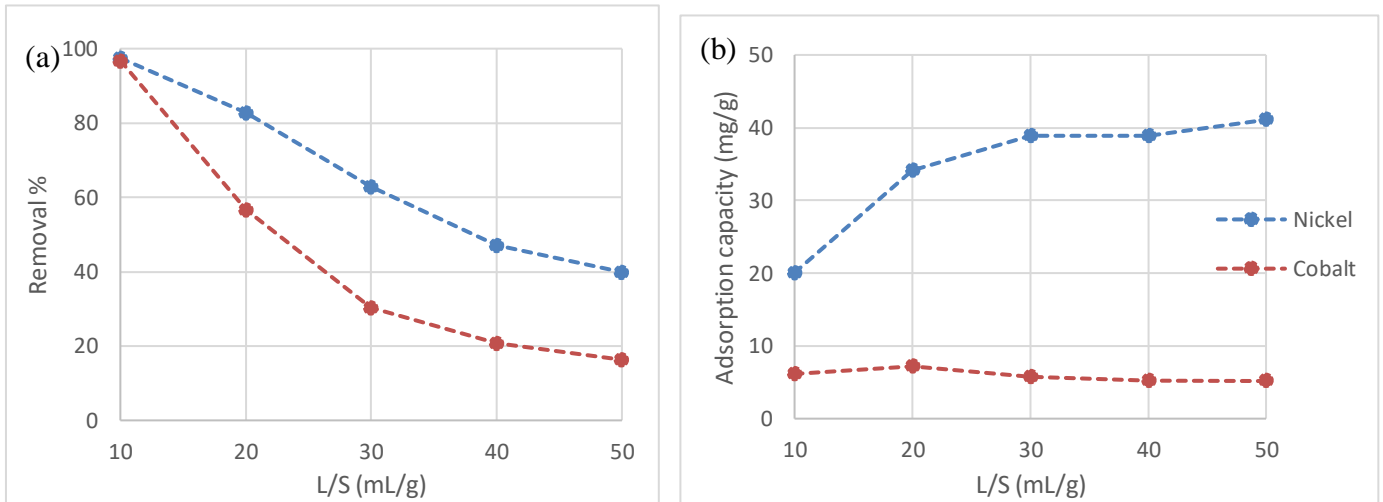


Figure 4.45 (a) metal ion removal percentages and (b) adsorption capacity with solid-liquid ratio

The adsorption capacities and removal percentages were similar in values with a slight decrease compared to the Ni²⁺ and Co²⁺ two-component system (section 4.9.4) indicating that the effect of Mn²⁺ and Li⁺ in the solution was very low. However, the maximum relative selectivity as shown in figure 4.46 at the liquid-solid ratio of 40 mL g⁻¹ has decreased in the presence of Mn²⁺ and Li⁺ in the system due to a certain amount of Mn²⁺ and Li⁺ ions getting exchanged, reducing the sites for Ni²⁺.

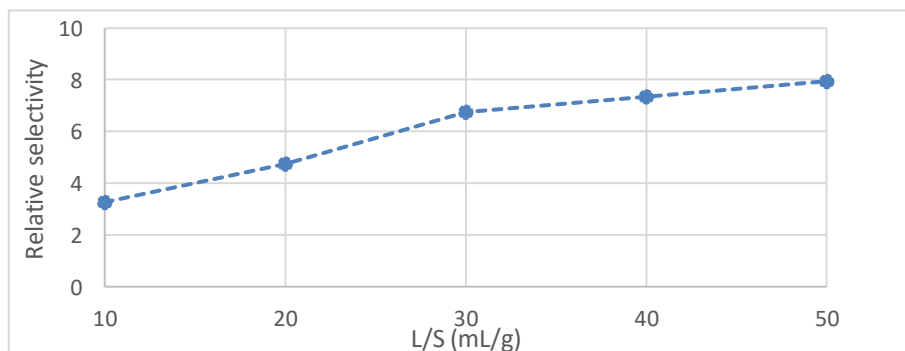


Figure 4.46. Variation of relative selectivity for Ni²⁺ compared to Co²⁺

4.11 Determining the potential of reusing the resin in adsorption

The potential of recyclability of resins in adsorption was investigated for the optimum conditions determined in previous experiments. Samples A and B were selected with initial liquid-solid ratios of 30 mL g⁻¹ and 40 mL g⁻¹. As shown in Table 4.15, the mass of resin used for cycles 2 and 3 decreased due to resin mass loss in the regeneration process. However, the same volume of simulated metal solution was added at all 3 cycles.

Table 4.15. Resin masses used for adsorption cycles.

Sample	Simulated metal solution volume (mL)	Resin mass cycle -1 (g)	Resin mass cycle -2 (g)	Resin mass cycle -3 (g)
sample A	15	0.5	0.2043	0.155
sample B	20	0.5	0.206	0.16

Figures 4.47 and 4.48 show the adsorption capacity variation and removal % of Ni²⁺ and Co²⁺ in the 3 cycles of adsorption. The adsorption capacity of Ni²⁺ and Co²⁺ has an increasing trend when the number of adsorption cycles. In the regeneration process, the acid elution was followed by a base treatment step to convert the resins to sodium form eliminating the effect in the previous resin regeneration experiment. The higher adsorption capacity was due to more open exchange sites in the resin formed due to the damages caused to resin's bead form when stirring in the initial cycles. However, the Ni²⁺ and Co²⁺ removal percentages showed decreasing trend due to the lower amount of resin regenerated with the increase in cycle number. But the removal percentage drop was controlled by the increase in adsorption capacity.

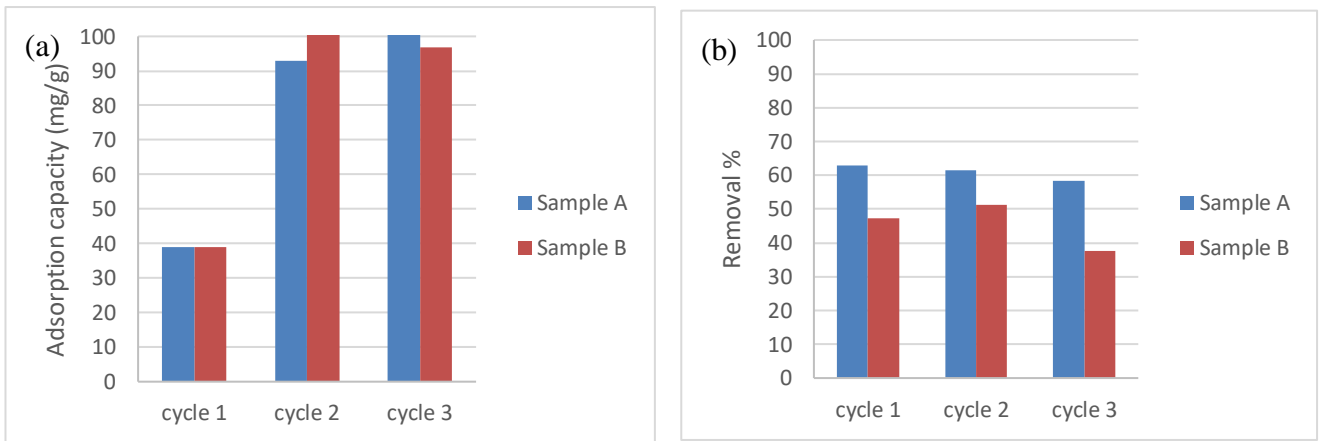


Figure 4.47. (a) adsorption capacity and (b) metal ion removal percentages for Ni^{2+} adsorption cycles for samples with different solid-liquid ratios

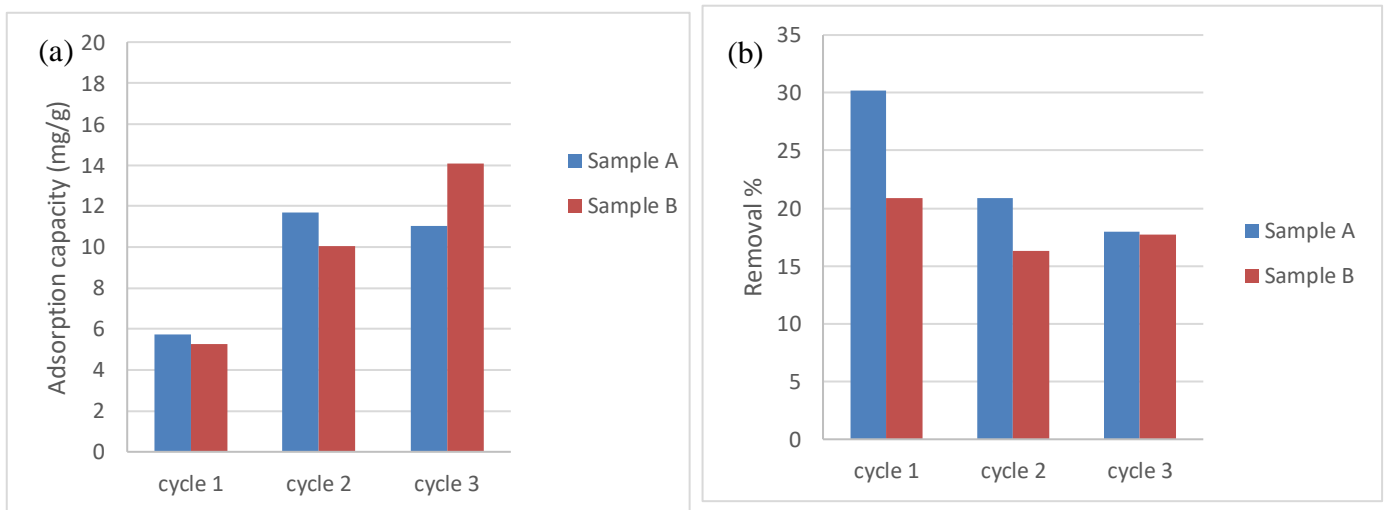


Figure 4.48(a) adsorption capacity and (b) metal ion removal percentages for Co^{2+} adsorption cycles for samples with different solid-liquid ratios

Figure 4.49 shows the relative selectivity of Ni^{2+} with respect to Co^{2+} in samples A and B mentioned above. The relative selectivity of sample A showed an increasing trend. The sample B showed the highest relative selectivity in cycle 2 as cycle 3 did not result in a higher adsorption capacity according to the trend, due to incomplete regeneration of the resin.

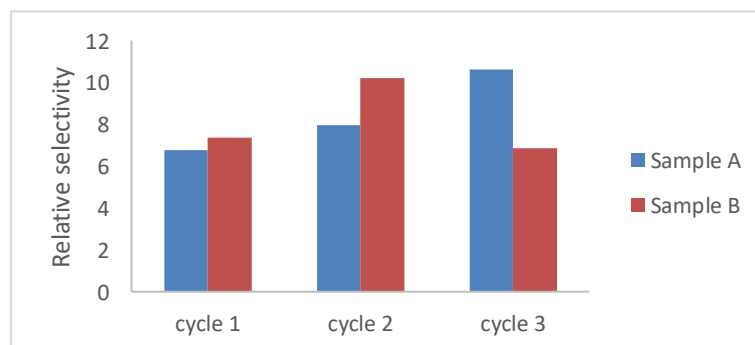


Figure 4.49. Variation of relative selectivity for Ni^{2+} compared to Co^{2+} for samples with different solid-liquid ratios

4.12 Resin column breakthrough experiment

Figure 4.50 shows the breakthrough curves for Ni^{2+} and Co^{2+} in the resin column when Ni^{2+} , Co^{2+} , Mn^{2+} and Li^{+} mixed simulated solution was used. The curves were made by 4th order polynomial trendline to the data sets obtained by the experiment. The removal efficiencies of Ni^{2+} and Co^{2+} were over 99 % until 60 min of flow time. The relatively shallow breakthrough curve of Ni^{2+} indicated the slower adsorption kinetics of the Ni^{2+} in the column.

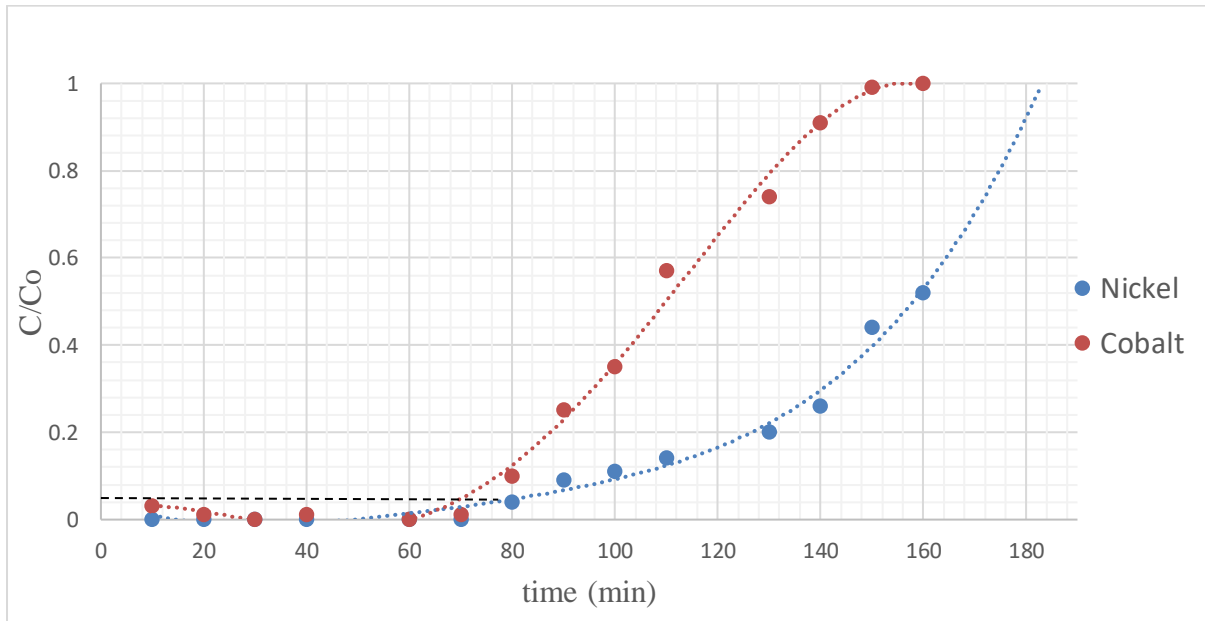


Figure 4.50. Resin breakthrough curve for mixed simulated solution of Ni^{2+} , Co^{2+} , Mn^{2+} and Li^{+}

The breakthrough time was considered as the time at which C/C_0 reached 0.05 (Marzbali & Esmaili, 2017). Hence, the breakthrough time was 78 min and 70 min for Ni^{2+} and Co^{2+} , respectively. The time for bed saturation by Ni^{2+} and Co^{2+} were 180 min and 150 min, respectively.

According to table 4.16, the bed length was used mostly by Co^{2+} . Therefore, overall bed length usage will be decided on the Co^{2+} breakthrough curve, which is 3.02 cm (Appendix 7).

Table 4.16. Summary of calculated bed lengths for breakthrough curves.

Parameter	Ni^{2+} breakthrough curve	Co^{2+} breakthrough curve
Fraction of unused bed	0.4843	0.3963
Length of unused bed	2.42 cm	1.98 cm
Length of used bed	2.58 cm	3.02 cm

4.13 Characterization of regenerated resins

The regenerated resins were characterized using N₂ sorption and ATR-IR to compare with as received resins.

Figure 4.51 shows the nitrogen adsorption (filled marker) and desorption isotherms (non-filled marker) for resin in as received form and regenerated sample. The curves were IUPAC type II isotherms, where it formed a monolayer and then changed into a multi-layer.

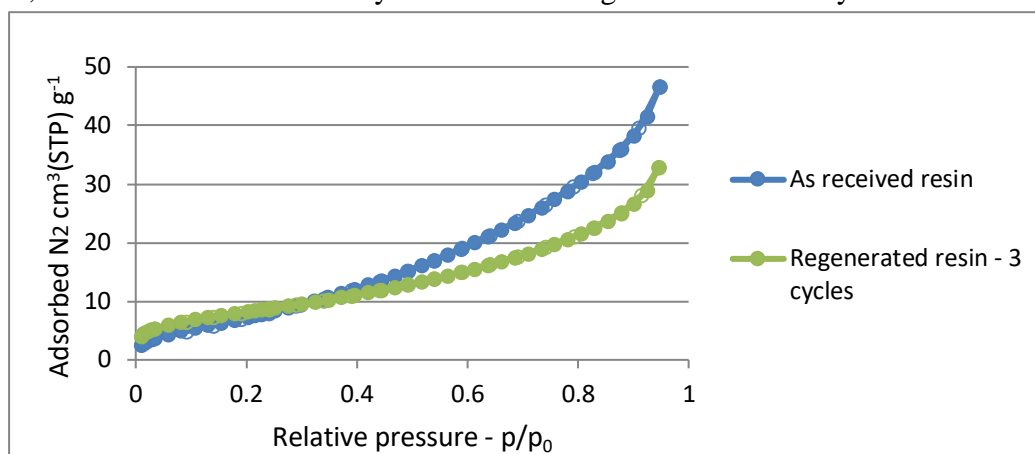


Figure 4.51. Nitrogen sorption isotherms for resins as received and regenerated resins

The BET surface area of regenerated resin was very close to the as-received form, as shown in Table 4.17. However, there was a decrease in total pore volume in regenerated resins due to the presence of adsorbed metals in small quantities and due to the deformation of the beads.

Table 4.17. Comparison of calculated properties from BET curve equation for regenerated resins

Adsorbent	BET surface area (m ² /g)	Total pore volume (cm ³ /g) at 0.94 P/P _o	Monolayer pore volume (V _m) (cm ³ (STP)/g)	Correlation coefficient
Amberlite IRC 748 (as received)	29	0.064	7	0.9977
Amberlite IRC748 (regenerated after 3 cycles)	30	0.045	7	1.0000

Figure 4.52 shows the ATR-IR spectra for as received resin and regenerated resin to analyze the effect of regeneration on resin functionality. According to the spectra, the intensities of regenerated resin have reduced compared to the as received resin, indicating a loss of functional groups after 3 cycles of adsorption.

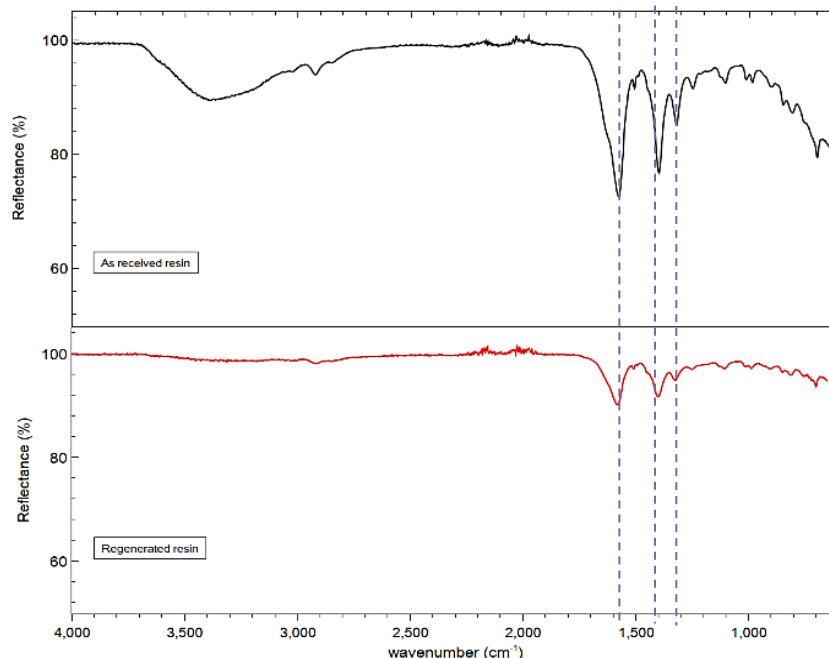


Figure 4.52. ATR-IR spectra for as received and regenerated resins

4.14 Batch adsorption experiments for MOF-808 in single metal solutions.

Batch experiments were conducted in Ni^{2+} and Co^{2+} single metal solutions to determine the effect of pH and liquid-solid ratio. The relative selectivity between two metal ions were not discussed in this section because the metal ions were tested in single-component systems.

4.14.1 Effect of variation of pH

Figures 4.53 (a) and 4.53 (b) show the adsorption capacity of Ni^{2+} and Co^{2+} at pH values 2, 4 and 6 for MOF-808-acetate and its modified MOFs. MOF-808-EDTA showed a significantly higher adsorption capacity than the other MOFs for Ni^{2+} and Co^{2+} . The EDTA group in MOF-808-EDTA provides more active sites where the metal ions can bind efficiently. All the other MOFs showed adsorption capacities less than 10 mg g^{-1} . There were no specific active functional groups in these MOFs to provide active sites for the metal ions. However, modifying the MOF with benzoate and dihydroxybenzoate was expected to enhance the adsorption capacity by changing the pore sizes. But the adsorption capacity decreased to a negligible value to the bulky phenyl groups. At pH 6 the MOFs except MOF-808-EDTA showed nearly zero adsorption capacity for Co^{2+} . In addition, MOF-808-benzoate and MOF-808-DHBA showed nearly zero adsorption capacity for Ni^{2+} (Appendix 8).

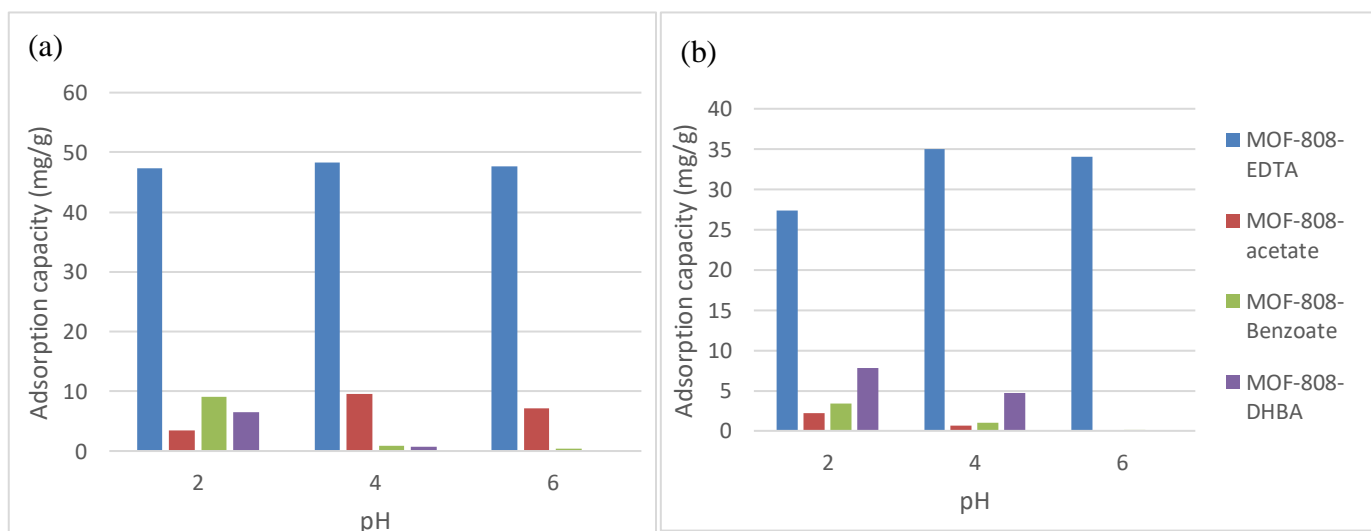


Figure 4.53. Variation of adsorption capacity with pH for (a) Nickel and (b) cobalt ions with MOF-808-types

Figures 4.54 (a) and 4.54 (b) show the metal removal percentages of Ni^{2+} and Co^{2+} respectively at pH values 2, 4 and 6 for MOF-808 analogues. Due to the lower adsorption capacities, the MOFs except MOF-808-EDTA showed metal ion removal percentages less than 10 %.

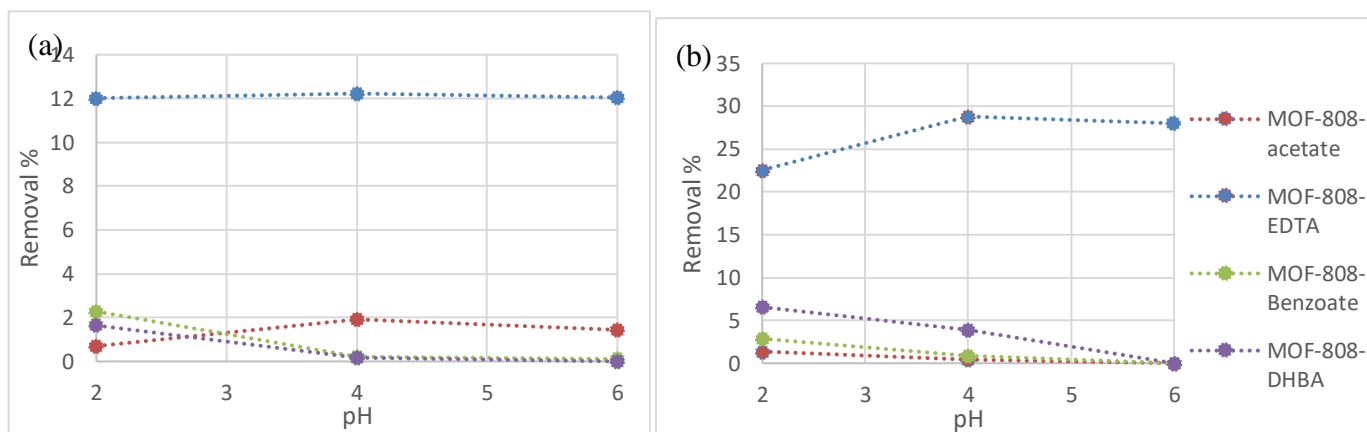


Figure 4.54. Variation of removal percentages with pH for (a) Nickel and (b) cobalt ions with MOF-808-types

Therefore, MOF-808-EDTA was selected for the next experiments at pH 6. However, a significant adsorption capacity and removal percentage was observed for MOF-808-acetate for Ni²⁺ compared to Co²⁺ at pH 6. Hence, MOF-808-acetate was also considered in the next steps with the expectation of selectively adsorbing Ni²⁺ compared to Co²⁺.

4.15 Batch adsorption experiments for MOF-808 in Ni²⁺ and Co²⁺ mixed simulated solution

Batch experiments were carried out in Ni²⁺ and Co²⁺ mixed solution to determine the effect liquid-solid ratio. The relative selectivity of Ni²⁺ with respect to Co²⁺ was reported and discussed here to determine the degree of selectivity.

4.15.1 Liquid-Solid ratio variation for MOF-808-acetate

Figure 4.55 (a) and 4.55 (b) show removal percentage and adsorption capacity of Ni²⁺ and Co²⁺ in mixed solution at pH 6. The removal percentage of both metal ions were less than 5 %, and adsorption capacities were less than 10 mg g⁻¹ for the considered liquid-solid ratios. The significantly higher adsorption capacities for Ni²⁺ over Co²⁺ observed in single metal systems were not observed in Ni²⁺ and Co²⁺ mixed solution. The metal removal percentages did not show an increasing trend, and the adsorption capacities decreased when the liquid-solid ratio was lowered. These observations conclude that the low adsorption capacity shown by MOF-808-acetate is possibly due to the defects in the MOF, which provides random sites where the metal ions can get adsorbed.

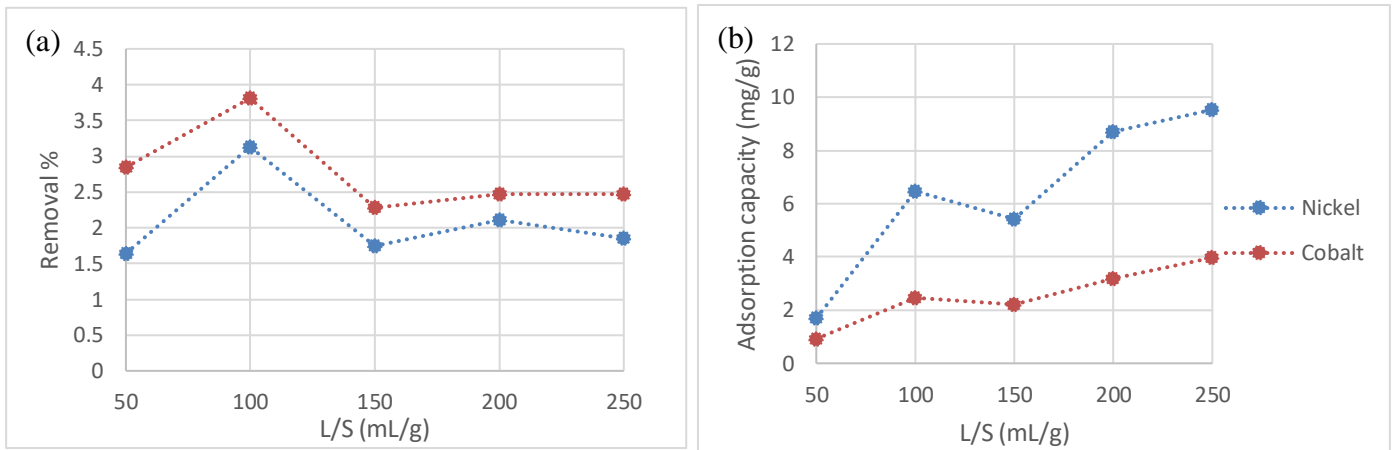


Figure 4.55. Variation of metal removal percentage and (b) adsorption capacity with solid-liquid ratio for MOF-808-acetate

Figure 4.56 shows the variation of relative selectivity of Ni^{2+} with liquid-solid ratio. The relative selectivities showed values around 2.5 for the considered liquid-solid ratios.

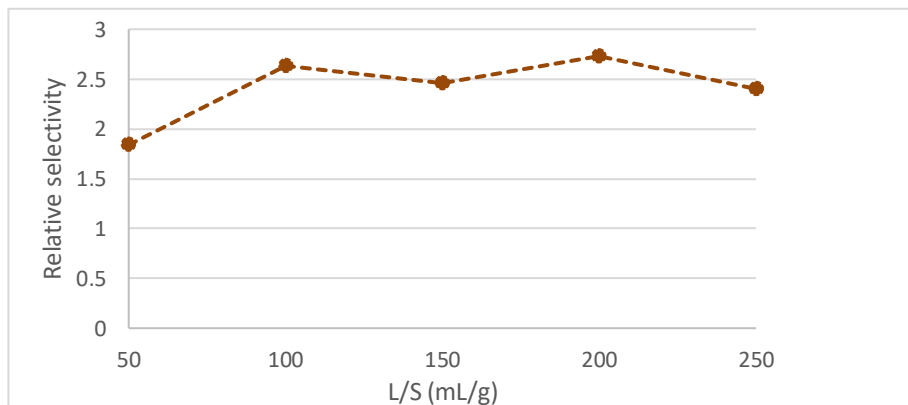


Figure 4.56. Variation of relative selectivity for Ni^{2+} compared to Co^{2+} with solid-liquid ratio for MOF-808-acetate

4.16 Batch adsorption experiments for MOF-808-EDTA in Ni^{2+} , Co^{2+} , Mn^{2+} and Li^+ mixed simulated solution to determine liquid-solid ratio

Figure 4.57 (a) and 4.57 (b) show removal % and adsorption capacity of Ni^{2+} and Co^{2+} in mixed simulated solution at pH 6. The removal percentage of Co^{2+} was less than 5 %, while Ni^{2+} showed significantly higher values at lower liquid-solid ratios. The adsorption capacities showed stable values around 45 mg g^{-1} for Ni^{2+} and $0.5\text{-}1.3 \text{ mg g}^{-1}$ Co^{2+} in the considered liquid-solid ratios.

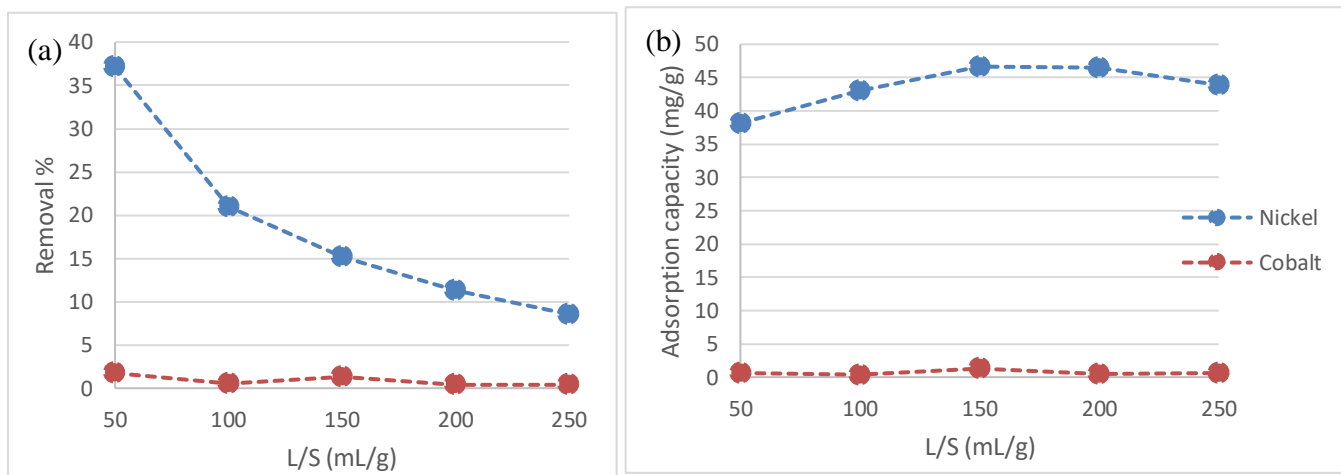


Figure 4.57. Variation of metal removal percentage and (b) adsorption capacity with solid-liquid ratio for MOF-808-EDTA

Figure 4.58 shows the variation of relative selectivity of Ni^{2+} with liquid-solid ratio. The highest liquid-solid ratio of 116.4 mg g^{-1} was obtained at 100 mL g^{-1} . According to the relative selectivity curve, MOF-808-EDTA showed a higher affinity for Ni^{2+} over Co^{2+} . Hence, MOF-808-EDTA is a potential adsorbent in selectively adsorbing Ni^{2+} from Co^{2+} in the simulated solution.

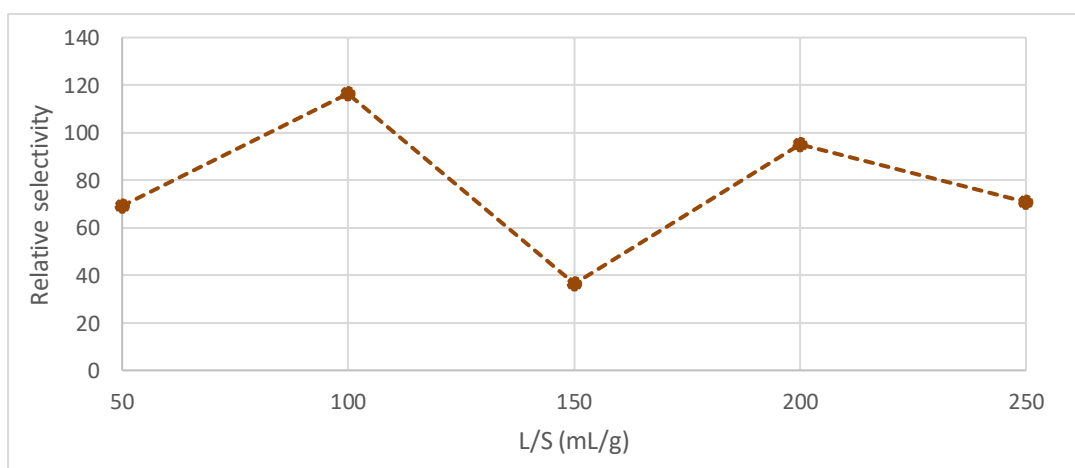


Figure 4.58. Variation of relative selectivity for Ni^{2+} compared to Co^{2+} with solid-liquid ratio for MOF-808-EDTA

4.17 Determining the potential of recycling MOF-808-EDTA

The potential of recyclability of MOF-808-EDTA in adsorption was investigated for the optimum conditions determined in previous experiments. Samples A and B were selected with initial liquid-solid ratios of 100 mL g^{-1} and 150 mL g^{-1} based on relative selectivity and metal

removal percentage. As shown in Table 4.18, the mass of resin used for the second adsorption cycle decreased due to resin mass loss in the regeneration process. However, the same volume of simulated metal solution was added for the second adsorption cycle.

Table 4.18. Mass of MOF-808-EDTA used for adsorption cycles

Sample	Simulated metal solution volume (mL)	MOF mass cycle -1 (g)	MOF mass cycle -2 (g)
sample A	10	0.1	0.0958
sample B	15	0.1	0.0964

Figures 4.59 and 4.60 shows the variation of adsorption capacity and removal % of Ni²⁺ and Co²⁺ in the 2 cycles of adsorption. The adsorption capacity of Ni²⁺ and Co²⁺ has an increasing trend in the second adsorption cycle. The higher adsorption capacity was due to more open exchange sites in the MOF-808-EDTA formed due to the stirring in the initial cycles and regeneration using 2Na-EDTA. Also, the Ni²⁺ and Co²⁺ removal percentages showed an increasing trend due to the less mass loss in MOF-808-EDTA regeneration and increase in adsorption capacity.

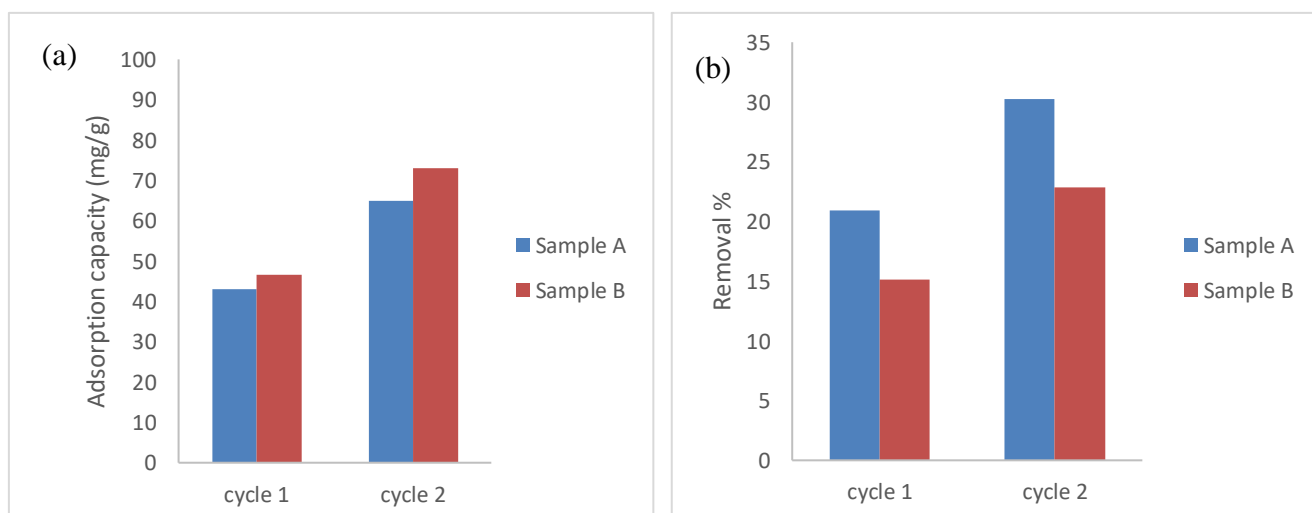


Figure 4.59. (a) adsorption capacity and (b) metal ion removal percentages for Ni²⁺ adsorption cycles for samples with different solid-liquid ratios for MOF-808-EDTA

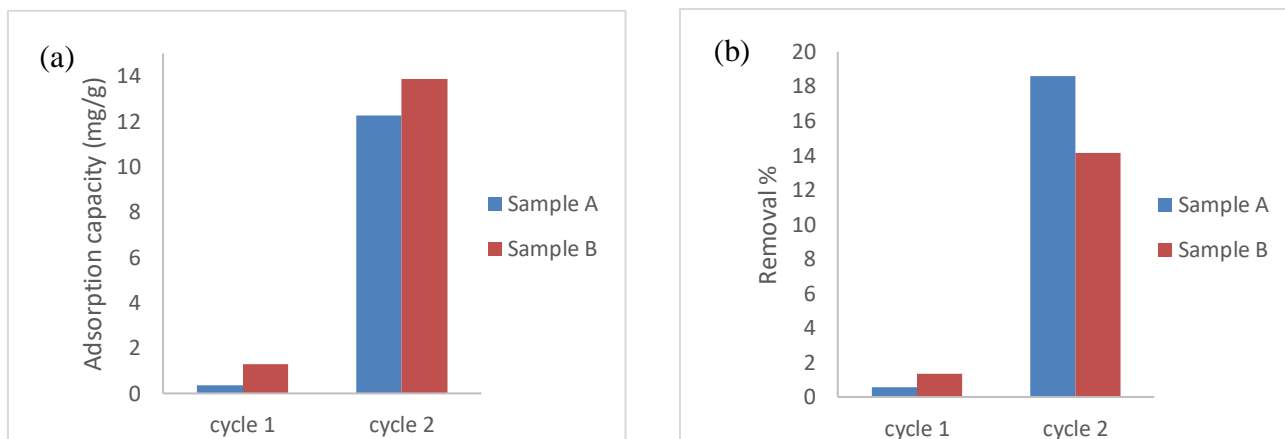


Figure 4.60 (a) adsorption capacity and (b) metal ion removal percentages for Co^{2+} adsorption cycles for samples with different solid-liquid ratios for MOF-808-EDTA

Figure 4.61 shows the relative selectivity of Ni^{2+} with respect to Co^{2+} in samples A and B mentioned above. The relative selectivity of both samples decreased drastically in the second adsorption cycle due to the significant increase in the adsorption capacity of Co^{2+} in the second cycle.

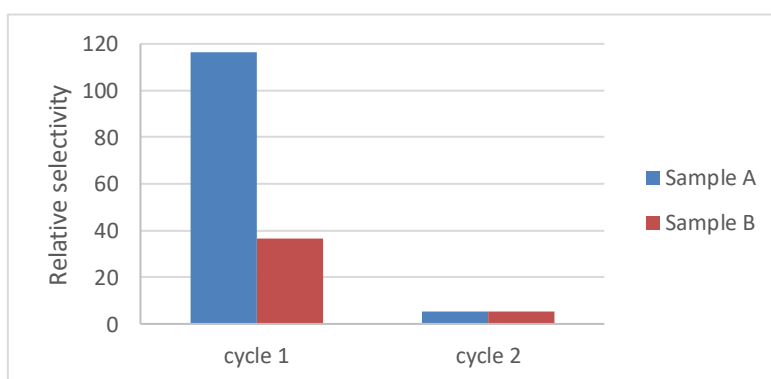


Figure 4.61. Variation of relative selectivity for Ni^{2+} compared to Co^{2+} for samples with different solid-liquid ratios for MOF-808-EDTA

Therefore, MOF-808-EDTA regeneration need to be optimized to maintain the higher selectivity for Ni^{2+} with respect to Co^{2+} .

4.18 Batch adsorption experiments for MOF-808-EDTA in Ni²⁺, Co²⁺, Mn²⁺ and Li⁺ mixed simulated solution to enhance removal % by varying the liquid-solid ratio

Figure 4.62 (a) and 4.62 (b) show ICP-OES determined removal % and adsorption capacity of Ni²⁺, Co²⁺, Mn²⁺ and Li⁺ in mixed simulated solution at pH 6. The adsorption properties of Mn²⁺ and Li⁺ could also be determined due to ICP-OES analysis. The removal percentage of Co²⁺, Mn²⁺ and Li⁺ was less than 5 %, while Ni²⁺ showed relatively higher values at both the liquid-solid ratios. The adsorption capacities showed a slightly higher value for Ni²⁺ at the higher liquid-solid ratio, while all other metals showed nearly zero adsorption capacities. The negative values shown by Mn²⁺ and Li⁺ were due to the slight concentration changes in sample dilutions for ICP-OES (Appendix 9).

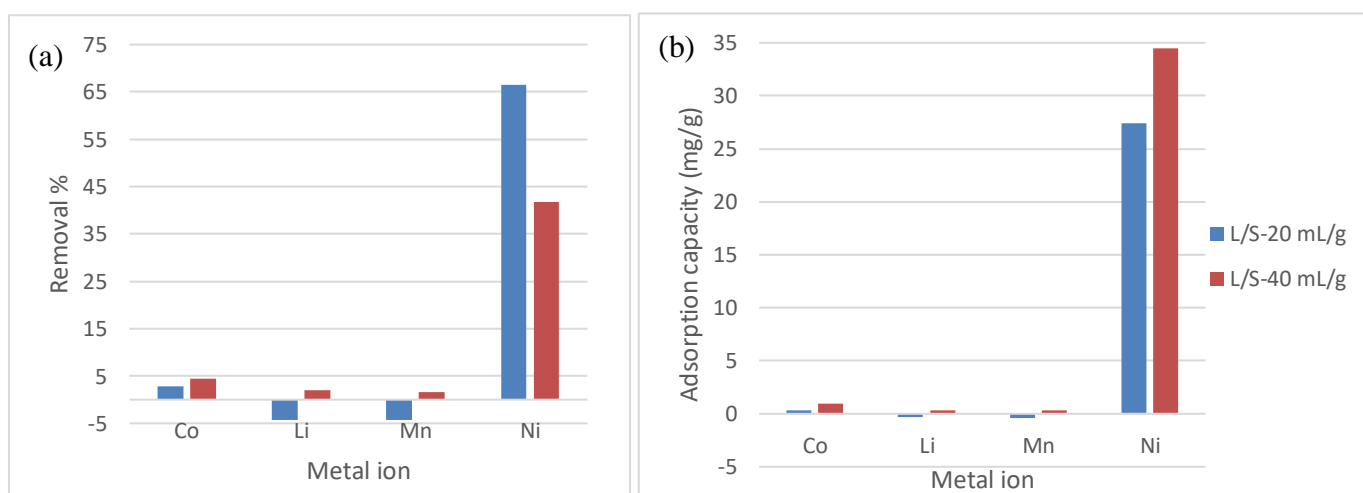


Figure 4.62. (a) Metal ion removal percentages and (b) adsorption capacity with further optimized solid-liquid ratios

According to the relative selectivity shown in Figure 4.63, MOF-808-EDTA has a higher affinity for Ni²⁺ over Co²⁺ at the lower liquid-solid ratio. Hence, MOF-808-EDTA is a potential adsorbent to selectively adsorb Ni²⁺ from Co²⁺ even at lower liquid-solid ratios in the simulated solution, enhancing the Ni²⁺ removal percentage selectively.

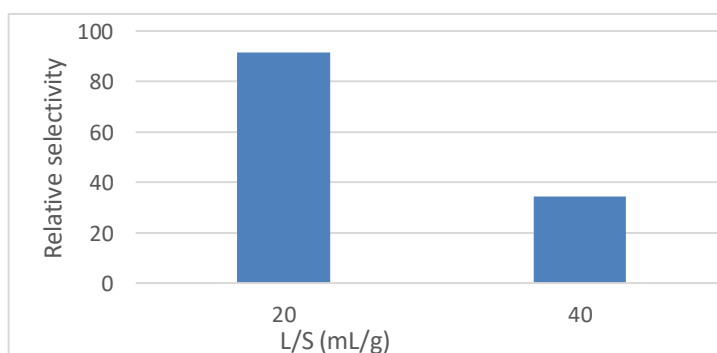


Figure 4.63. Variation of relative selectivity for Ni²⁺ compared to Co²⁺ with further optimized solid-liquid ratios

4.19 Characterization of regenerated MOF-808-EDTA

The regenerated MOF-808-EDTA was characterized using XRD, TGA, BET, EDS, and ATR-IR to compare with as-synthesized MOF-808-EDTA.

Figure 4.64 shows the normalized XRD patterns of as synthesized and regenerated MOF-808-EDTA. When comparing the two spectra, it can be concluded based on observations of related peaks that the regenerated form has peaks at nearly the same 2θ angles confirming the crystallinity remains the same after the regeneration processes.

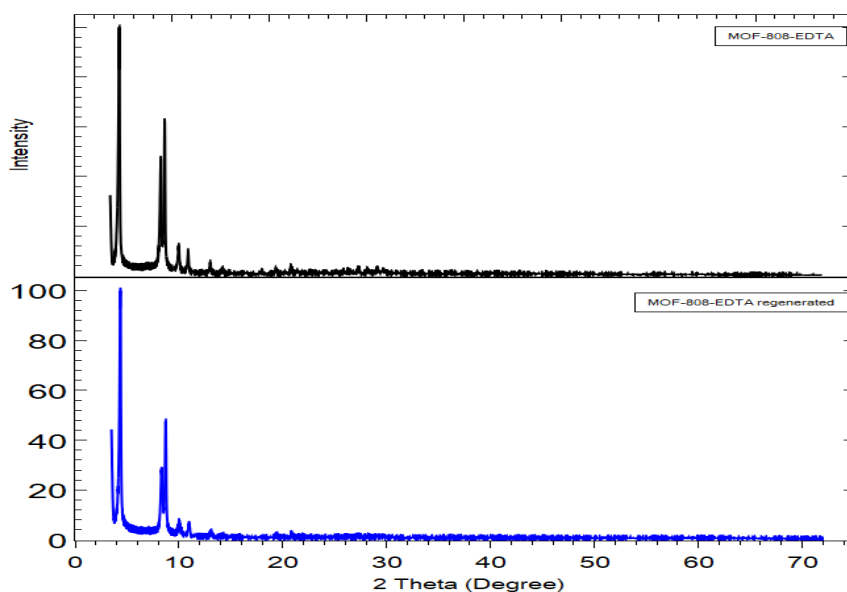


Figure 4.64. X-ray diffraction patterns for as synthesized and regenerated MOF-808-EDTA.

Figure 4.65 displays the TGA curves for the MOF-808-EDTA and its regenerated form. The two curves were almost overlapping except for the slight temperature lag of regenerated MOF-808-EDTA in the upper (region 1) and lower regions (region 4) of the curve. Both the forms maintained thermal stability up to 230 °C, indicating the formation of a regenerated form of similar thermal property.

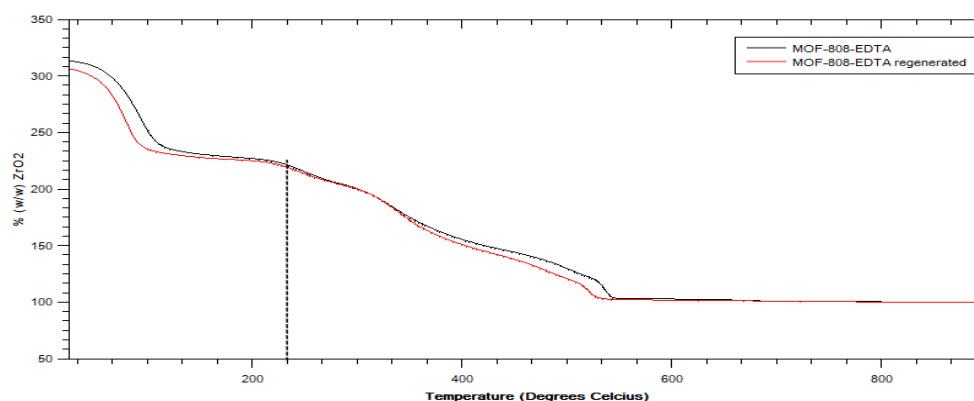


Figure 4.65. TGA for as synthesized and regenerated MOF-808-EDTA

Figure 4.66 shows the ATR-IR spectra of MOF-808-EDTA and when it was regenerated after one cycle of adsorption using 2 Na-EDTA. The MOF-808-EDTA regenerated IR spectra clearly showed intensified peaks with low reflectance % at 1600 cm^{-1} and 1400 cm^{-1} , which corresponds to vibrations due to C=O bonds and wavenumber 1580 cm^{-1} corresponding to C-N bond vibrations. The concentration of 2Na-EDTA used for the regeneration was twice the concentration used for ligand exchange to form MOF-808-EDTA initially. The higher concentration led to the exchange of more EDTA groups with the MOF-808 cluster, showing intensified peaks for the characteristic bond vibrations due to the presence of EDTA.

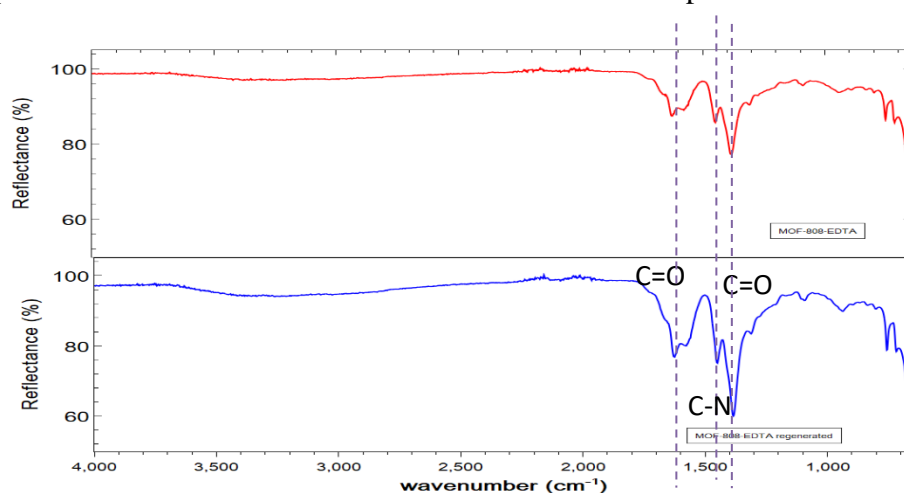


Figure 4.66. ATR-IR spectra for as synthesized (red) and regenerated MOF-808-EDTA (blue)

The intensified peaks confirm the hypothesis of having more EDTA groups in the MOF-808 cluster which enhanced the adsorption capacity in the second cycle, as discussed in the MOF-808-EDTA regeneration experiment.

Figure 4.67 shows the nitrogen adsorption (filled marker) and desorption isotherms (non filled marker) for MOF-808-EDTA in as synthesized, with metals adsorbed and regenerated forms. The curves followed IUPAC type I isotherm.

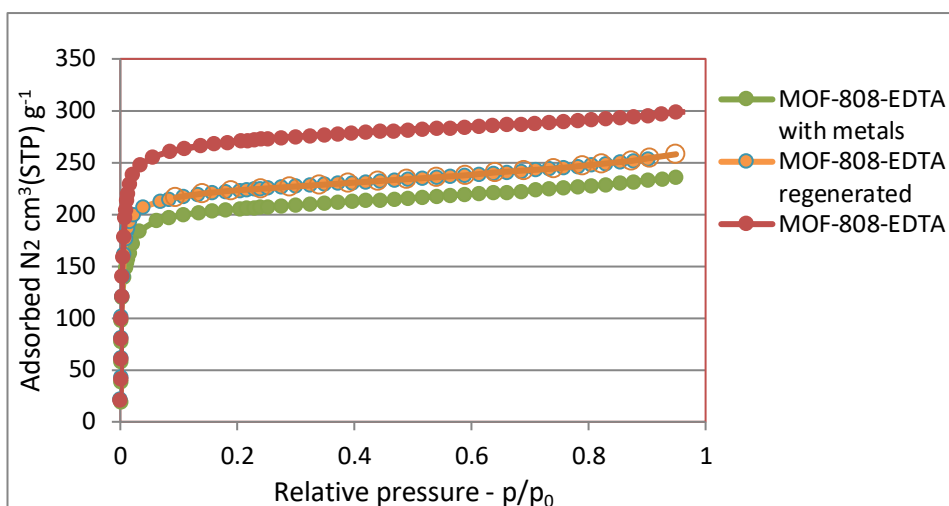


Figure 4.67. Nitrogen sorption isotherms for as synthesized, metal adsorbed and regenerated MOF-808-EDTA

The BET surface area of MOF-808-EDTA with metals has decreased with respect to the as synthesized form, but with the regeneration, the BET surface area increased, as shown in Table 4.19. However, there was a decrease in BET surface area and total pore volume in regenerated MOF-808-EDTA. The difference of 200 $\text{m}^2 \text{g}^{-1}$ of BET surface area can be partially affected by the lower regenerated sample mass used for BET analysis which was approximately half of the recommended sample weight for TriStar II Plus instrument.

Table 4.19. Comparison of calculated properties from BET curve equation for regenerated MOF-808-EDTA

Adsorbent	Sample mass used (g)	BET surface area ($\text{m}^2 \text{g}^{-1}$)	Total pore volume ($\text{cm}^3 \text{g}^{-1}$) at 0.94 P/P _o	Monolayer pore volume (V_m) ($\text{cm}^3(\text{STP}) \text{g}^{-1}$)	Correlation coefficient
MOF-808-EDTA	0.125	1101	0.459	253	0.9995
MOF-808-EDTA with metals	0.069	825	0.363	189	0.9998
MOF-808-EDTA regenerated	0.067	893	0.396	205	1.0000

Figure 4.68 shows the EDS of MOF-808-EDTA with metals adsorbed and in regenerated form. MOF-808-EDTA was kept stirring with Ni^{2+} , Co^{2+} , Mn^{2+} , and Li^+ mixed simulated solution for 24 h to adsorb the metals. According to the elemental analysis, only nickel was detected, matching the adsorption results obtained because Ni^{2+} ions were selectively adsorbed over Co^{2+} ions. The EDS elemental analysis for the regenerated sample indicated the presence of trace amounts of nickel. The decrease in the spectral peaks for nickel to very low levels and the decrease in the elemental composition of nickel from 8.48 % to 0.87 % proves the efficacy of the regeneration process.

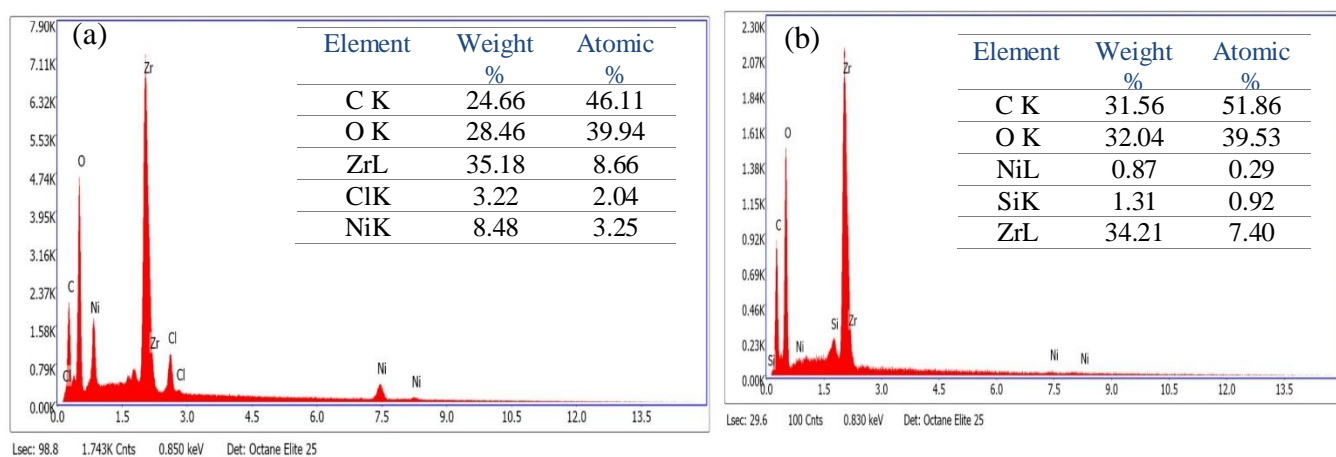


Figure 4.68. EDS analysis for (a) metal adsorbed and (b) regenerated MOF-808-EDTA

4.20 Adsorption experiments in citric acid leachate under optimum conditions

The optimum conditions resulted from experiments conducted in simulated solutions were applied in this experiment with citric acid black mass leachate. The experiment was conducted at a temperature of 20 °C and a solution initial pH of 6. However, the citric acid leachate pH adjustment was critical because 40 mL of citric acid leachate consumed 200 mL of 1 M NaOH, diluting the solution in a 1:6 ratio. Due to the diluted metal ion concentrations, the liquid-solid ratio was maintained at 40 mL g⁻¹ and 200 mL g⁻¹ for resins and MOF-808 types, respectively. All the samples were analyzed in duplicates, and the mean values were recorded in table 4.20 for metal removal percentage and adsorption capacity.

According to the results obtained with resins, all the metal ions except Ni^{2+} and Co^{2+} showed nearly zero adsorption. The relative selectivity of Ni^{2+} with respect to Co^{2+} was 3.6. However, the metal removal percentages and adsorption capacities with Ni^{2+} and Co^{2+} are nearly zero for all the MOF-808 types used.

Table 4.20. Summary of adsorption experiments with citric acid black mass leachate

Sample	Removal (%)							Adsorption capacity (mg/g)						
	Al	Co	Cu	Fe	Li	Mn	Ni	Al	Co	Cu	Fe	Li	Mn	Ni
Resin in citric acid leachate	-4.8	25.5	-	-3.8	-2.1	2.7	37.5	-0.5	2.4	-	-0.1	-0.2	0.3	8.6
MOF-808-EDTA in citric acid leachate	-1.1	-1.1	-	0.4	-1.2	2.8	-1.3	-0.5	-0.5	-	0	-0.5	1.7	-1.5
MOF-808-acetate in citric acid leachate	-0.2	-0.2	-	0.9	0.5	1.8	0.2	-0.1	-0.1	-	0.1	0.2	1.1	0.2
MOF-808-benzoate in citric acid leachate	-1.7	-0.9	-	0.6	-1	1.5	-0.1	-0.8	-0.4	-	0	-0.4	0.9	-0.1

As shown in Table 4.21, the high quantity of NaOH addition can cause interference in adsorbing the leachate metal ions due to very high sodium ion concentration relative to other metal ions.

Table 4.21. Metal composition in pH 6 adjusted citric acid black mass leachate

Metal ion	Concentration in pH 6 adjusted citric acid leachate (mg L ⁻¹)
Sodium	19166
Aluminium	234.5
Cobalt	231.5
Iron	40.95
Lithium	201.5
Manganese	307.5
Nickel	574

Figure 4.69 shows the normalized XRD spectra to determine the chemical stability of MOF-808 analogues in citric acid at pH 6. According to the spectra, MOF-808-EDTA was chemically unstable when compared with as synthesized MOF-808-acetate becoming another reason for the negligible metal uptake in the citric acid black mass leachate.

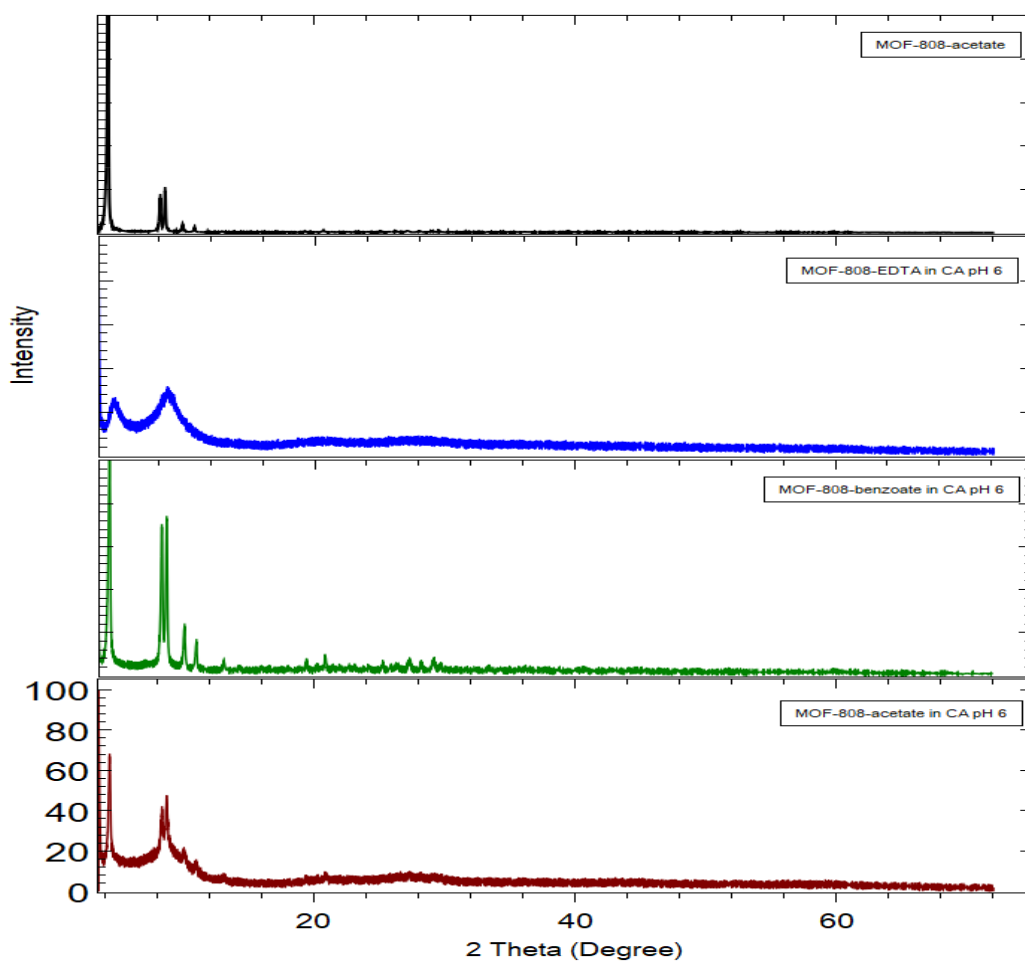


Figure 4.69. X-ray diffraction patterns for MOF-808 types in citric acid black mass leachate adjusted at pH 6

According to figure 4.70, the citric acid leachate adsorbed MOF-808 types showed a similar trend with the temperature variation. Compared to the synthesized MOF-808-acetate, the metal adsorbed MOF-808 samples showed a high percentage of solvent or moisture. The higher temperature region showed two stages of percentage weight reduction which might be due to metals and need to be compared with XRD spectra of MOF-808 after adsorption in simulated aqueous metal solution. The difference in shapes of TGA curves compared to as synthesized MOF-808-acetate sample indicated the occurrence of structural changes in adsorbed MOF-808, leading to instability of the MOFs.

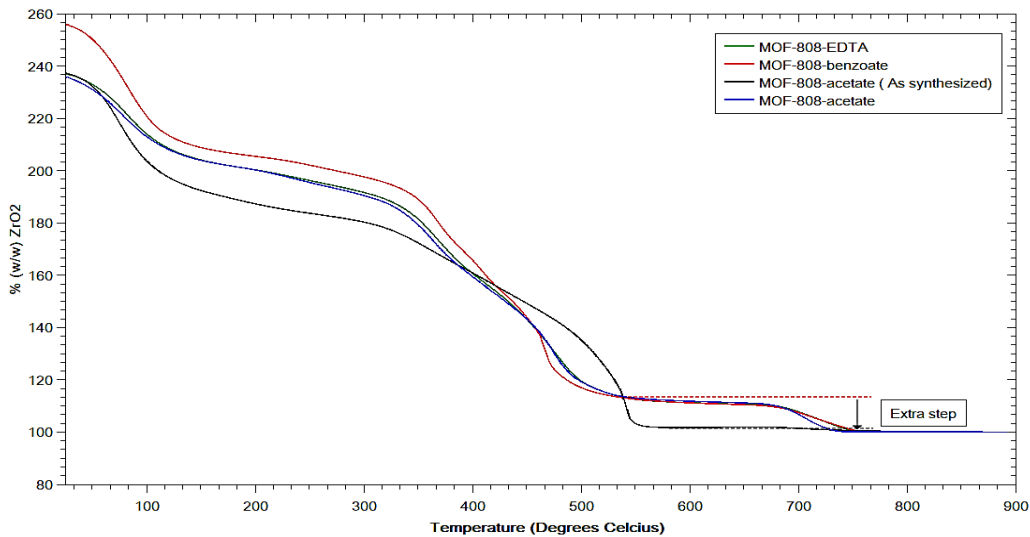


Figure 4.70. TGA for MOF-808 types in citric acid black mass leachate adjusted at pH 6

Therefore, with citric acid leachate, it is recommended to conduct the adsorption experiments without pH adjustment or with pH 2 adjustment as the next step in this study. However, with the time limitation and limited availability of ICP-OES for the analysis, it will be suggested for future works related to this study.

5. ERROR ANALYSIS

This section analyzes the uncertainties and errors with experimental procedures, instruments, and results. In the calculations for percentage error, three sigma (3σ) value with a confidence level of 99.7 % was considered.

5.1 Preparation of UV-visible spectrophotometer calibration curves

The samples were prepared in duplicates for both Ni^{2+} and Co^{2+} for each concentration used in the calibration curve. Most of the metal uptake experiment calculations were based on the calibration curves prepared here. Thus it is important to maintain a higher accuracy of the data. According to the tables 5.1 and 5.2, the percentage error values were less than 3 % which is an acceptable value for the analysis.

Table 0.1 Error analysis for Ni^{2+} calibration standard absorbance values

Concentration (mg L ⁻¹)	Mean Absorbance	Standard deviation of absorbance	Percentage error (%)
500	0.0475	0.0001	0.6
1000	0.0952	0.0001	0.3
2000	0.1879	0.001	1.6
3000	0.2823	0.0006	0.6
4000	0.3799	0.0012	0.9
5000	0.4731	0.0016	1
6000	0.5664	0.0037	2

Table 0.2. Error analysis for Co^{2+} calibration standard absorbance values

Concentration(mg L ⁻¹)	Mean absorbance	Standard deviation of absorbance	Percentage error (%)
250	0.0207	0.0001	1.4
500	0.0408	0	0
1,000	0.082	0.0006	2.2
1,500	0.123	0.0011	2.7
2,000	0.1633	0	0
2,500	0.2047	0.0008	1.2

5.2 Batch adsorption experiments

Resin batch adsorption experiment to determine the effect of liquid-solid(L-S) variation in simulated mixed solution of Ni^{2+} , Co^{2+} , Mn^{2+} and Li^{+} was duplicated. The results obtained were analyzed as shown in Table 5.3. According to the error analysis, the percentage error was less than 5 % for all the samples except the L-S ratio 10 sample. The high percentage error in

the L-S ratio 10 sample is due to the low metal concentrations resulting low absorbance values from the UV-visible spectrophotometer below the calibrated range. Therefore, it is required to have a calibration curve in the lower range to obtain accurate results for the L-S ratio 10 sample. However, the other results were acceptable according to the error analysis.

Table 0.3. Error analysis for resin batch adsorption experiment to determine the effect of liquid-solid (L-S) variation in simulated solution of Ni²⁺, Co²⁺, Mn²⁺ and Li⁺

Sample/ L-S ratio (mL g ⁻¹)	Ni ²⁺			Co ²⁺		
	Mean concentration (mg L ⁻¹)	Standard deviation	Percentage error (%)	Mean concentration (mg L ⁻¹)	Standard deviation	Percentage error (%)
Initial metal solution	2060.69	1.49	0.22	633.66	7.79	3.69
10	52.51	1.49	8.51	20.28	1.73	25.59
20	355.11	4.49	3.79	274.07	4.33	4.74
30	764.05	11.22	4.41	442.24	1.73	1.17
40	1087.81	15.71	4.33	501.56	6.05	3.62
50	1238.06	3.74	0.91	530.3	5.19	2.94

5.3 Comparison of ICP-OES and UV-visible spectroscopy determined adsorption results.

The metal removal percentage and adsorption capacity for Ni²⁺ and Co²⁺ adsorption with MOF-808-EDTA at liquid-solid ratios of 20 mL g⁻¹ and 40 mL g⁻¹ were compared using ICP-OES and UV-visible spectroscopy as shown in Table 5.4. The percentage difference values of the results obtained by the two instruments showed considerable differences due to human and instrumental errors the two techniques were performed. However, both the techniques resulted in similar trends and Ni²⁺ showed lower deviations with the two techniques compared to Co²⁺.

Table 0.4. Comparison of ICP-OES and UV-visible spectroscopy results for Ni²⁺ and Co²⁺ batch adsorption with MOF-808-EDTA at different liquid-solid ratios

Sample	Removal %						Adsorption capacity (mg g ⁻¹)					
	ICP-OES		UV-visible		Percentage difference		ICP-OES		UV-visible		Percentage difference	
	Co	Ni	Co	Ni	Co	Ni	Co	Ni	Co	Ni	Co	Ni
MOF-808-EDTA in synthetic solution -20 mL g ⁻¹	2.8	66.5	3.2	61.9	14.3	6.9	0.3	27.4	0.4	24.81	33.3	9.5
MOF-808-EDTA in synthetic solution -40 mL g ⁻¹	4.4	41.8	4.85	38.46	10.2	8.0	1	34.5	1.22	30.83	22	10.6

5.4 Characterization of black mass and adsorbents

Sample preparation is an important aspect of characterization techniques. Deviation of results were caused due to errors by the analyzer and the instrument.

When preparing the XRD samples, the powdered samples should be levelled using a glass plate, forming a smooth upper layer and a finely distributed solid layer in the case of slurry samples.

It is important to check a blank sample before each measurement when using ATR-IR because slight contamination can result in highly deviated reflectance percentage. Nitrogen sorption (BET) results have a high chance of deviation when lower amounts of adsorbents were measured. Also, it was important to transfer the samples to the bulb area of the sample tube without getting samples stuck in the tube neck region.

6. CONCLUSION

The metal recovery process consists of spent battery waste pretreatment, metal extraction, and metal separation. The black mass obtained for this study was crushed and thermally treated electrode material with a cathode configuration mixture of mainly NMC 622 and NMC 811. The metal extraction was conducted by hydrometallurgy process with citric acid which is an organic acid with less environmental impact and high literature reported leaching efficiency. The metal separation, which is the main focus area of this study, was experimented with MOF-808 types and resin, Amberlite IRC-748. Amberlite IRC-748 in as received (sodium) form showed 3 and 2 times higher adsorption capacities for Ni^{2+} and Co^{2+} respectively when compared to the treated (hydrogen) form for adsorption at pH 6 due to removal of functional groups in acid treatment. The resin was 3.5 times more selective towards Ni^{2+} over Co^{2+} in the citric acid black mass leachate at pH 6 where the highest selectivity for Ni^{2+} was resulted. Over 99 % metal removal percentage was observed at 10 mL g^{-1} liquid to solid ratio. However, higher selectivity for Ni^{2+} was observed at the higher liquid to solid ratios. Therefore, selecting the optimum liquid-solid ratio is highly dependent on the application. The resin adsorption kinetics followed pseudo-second order with a lower sorption rate for Ni^{2+} compared to Co^{2+} . Hence adsorption time was not a useful parameter in enhancing the Ni^{2+} selectivity of resins. Langmuir model fitted the adsorption isotherm data with a higher correlation coefficient compared to Freundlich isotherm. The resin recyclability in metal uptake was consistent over the three sorption cycles tested.

Zr-MOF-808 and its modified groups such as MOF-808-benzoate, MOF-808-DHBA, and MOF-808-EDTA were successfully synthesized and grafted according to the characterization results. In single metal simulated solutions, MOF-808-EDTA showed better metal uptake with adsorption capacities above 40 mg g^{-1} and 25 mg g^{-1} for Ni^{2+} and Co^{2+} respectively, while the other MOF-808 analogues showed adsorption capacities less than 10 mg g^{-1} due to the lack of active functional sites for adsorption. However, higher adsorption capacities and removal percentages were observed for MOF-808-acetate for Ni^{2+} compared to Co^{2+} at pH 6. But with the Ni^{2+} and Co^{2+} mixed simulated solution, MOF-808-acetate showed a lower relative selectivity of Ni^{2+} with respect to Co^{2+} , which was around 3 times. In contrast, Ni^{2+} and Co^{2+} mixed simulated solution with MOF-808-EDTA showed a higher relative selectivity of Ni^{2+} with respect to Co^{2+} in the range of 40-120 times with the variation of liquid-solid ratio with negligible uptake of Mn^{2+} and Li^+ . MOF-808-EDTA was regenerated using 2Na-EDTA, and the characterization results confirmed the successful regeneration of the original form of the

MOF-808-EDTA. However, there was a reduction in relative selectivity of Ni^{2+} with respect to Co^{2+} in the recycling stages.

The citric acid black mass leachate adsorption experiments showed a metal uptake only for the resins with negligible uptakes for MOF-808 when the adsorption conditions from the mixed simulated solutions were used. This is possibly due to the unfavorable conditions affecting adsorption which will be discussed with the possible modifications and suggestions for future experiments under the recommendations.

The process shown in the flow diagram below can be suggested from experiments performed to recover Ni^{2+} and Co^{2+} . A breakthrough column experiment was conducted as an initiative, which resulted in a complete Ni^{2+} , and Co^{2+} removal from the simulated solution in the initial 50 min with a break-through time of 70 min.

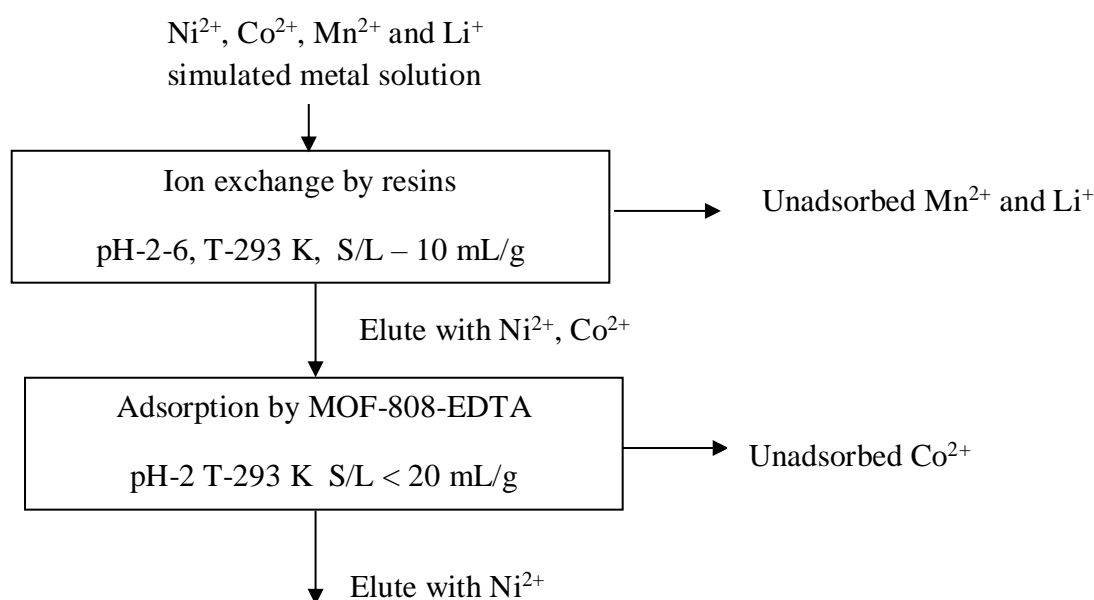


Figure 6.1. Suggested process flow diagram for recovery of Ni^{2+} and Co^{2+} .

Overall, the experimental methods were able to address the thesis objectives satisfactorily, confirming the potential of as received Amberlite IRC 748 in uptaking Ni^{2+} and Co^{2+} and MOF-808-EDTA in selectivity uptaking Ni^{2+} with respect to Co^{2+} .

7. RECOMMENDATIONS

This study was conducted as a preliminary step in the metal recovery process from spent battery waste by determining the black mass leachate metal uptakes from Amberlite IRC-748 and Zr-MOF-808. The suggestions and improvements for the methodologies used in this study are as follows for the reference of future actions on it.

The leaching conditions used for the leaching experiments were taken from the previous studies. However, the conditions used did not leach out the metals as expected and recorded in the literature. Therefore, optimizing the leaching process with the selected citric acid is necessary by varying the conditions such as acid concentration, reaction temperature, time, reducing conditions and liquid-solid ratio.

- The aqua regia digestion did not successfully extract the total amount of metals to the solution phase. Hence the digestion conditions need to be optimized or multiple digestions until the digested black mass residue does not indicate any metals.
- Black mass composition varies to a great extent due to the heterogeneity in the powdered mixture. Therefore, when conducting leaching experiments, using the same sample to analyze a structural or a composition change is recommended for the black mass characterization techniques.
- The Ni^{2+} and Co^{2+} calibration curves for the UV-visible spectroscopy need to be extended for lower concentrations because the metal adsorbed solutions resulted in very low absorbance values.
- The adsorption studies conducted with MOF-808 for pH 6 adjusted black mass leachate did not result in any leachate metal uptakes as expected, possibly due to the effect of high pH on the chemical stability of the MOF-808 or interference due to the high concentration of Na^+ from NaOH addition for pH adjustment. Therefore, conducting the same experiment at pH 2 or without any pH adjustment is recommended.

The following future works are recommended as a follow up for this study.

- Optimize acid elution recovery of resin adsorbed metals by changing the acid concentration, elution time and temperature.
- Determine MOF-808 adsorption kinetics and isotherms. The adsorption kinetics are critical because over-contacting the MOF-808 with black mass leachates possibly affect the MOFs' chemical stability.

- Analyze Ni²⁺ and Co²⁺ adsorption selectivity using MOF-808 analogues by varying pore sizes and active functional groups.
- Conduct MOF-808-EDTA column adsorption experiments.

REFERENCES

- Ahn, N.-K., Swain, B., Shim, H.-W., & Kim, D.-W. (2019). Recovery of Rare Earth Oxide from Waste NiMH Batteries by Simple Wet Chemical Valorization Process. *Metals*, 9(11), 1151. <https://doi.org/10.3390/met9111151>
- Alonso, A. R., Pérez, E. A., Lapidus, G. T., & Luna-Sánchez, R. M. (2015). Hydrometallurgical process for rare earth elements recovery from spent Ni-HM batteries. *Canadian Metallurgical Quarterly*, 54(3), 310–317. <https://doi.org/10.1179/1879139515Y.0000000013>
- Anirudhan, T. S., Shainy, F., & Deepa, J. R. (2019). Effective removal of Cobalt(II) ions from aqueous solutions and nuclear industry wastewater using sulfhydryl and carboxyl functionalised magnetite nanocellulose composite: batch adsorption studies. *Chemistry and Ecology*, 35(3), 235–255. <https://doi.org/10.1080/02757540.2018.1532999>
- Ardila-Suárez, C., Molina V., D. R., Alem, H., Baldovino Medrano, V. G., & Ramírez-Caballero, G. E. (2019). Synthesis of Ordered Microporous/Macroporous MOF-808 through Modulator-Induced Defect Formation, and Surfactant Self-Assembly Strategies. Advance online publication. <https://doi.org/10.26434/chemrxiv.10316924.v1>
- Aunan, E., Affolter, C. W., Olsbye, U., & Lillerud, K. P [Karl Petter] (2021). Modulation of the Thermochemical Stability and Adsorptive Properties of MOF-808 by the Selection of Non-structural Ligands. *Chemistry of Materials*, 33(4), 1471–1476. <https://doi.org/10.1021/acs.chemmater.0c04823>
- Azevedo, M., Campagnol, N., Hagenbruch, T., Hoffman, K., Lala, A., & Ramsbottom, O. (2018). *lithium-and-cobalt-a-tale-of-two-commodities*.
- Basuki, K. T., Hasnowo, L. A., & Jamayanti, E. (2019). ADSORPTION OF URANIUM SIMULATION WASTE USING BENTONITE:TITANIUM DIOXIDE. *Urania Jurnal Ilmiah Daur Bahan Bakar Nuklir*, 25(1). <https://doi.org/10.17146/urania.2019.25.1.4527>
- Botelho Junior, A. B., Dreisinger, D. B., & Espinosa, D. C. R. (2019). A Review of Nickel, Copper, and Cobalt Recovery by Chelating Ion Exchange Resins from Mining Processes and Mining Tailings. *Mining, Metallurgy & Exploration*, 36(1), 199–213. <https://doi.org/10.1007/s42461-018-0016-8>
- Boydén, A., Soo, V. K., & Doolan, M. (2016). The Environmental Impacts of Recycling Portable Lithium-Ion Batteries. *Procedia CIRP*, 48, 188–193. <https://doi.org/10.1016/j.procir.2016.03.100>
- Bożęcka, A., Orlof-Naturalna, M., & Korpalski, A. (2020). Comparison of Copper and Cobalt Ions Sorption from Aqueous Solutions on Selected Sorbents. *Journal of Ecological Engineering*, 21(8), 84–90. <https://doi.org/10.12911/22998993/127164>
- Bruce, P. G., Scrosati, B., & Tarascon, J.-M. (2008). Nanomaterials for rechargeable lithium batteries. *Angewandte Chemie (International Ed. In English)*, 47(16), 2930–2946. <https://doi.org/10.1002/anie.200702505>
- Cavka, J. H., Jakobsen, S., Olsbye, U., Guillou, N., Lamberti, C., Bordiga, S., & Lillerud, K. P [Karl Petter] (2008). A new zirconium inorganic building brick forming

- metal organic frameworks with exceptional stability. *Journal of the American Chemical Society*, 130(42), 13850–13851. <https://doi.org/10.1021/ja8057953>
- Chagnes, A., & Pospiech, B. (2013). A brief review on hydrometallurgical technologies for recycling spent lithium-ion batteries. *Journal of Chemical Technology & Biotechnology*, 88(7), 1191–1199. <https://doi.org/10.1002/jctb.4053>
- Chagnes, A., & Swiatowsk, J. (2012). Electrolyte and Solid-Electrolyte Interphase Layer in Lithium-Ion Batteries. Advance online publication. <https://doi.org/10.5772/31112>
- Chen, X [Xiangping], Cao, L., Kang, D., Li, J [Jiazhu], Zhou, T., & Ma, H. (2018). Recovery of valuable metals from mixed types of spent lithium ion batteries. Part II: Selective extraction of lithium. *Waste Management (New York, N.Y.)*, 80, 198–210. <https://doi.org/10.1016/j.wasman.2018.09.013>
- Chen, X [Xiangping], Fan, B., Xu, L., Zhou, T., & Kong, J. (2016). An atom-economic process for the recovery of high value-added metals from spent lithium-ion batteries. *Journal of Cleaner Production*, 112, 3562–3570. <https://doi.org/10.1016/j.jclepro.2015.10.132>
- Chen, X [Xiangping], Kang, D., Cao, L., Li, J [Jiazhu], Zhou, T., & Ma, H. (2019). Separation and recovery of valuable metals from spent lithium ion batteries: Simultaneous recovery of Li and Co in a single step. *Separation and Purification Technology*, 210, 690–697. <https://doi.org/10.1016/j.seppur.2018.08.072>
- Chen, X [Xiangping], & Zhou, T. (2014). Hydrometallurgical process for the recovery of metal values from spent lithium-ion batteries in citric acid media. *Waste Management & Research : The Journal of the International Solid Wastes and Public Cleansing Association, ISWA*, 32(11), 1083–1093. <https://doi.org/10.1177/0734242X14557380>
- Chen, X [Xinyu], Chen, D., Li, N., Xu, Q [Qingfeng], Li, H., He, J., & Lu, J. (2020). Modified-MOF-808-Loaded Polyacrylonitrile Membrane for Highly Efficient, Simultaneous Emulsion Separation and Heavy Metal Ion Removal. *ACS Applied Materials & Interfaces*, 12(35), 39227–39235. <https://doi.org/10.1021/acsami.0c10290>
- Chen, Z., Zhang, L [Lingen], & Xu, Z. (2020). Analysis of cobalt flows in mainland China: Exploring the potential opportunities for improving resource efficiency and supply security. *Journal of Cleaner Production*, 275, 122841. <https://doi.org/10.1016/j.jclepro.2020.122841>
- Dichiara, A. B., Harlander, S. F., & Rogers, R. E. (2015). Fixed bed adsorption of diquat dibromide from aqueous solution using carbon nanotubes. *RSC Advances*, 5(76), 61508–61512. <https://doi.org/10.1039/C5RA11167F>
- Dorella, G., & Mansur, M. B. (2007). A study of the separation of cobalt from spent Li-ion battery residues. *Journal of Power Sources*, 170(1), 210–215. <https://doi.org/10.1016/j.jpowsour.2007.04.025>
- Efome, J. E., Rana, D., Matsuura, T., & Lan, C. Q. (2018). Insight Studies on Metal-Organic Framework Nanofibrous Membrane Adsorption and Activation for Heavy Metal Ions Removal from Aqueous Solution. *ACS Applied Materials & Interfaces*, 10(22), 18619–18629. <https://doi.org/10.1021/acsami.8b01454>

- Etacheri, V., Marom, R., Elazari, R., Salitra, G., & Aurbach, D. (2011). Challenges in the development of advanced Li-ion batteries: a review. *Energy & Environmental Science*, 4(9), 3243. <https://doi.org/10.1039/c1ee01598b>
- Farha, O. K., & Hupp, J. T. (2010). Rational design, synthesis, purification, and activation of metal-organic framework materials. *Accounts of Chemical Research*, 43(8), 1166–1175. <https://doi.org/10.1021/ar1000617>
- Fila, D., Hubicki, Z., & Kołodyńska, D. (2019). Recovery of metals from waste nickel-metal hydride batteries using multifunctional Diphonix resin. *Adsorption*, 25(3), 367–382. <https://doi.org/10.1007/s10450-019-00013-9>
- Furukawa, H., Gándara, F., Zhang, Y.-B., Jiang, J [Juncong], Queen, W. L., Hudson, M. R., & Yaghi, O. M. (2014). Water adsorption in porous metal-organic frameworks and related materials. *Journal of the American Chemical Society*, 136(11), 4369–4381. <https://doi.org/10.1021/ja500330a>
- Garole, D. J., Hossain, R., Garole, V. J., Sahajwalla, V., Nerkar, J., & Dubal, D. P. (2020). Recycle, Recover and Repurpose Strategy of Spent Li-ion Batteries and Catalysts: Current Status and Future Opportunities. *ChemSusChem*, 13(12), 3079–3100. <https://doi.org/10.1002/cssc.201903213>
- Georgi-Maschler, T., Friedrich, B., Weyhe, R., Heegn, H., & Rutz, M. (2012). Development of a recycling process for Li-ion batteries. *Journal of Power Sources*, 207, 173–182. <https://doi.org/10.1016/j.jpowsour.2012.01.152>
- Guo, F., Nishihama, S., & Yoshizuka, K. (2012). Selective Recovery of Copper, Cobalt, and Nickel from Aqueous Chloride Media using Solvent Impregnated Resins. *Solvent Extraction and Ion Exchange*, 30(6), 579–592. <https://doi.org/10.1080/07366299.2012.671114>
- Guo, F., Nishihama, S., & Yoshizuka, K. (2013). Selective recovery of valuable metals from spent Li-ion batteries using solvent-impregnated resins. *Environmental Technology*, 34(9-12), 1307–1317. <https://doi.org/10.1080/09593330.2012.746734>
- Guo, H., Min, Z., Hao, Y., Wang, X [Xu], Fan, J., Shi, P., Min, Y., & Xu, Q [Qunjie] (2021). Sustainable recycling of LiCoO₂ cathode scrap on the basis of successive peroxymonosulfate activation and recovery of valuable metals. *The Science of the Total Environment*, 759, 143478. <https://doi.org/10.1016/j.scitotenv.2020.143478>
- Guo, Y., Li, F., Zhu, H., Li, G., Huang, J., & He, W. (2016). Leaching lithium from the anode electrode materials of spent lithium-ion batteries by hydrochloric acid (HCl). *Waste Management (New York, N.Y.)*, 51, 227–233. <https://doi.org/10.1016/j.wasman.2015.11.036>
- Gutov, O. V., Molina, S., Escudero-Adán, E. C., & Shafir, A. (2016). Modulation by Amino Acids: Toward Superior Control in the Synthesis of Zirconium Metal-Organic Frameworks. *Chemistry (Weinheim an Der Bergstrasse, Germany)*, 22(38), 13582–13587. <https://doi.org/10.1002/chem.201600898>
- Harper, G., Sommerville, R., Kendrick, E., Driscoll, L., Slater, P., Stolkin, R., Walton, A., Christensen, P., Heidrich, O., Lambert, S., Abbott, A., Ryder, K., Gaines, L., & Anderson, P. (2019). Recycling lithium-ion batteries from electric vehicles. *Nature*, 575(7781), 75–86. <https://doi.org/10.1038/s41586-019-1682-5>

- He, L.-P., Sun, S.-Y., Mu, Y.-Y., Song, X.-F., & Yu, J.-G. (2017). Recovery of Lithium, Nickel, Cobalt, and Manganese from Spent Lithium-Ion Batteries Using L-Tartaric Acid as a Leachant. *ACS Sustainable Chemistry & Engineering*, 5(1), 714–721. <https://doi.org/10.1021/acssuschemeng.6b02056>
- Henckens, M., & Worrell, E. (2020). Reviewing the availability of copper and nickel for future generations. The balance between production growth, sustainability and recycling rates. *Journal of Cleaner Production*, 264, 121460. <https://doi.org/10.1016/j.jclepro.2020.121460>
- Jacoby, M. (2019). It's time to recycle lithium-ion batteries. *C&EN Global Enterprise*, 97(28), 29–32. <https://doi.org/10.1021/cen-09728-cover>
- Ji, C., Ren, Y., Yu, H [Hang], Hua, M., Lv, L., & Zhang, W [Weiming] (2022). Highly efficient and selective Hg(II) removal from water by thiol-functionalized MOF-808: Kinetic and mechanism study. *Chemical Engineering Journal*, 430, 132960. <https://doi.org/10.1016/j.cej.2021.132960>
- Jiang, F., Chen, Y [Yuqian], Ju, S., Zhu, Q., Zhang, L [Libo], Peng, J., Wang, X [Xuming], & Miller, J. D. (2018). Ultrasound-assisted leaching of cobalt and lithium from spent lithium-ion batteries. *Ultrasonics Sonochemistry*, 48, 88–95. <https://doi.org/10.1016/j.ultsonch.2018.05.019>
- Jiang, J [Juncong], Gándara, F., Zhang, Y.-B., Na, K., Yaghi, O. M., & Klemperer, W. G. (2014). Superacidity in sulfated metal-organic framework-808. *Journal of the American Chemical Society*, 136(37), 12844–12847. <https://doi.org/10.1021/ja507119n>
- Jiang, X., Yang, L., Yang, Q., Xiong, C., Jiang, J [Jianxiong], Jia, Q., & Chen, Q. (2014). Adsorption Behaviour of Co(II) from Aqueous Solutions onto D113-III Resin. *Asian Journal of Chemistry*, 26(7), 2022–2026. <https://doi.org/10.14233/ajchem.2014.15627>
- Joulié, M., Laucournet, R., & Billy, E. (2014). Hydrometallurgical process for the recovery of high value metals from spent lithium nickel cobalt aluminum oxide based lithium-ion batteries. *Journal of Power Sources*, 247, 551–555. <https://doi.org/10.1016/j.jpowsour.2013.08.128>
- Korkmaz, K., Alemrajabi, M., Rasmuson, Å., & Forsberg, K. (2018). Recoveries of Valuable Metals from Spent Nickel Metal Hydride Vehicle Batteries via Sulfation, Selective Roasting, and Water Leaching. *Journal of Sustainable Metallurgy*, 4(3), 313–325. <https://doi.org/10.1007/s40831-018-0169-1>
- Ku, H., Jung, Y., Jo, M., Park, S., Kim, S., Yang, D., Rhee, K., An, E.-M., Sohn, J., & Kwon, K. (2016). Recycling of spent lithium-ion battery cathode materials by ammoniacal leaching. *Journal of Hazardous Materials*, 313, 138–146. <https://doi.org/10.1016/j.jhazmat.2016.03.062>
- Li, Z.-Q., Yang, J.-C., Sui, K.-W., & Yin, N. (2015). Facile synthesis of metal-organic framework MOF-808 for arsenic removal. *Materials Letters*, 160, 412–414. <https://doi.org/10.1016/j.matlet.2015.08.004>
- Li Li, Jun Lu, Yang Ren, Xiao Xiao Zhang, Ren Jie Chen, Feng Wu, & Khalil Amine (2012). Ascorbic-acid-assisted recovery of cobalt and lithium from spent Li-ion batteries. *Journal of Power Sources*, 218, 21–27.

- Li Li, Renjie Chen, Feng Sun, Feng Wu, & Jianrui Liu (2011). Preparation of LiCoO₂ films from spent lithium-ion batteries by a combined recycling process. *Hydrometallurgy*, *108*, 220–225.
- Liang, Y., Zhao, C.-Z., Yuan, H., Chen, Y [Yuan], Zhang, W [Weicai], Huang, J.-Q., Yu, D., Liu, Y [Yingliang], Titirici, M.-M., Chueh, Y.-L., Yu, H [Haijun], & Zhang, Q [Qiang] (2019). A review of rechargeable batteries for portable electronic devices. *InfoMat*, *1*(1), 6–32. <https://doi.org/10.1002/inf2.12000>
- Lin, S., Zhao, Y., Bediako, J. K., Cho, C.-W., Sarkar, A. K., Lim, C.-R., & Yun, Y.-S. (2019). Structure-controlled recovery of palladium(II) from acidic aqueous solution using metal-organic frameworks of MOF-802, UiO-66 and MOF-808. *Chemical Engineering Journal*, *362*, 280–286. <https://doi.org/10.1016/j.cej.2019.01.044>
- Liu, Q [Qifeng], Zhang, Q [Qian], Liu, B., & Ma, J. (2019). A new synthesis and adsorption mechanism of ZrO₂ based metal-organic frames for efficient removal of mercury ions from aqueous solution. *Ceramics International*, *45*(12), 15720–15724. <https://doi.org/10.1016/j.ceramint.2019.04.246>
- Marzbali, M. H., & Esmaili, M. (2017). Fixed bed adsorption of tetracycline on a mesoporous activated carbon: Experimental study and neuro-fuzzy modeling. *Journal of Applied Research and Technology*, *15*(5), 454–463. <https://doi.org/10.1016/j.jart.2017.05.003>
- Mendes, F. D., & Martins, A. H. (2004). Selective sorption of nickel and cobalt from sulphate solutions using chelating resins. *International Journal of Mineral Processing*, *74*(1-4), 359–371. <https://doi.org/10.1016/j.minpro.2004.04.003>
- Mendes, F. D., & Martins, A. H. (2005). Recovery of nickel and cobalt from acid leach pulp by ion exchange using chelating resin. *Minerals Engineering*, *18*(9), 945–954. <https://doi.org/10.1016/j.mineng.2004.12.009>
- Meng, X., Wang, H.-N., Wang, L.-S., Zou, Y.-H., & Zhou, Z.-Y. (2019). Enhanced proton conductivity of a MOF-808 framework through anchoring organic acids to the zirconium clusters by post-synthetic modification. *CrystEngComm*, *21*(20), 3146–3150. <https://doi.org/10.1039/C9CE00328B>
- Meshram, P., Pandey, B. D [B. D.], & Mankhand, T. R [T. R.] (2015). Hydrometallurgical processing of spent lithium ion batteries (LIBs) in the presence of a reducing agent with emphasis on kinetics of leaching. *Chemical Engineering Journal*, *281*, 418–427. <https://doi.org/10.1016/j.cej.2015.06.071>
- Meshram, P., Somani, H., Pandey, B. D [Banshi Dhar], Mankhand, T. R [Tilak Raj], Deveci, H., & Abhilash (2017). Two stage leaching process for selective metal extraction from spent nickel metal hydride batteries. *Journal of Cleaner Production*, *157*, 322–332. <https://doi.org/10.1016/j.jclepro.2017.04.144>
- Mishra, D., Kim, D.-J., Ralph, D. E., Ahn, J.-G., & Rhee, Y.-H. (2008). Bioleaching of metals from spent lithium ion secondary batteries using *Acidithiobacillus ferrooxidans*. *Waste Management (New York, N.Y.)*, *28*(2), 333–338. <https://doi.org/10.1016/j.wasman.2007.01.010>
- Moon, S.-Y., Liu, Y [Yangyang], Hupp, J. T., & Farha, O. K. (2015). Instantaneous hydrolysis of nerve-agent simulants with a six-connected zirconium-based metal-

- organic framework. *Angewandte Chemie (International Ed. In English)*, 54(23), 6795–6799. <https://doi.org/10.1002/anie.201502155>
- Naderi, M. (2015). *Surface Area Brunauer–Emmett–Teller (BET)*. Elsevier Ltd. <https://doi.org/10.1016/B978-0-12-384746-1.00014-8>
- Nayaka, G. P., Pai, K. V., Manjanna, J., & Keny, S. J. (2016). Use of mild organic acid reagents to recover the Co and Li from spent Li-ion batteries. *Waste Management (New York, N.Y.)*, 51, 234–238. <https://doi.org/10.1016/j.wasman.2015.12.008>
- Øien-Ødegaard, S., Shearer, G. C [G. C.], Wragg, D. S., & Lillerud, K. P [K. P.] (2017). Pitfalls in metal-organic framework crystallography: Towards more accurate crystal structures. *Chemical Society Reviews*, 46(16), 4867–4876. <https://doi.org/10.1039/c6cs00533k>
- Olsztyńska-Janus, S., Pietruszka, A., Kielbowicz, Z., & Czarnecki, M. A. (2018). Atr-IR study of skin components: Lipids, proteins and water. Part I: Temperature effect. *Spectrochimica Acta. Part A, Molecular and Biomolecular Spectroscopy*, 188, 37–49. <https://doi.org/10.1016/j.saa.2017.07.001>
- Ordoñez, J., Gago, E. J., & Girard, A. (2016). Processes and technologies for the recycling and recovery of spent lithium-ion batteries. *Renewable and Sustainable Energy Reviews*, 60, 195–205. <https://doi.org/10.1016/j.rser.2015.12.363>
- Panahi, H. A., Sadeghi, H. B., Farahmandnejad, N., Badr, A. R., & Moniri, E. (2012). Removal of cobalt from human serum and environmental samples by adsorption using Amberlite XAD-2–salicylic acid–iminodiacetic acid. *Desalination and Water Treatment*, 46(1-3), 244–255. <https://doi.org/10.1080/19443994.2012.677530>
- Patel, H. (2019). Fixed-bed column adsorption study: a comprehensive review. *Applied Water Science*, 9(3). <https://doi.org/10.1007/s13201-019-0927-7>
- Peng, C., Liu, F., Aji, A. T., Wilson, B. P., & Lundström, M. (2019). Extraction of Li and Co from industrially produced Li-ion battery waste - Using the reductive power of waste itself. *Waste Management (New York, N.Y.)*, 95, 604–611. <https://doi.org/10.1016/j.wasman.2019.06.048>
- Peng, Y., Huang, H., Zhang, Y [Yuxi], Kang, C., Chen, S., Song, L., Liu, D., & Zhong, C. (2018). A versatile MOF-based trap for heavy metal ion capture and dispersion. *Nature Communications*, 9(1), 187. <https://doi.org/10.1038/s41467-017-02600-2>
- Piątek, J., Afyon, S., Budnyak, T. M., Budnyk, S., Sipponen, M. H., & Slabon, A. (2020). Sustainable Li-Ion Batteries: Chemistry and Recycling. *Advanced Energy Materials*, 2003456. <https://doi.org/10.1002/aenm.202003456>
- Pospiech, B. (2014). Selective recovery of cobalt(II) towards lithium(I) from chloride media by transport across polymer inclusion membrane with triisooctylamine. *Pjct*, 16(1), 15–20. <https://doi.org/10.2478/pjct-2014-0003>
- Pradhan, S., Nayak, R., & Mishra, S. (2021). A review on the recovery of metal values from spent nickel metal hydride and lithium-ion batteries. *International Journal of Environmental Science and Technology*. Advance online publication. <https://doi.org/10.1007/s13762-021-03356-5>
- Rabah, M. A., Farghaly, F. E., & Abd-El Motaleb, M. A. (2008). Recovery of nickel, cobalt and some salts from spent Ni-MH batteries. *Waste Management (New York, N.Y.)*, 28(7), 1159–1167. <https://doi.org/10.1016/j.wasman.2007.06.007>

- Rodrigues, L. E. O. C., & Mansur, M. B. (2010). Hydrometallurgical separation of rare earth elements, cobalt and nickel from spent nickel–metal–hydride batteries. *Journal of Power Sources*, 195(11), 3735–3741. <https://doi.org/10.1016/j.jpowsour.2009.12.071>
- Rouquerol, J., Llewellyn, P., & Rouquerol, F. Is the bet equation applicable to microporous adsorbents?, *160*, 49–56. [https://doi.org/10.1016/S0167-2991\(07\)80008-5](https://doi.org/10.1016/S0167-2991(07)80008-5)
- Scott, K. (2009). *Nickel Metal Hydride Batteries*. MDPI. <https://doi.org/10.3390/books978-3-03842-303-4>
- Shearer, G. C [Greig C.], Chavan, S., Bordiga, S., Svelle, S., Olsbye, U., & Lillerud, K. P [Karl Petter] (2016). Defect Engineering: Tuning the Porosity and Composition of the Metal–Organic Framework UiO-66 via Modulated Synthesis. *Chemistry of Materials*, 28(11), 3749–3761. <https://doi.org/10.1021/acs.chemmater.6b00602>
- Sobianowska-Turek, A. (2018). Hydrometallurgical recovery of metals: Ce, La, Co, Fe, Mn, Ni and Zn from the stream of used Ni-MH cells. *Waste Management (New York, N.Y.)*, 77, 213–219. <https://doi.org/10.1016/j.wasman.2018.03.046>
- Steward, D., Mayyas, A., & Mann, M. (2019). Economics and Challenges of Li-Ion Battery Recycling from End-of-Life Vehicles. *Procedia Manufacturing*, 33, 272–279. <https://doi.org/10.1016/j.promfg.2019.04.033>
- Sun, X., Hao, H., Liu, Z., Zhao, F., & Song, J. (2019). Tracing global cobalt flow: 1995–2015. *Resources, Conservation and Recycling*, 149, 45–55. <https://doi.org/10.1016/j.resconrec.2019.05.009>
- Trickett, C. A., Popp, T. M. O., Su, J., Yan, C., Weisberg, J., Huq, A., Urban, P., Jiang, J [Juncong], Kalmutzki, M. J., Liu, Q [Qingni], Baek, J., Head-Gordon, M. P., Somorjai, G. A., Reimer, J. A., & Yaghi, O. M. (2019). *CCDC 1871192: Experimental Crystal Structure Determination*. <https://doi.org/10.5517/CCDC.CSD.CC20T411>
- U.S. Geological Survey (2021). Mineral commodity summaries 2021.
- Uemura, T., Yanai, N., & Kitagawa, S. (2009). Polymerization reactions in porous coordination polymers. *Chemical Society Reviews*, 38(5), 1228–1236. <https://doi.org/10.1039/b802583p>
- Ugwu, E. I., Tursunov, O., Kodirov, D., Shaker, L. M., Al-Amiery, A. A., Yangibaeva, I., & Shavkarov, F. (2020). Adsorption mechanisms for heavy metal removal using low cost adsorbents: A review. *IOP Conference Series: Earth and Environmental Science*, 614(1), 12166. <https://doi.org/10.1088/1755-1315/614/1/012166>
- van den Brink, S., Kleijn, R., Sprecher, B., & Tukker, A. (2020). Identifying supply risks by mapping the cobalt supply chain. *Resources, Conservation and Recycling*, 156, 104743. <https://doi.org/10.1016/j.resconrec.2020.104743>
- Vaughan, J., Dieters, C., Fu, W., & Byrne, K. (2016). Properties of Lewatit® TP272, a commercial solvent impregnated cation exchange resin for cobalt recovery. *Minerals Engineering*, 88, 2–8. <https://doi.org/10.1016/j.mineng.2015.07.005>
- Wan, S., Ma, M., Lv, L., Qian, L., Xu, S., Xue, Y., & Ma, Z. (2014). Selective capture of thallium(I) ion from aqueous solutions by amorphous hydrous manganese dioxide. *Chemical Engineering Journal*, 239, 200–206. <https://doi.org/10.1016/j.cej.2013.11.010>

- Wang, H., Huang, K., Zhang, Y [Yang], Chen, X [Xin], Jin, W., Zheng, S., Zhang, Y [Yi], & Li, P. (2017). Recovery of Lithium, Nickel, and Cobalt from Spent Lithium-Ion Battery Powders by Selective Ammonia Leaching and an Adsorption Separation System. *ACS Sustainable Chemistry & Engineering*, 5(12), 11489–11495. <https://doi.org/10.1021/acssuschemeng.7b02700>
- Wang, J., Lv, J., Zhang, M., Tang, M., Lu, Q., Qin, Y., Lu, Y., & Yu, B. (2021). Recycling lithium cobalt oxide from its spent batteries: An electrochemical approach combining extraction and synthesis. *Journal of Hazardous Materials*, 405, 124211. <https://doi.org/10.1016/j.jhazmat.2020.124211>
- Wang, M.-M., Zhang, C.-C., & Zhang, F.-S. (2016). An environmental benign process for cobalt and lithium recovery from spent lithium-ion batteries by mechanochemical approach. *Waste Management (New York, N.Y.)*, 51, 239–244. <https://doi.org/10.1016/j.wasman.2016.03.006>
- Wang, M.-M., Zhang, C.-C., & Zhang, F.-S. (2017). Recycling of spent lithium-ion battery with polyvinyl chloride by mechanochemical process. *Waste Management (New York, N.Y.)*, 67, 232–239. <https://doi.org/10.1016/j.wasman.2017.05.013>
- Winarta, J., Shan, B., McIntyre, S. M., Ye, L., Wang, C., Liu, J., & Mu, B. (2020). A Decade of UiO-66 Research: A Historic Review of Dynamic Structure, Synthesis Mechanisms, and Characterization Techniques of an Archetypal Metal–Organic Framework. *Crystal Growth & Design*, 20(2), 1347–1362. <https://doi.org/10.1021/acs.cgd.9b00955>
- XIA, Y., XIAO, L., TIAN, J., LI, Z., & ZENG, L. (2015). Recovery of rare earths from acid leach solutions of spent nickel-metal hydride batteries using solvent extraction. *Journal of Rare Earths*, 33(12), 1348–1354. [https://doi.org/10.1016/S1002-0721\(14\)60568-8](https://doi.org/10.1016/S1002-0721(14)60568-8)
- Yang, X., Zhang, J., & Fang, X. (2014). Rare earth element recycling from waste nickel-metal hydride batteries. *Journal of Hazardous Materials*, 279, 384–388. <https://doi.org/10.1016/j.jhazmat.2014.07.027>
- Yao, L., Feng, Y., & Xi, G. (2015). A new method for the synthesis of LiNi 1/3 Co 1/3 Mn 1/3 O 2 from waste lithium ion batteries. *RSC Advances*, 5(55), 44107–44114. <https://doi.org/10.1039/C4RA16390G>
- Yuliusman, Nurqomariah, A., Fajaryanto, R., & Silvia (2018). Leaching and kinetics process of cobalt from used lithium ion batteries with organic citric acid. *E3S Web of Conferences*, 67, 3036. <https://doi.org/10.1051/e3sconf/20186703036>
- Zainol, Z., & Nicol, M. J. (2009a). Comparative study of chelating ion exchange resins for the recovery of nickel and cobalt from laterite leach tailings. *Hydrometallurgy*, 96(4), 283–287. <https://doi.org/10.1016/j.hydromet.2008.11.005>
- Zainol, Z., & Nicol, M. J. (2009b). Ion-exchange equilibria of Ni²⁺, Co²⁺, Mn²⁺ and Mg²⁺ with iminodiacetic acid chelating resin Amberlite IRC 748. *Hydrometallurgy*, 99(3-4), 175–180. <https://doi.org/10.1016/j.hydromet.2009.08.004>
- Zeng, G., Deng, X., Luo, S., Luo, X., & Zou, J. (2012). A copper-catalyzed bioleaching process for enhancement of cobalt dissolution from spent lithium-ion batteries. *Journal of Hazardous Materials*, 199-200, 164–169. <https://doi.org/10.1016/j.jhazmat.2011.10.063>

- Zeng, X., Li, J [Jinhui], & Shen, B. (2015). Novel approach to recover cobalt and lithium from spent lithium-ion battery using oxalic acid. *Journal of Hazardous Materials*, 295, 112–118. <https://doi.org/10.1016/j.jhazmat.2015.02.064>
- Zeng, X., Li, J [Jinhui], & Singh, N. (2014). Recycling of Spent Lithium-Ion Battery: A Critical Review. *Critical Reviews in Environmental Science and Technology*, 44(10), 1129–1165. <https://doi.org/10.1080/10643389.2013.763578>
- Zhao, J., Zhang, B., Xie, H., Qu, J., Qu, X., Xing, P., & Yin, H. (2020). Hydrometallurgical recovery of spent cobalt-based lithium-ion battery cathodes using ethanol as the reducing agent. *Environmental Research*, 181, 108803. <https://doi.org/10.1016/j.envres.2019.108803>
- Zheng, X., Zhu, Z., Lin, X., Zhang, Y [Yi], He, Y., Cao, H., & Sun, Z. (2018). A Mini-Review on Metal Recycling from Spent Lithium Ion Batteries. *Engineering*, 4(3), 361–370. <https://doi.org/10.1016/j.eng.2018.05.018>
- Zhou, H.-C., Long, J. R., & Yaghi, O. M. (2012). Introduction to metal-organic frameworks. *Chemical Reviews*, 112(2), 673–674. <https://doi.org/10.1021/cr300014x>

APPENDIX

Appendix 1-XRF analyzed aqua regia digestion

Description	MgO	Al ₂ O ₃	SiO ₂	P	S	Ca	Cr	Mn	Fe	Co	Ni	Cu	Zn	Zr	Mo
black mass	0.89	3.6	1.91	0.1	0.35	0.38	0.16	3.36	0.41	1.75	48.57	3.83	0.28	0.11	0.02
Aqua regia leached-black mass residue	0.82	4.9	9.54	0.14	0	0.14	0.64	1.34	0.27	1.41	9.82	1.7	0.21	0.66	0
Aqua regia +H ₂ O ₂ leached-black mass residue	0.79	5.23	10.75	0.14	0	0.12	0.71	1.28	0.24	1.32	8.22	1.6	0.25	0.74	0
Removal percentage Aqua regia leaching	7.87	-36.11	-399.48	-40	100	63.16	-300	60.12	34.15	19.43	79.78	55.61	25	-500	100
Removal percentage Aqua regia +H ₂ O ₂ leaching	11.24	-45.28	-462.83	-40	100	68.42	-343.75	61.9	41.46	24.57	83.08	58.22	10.71	-572.73	100

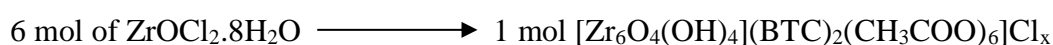
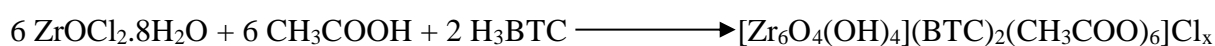
Appendix 2-Comparison of leaching results of ICP-OES and XRF

Leaching system	Leachate metal %(w/w)-ICP-OES			Leachate metal %(w/w)-XRF		
	Co	Mn	Ni	Co	Mn	Ni
Aqua regia leached P414 A	6.05	5.22	20.8	1.86	4.99	30.02
Aqua regia leached P414 B	5.83	5.09	20.62	2.01	4.58	37.9
Aqua regia leached P414 C	5.85	5.07	21.06	1.64	4.7	27.3
Aqua regia +H ₂ O ₂ leached P414A	5.8	5.18	20.28	2.06	5.12	31.12
Aqua regia +H ₂ O ₂ leached P414B	5.35	4.72	18.69	2.06	4.61	39.6
Aqua regia +H ₂ O ₂ leached P414C	5.98	5.4	20.93	1.72	4.71	29.3

Appendix 3-Determination of spent battery cathode configuration

Metal	Weight percentage	Moles in 100 g	Simplest mole ratio	mole ratio
Nickel	20.3	0.346	3.6	7
Manganese	5.3	0.096	1	2
Cobalt	6.25	0.106	1.1	2

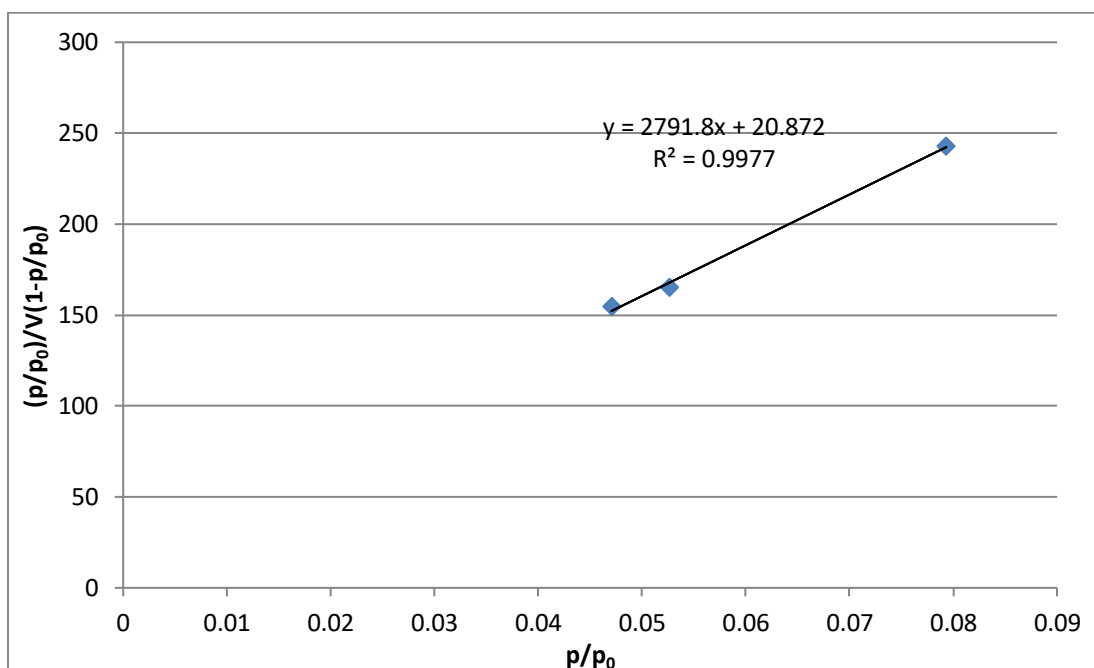
Appendix 4-Calculation of Theoretical yield of MOF-808-acetate



ZrOCl₂·8H₂O mass used = 1.815 g

$$\begin{aligned} \text{Theoretical yield} &= \frac{1.815 \times 98\% \text{ g ZrOCl}_2 \cdot 8\text{H}_2\text{O}}{322.252 \text{ g} \frac{\text{ZrOCl}_2 \cdot 8\text{H}_2\text{O}}{\text{mol ZrOCl}_2 \cdot 8\text{H}_2\text{O}}} \times \frac{1 \text{ mol product}}{6 \text{ mol ZrOCl}_2 \cdot 8\text{H}_2\text{O}} \times 1447.759 \frac{\text{g product}}{\text{mol product}} \\ &= 1.33 \text{ g} \end{aligned}$$

Appendix 5-Calculations from BET curve for MOF-808-acetate

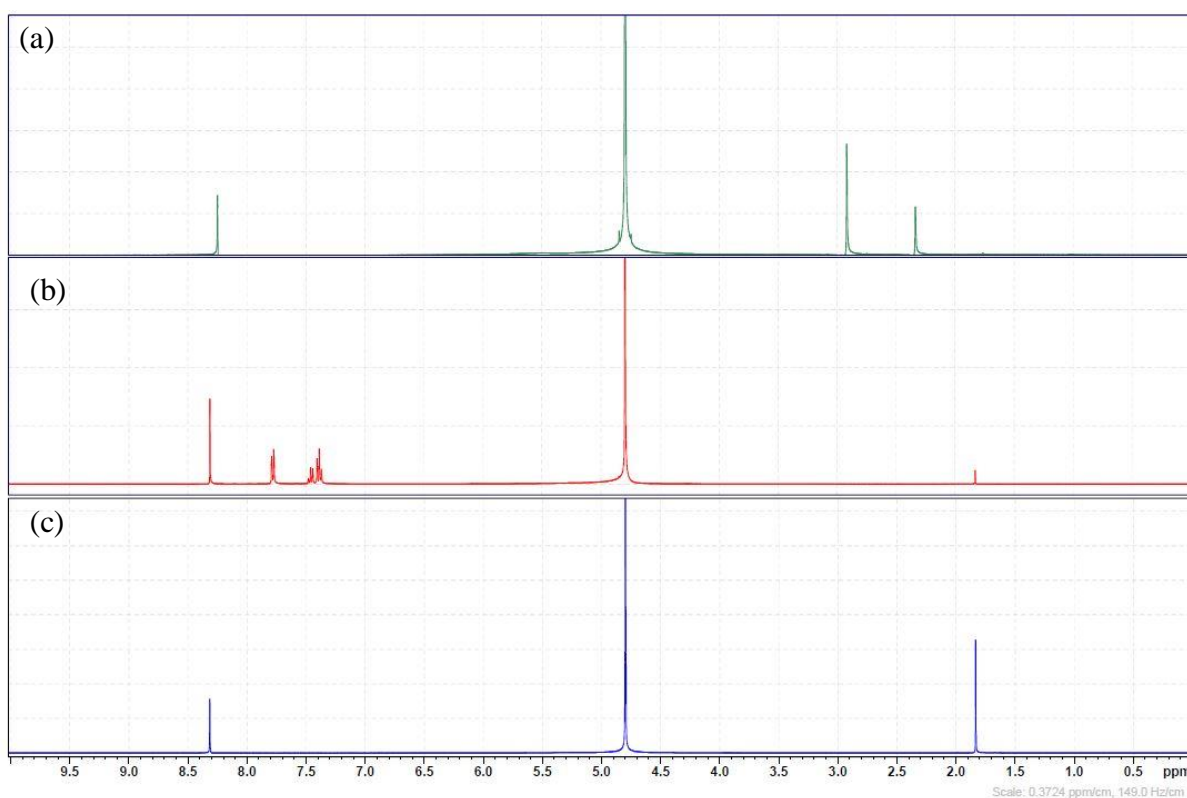


$$C = 1 + \frac{\text{gradient}}{\text{intercept}} = 1 + \frac{2791.80}{20.87} = 134.76$$

$$V_m = \frac{1}{\text{gradient+slope}} = \frac{1}{2791.80+20.87} = 0.000356 \text{ m}^3 \text{ (STP) g}^{-1} = 356 \text{ cm}^3 \text{ (STP) g}^{-1}$$

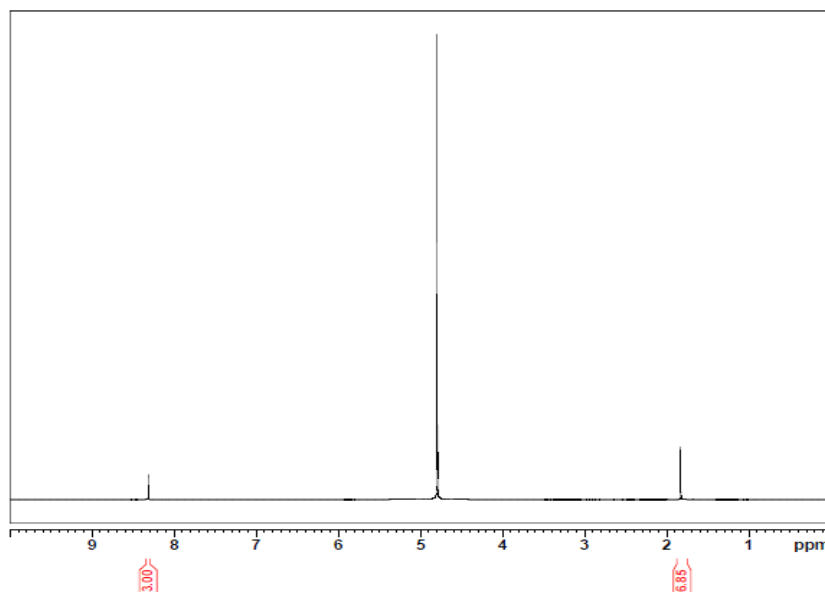
$$\begin{aligned} \text{BET surface area} &= \frac{N_a P V_m}{RT} \sigma_0 = \frac{6.022 \times 10^{23} \text{ mol}^{-1} \times 101325 \text{ Pa} \times 0.000356 \text{ m}^3 \text{ (STP) g}^{-1}}{8.31451 \frac{\text{J}}{\text{mol K}} \times 273.15 \text{ K}} \times 1.62 \times 10^{-19} \text{ m}^2 \\ &= 1548 \text{ m}^2 \text{ g}^{-1} \end{aligned}$$

Appendix 6-Calculation of molar ratios of molecular species in MOF-808 from NMR spectra



NMR spectra for (a) MOF-808-EDTA (b) MOF-808-benzoate (c) MOF-808-acetate

Calculation of molar ratios of molecular species in MOF-808-acetate

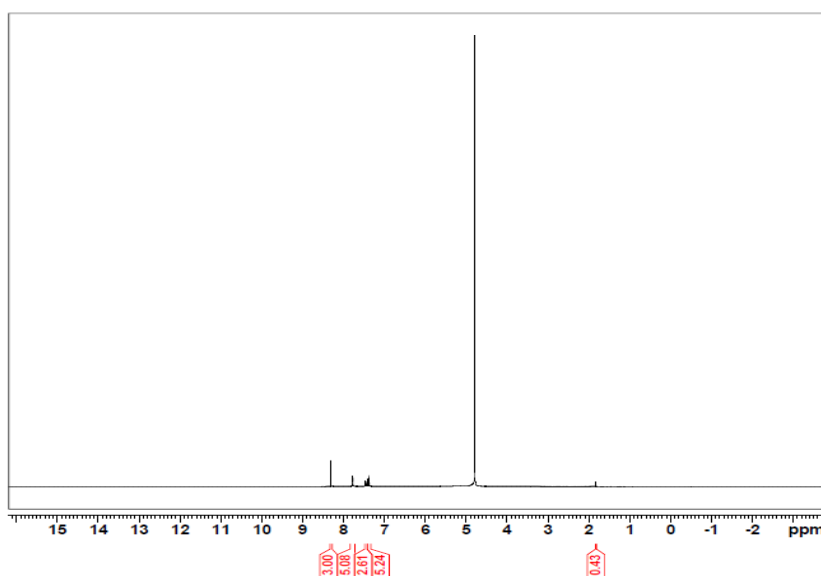


Acetic acid at
1.84ppm and
Trimesic acid at
8.33ppm

$$\frac{\text{Acetic acid}}{\text{Trimesic acid}} m_R = \left(\frac{\text{Acetic acid. 1H Int.}}{N_{\text{HAcetic acid.}}} \right) * \left(\frac{N_{\text{HTrimesic acid}}}{\text{Trimesic acid. 1H Int.}} \right)$$

$$\frac{\text{Acetic acid}}{\text{Trimesic acid}} m_R = \left(\frac{6.85}{3.0} \right) * \left(\frac{3.0}{3.0} \right) = 2.28$$

Calculation of molar ratios of molecular species in MOF-808-benzoate



Benzoic acid at 7.4, 7.5
and 7.8ppm. Acetic
acid at 1.84ppm and
Trimesic acid at
8.33ppm

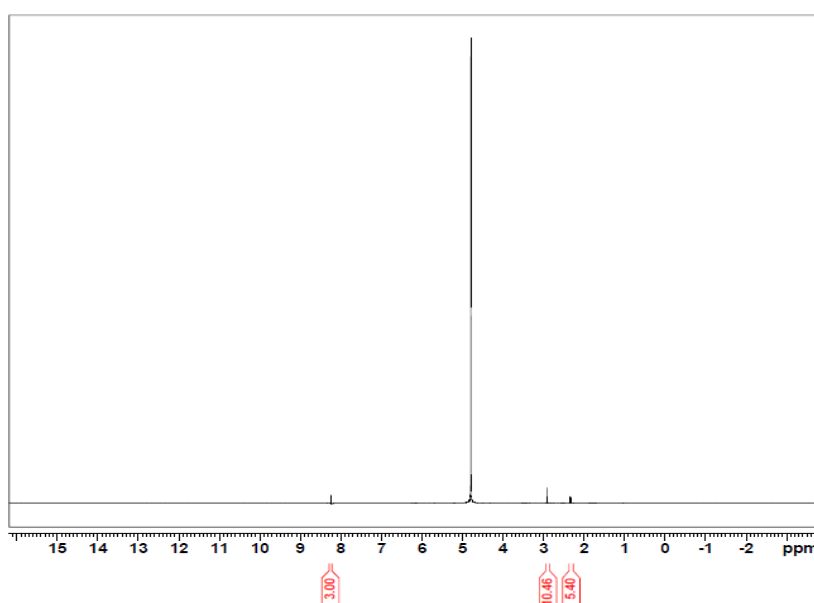
$$\frac{\text{Acetic acid}}{\text{Trimesic acid}} m_R = \left(\frac{\text{Acetic acid. 1H Int.}}{N_{\text{HAcetic acid.}}} \right) * \left(\frac{N_{\text{HTrimesic acid}}}{\text{Trimesic acid. 1H Int.}} \right)$$

$$\frac{\text{Actic acid}}{\text{Trimesic acid}} m_R = \left(\frac{0.43}{3.0}\right) * \left(\frac{3.0}{3.0}\right) = 0.143$$

$$\frac{\text{Benzoic acid}}{\text{Trimesic acid}} m_R = \left(\frac{\text{Benzoic acid. 1H Int.}}{N_{\text{HBenzoic acid.}}}\right) * \left(\frac{N_{\text{HTrimesic acid}}}{\text{Trimesic acid. 1H Int.}}\right)$$

$$\frac{\text{Benzoic acid}}{\text{Trimesic acid}} m_R = \left(\frac{4.9764 + 2.6502 + 5.1467}{5.0}\right) * \left(\frac{3.0}{3.0}\right) = 2.55$$

Calculation of molar ratios of molecular species in MOF-808-EDTA

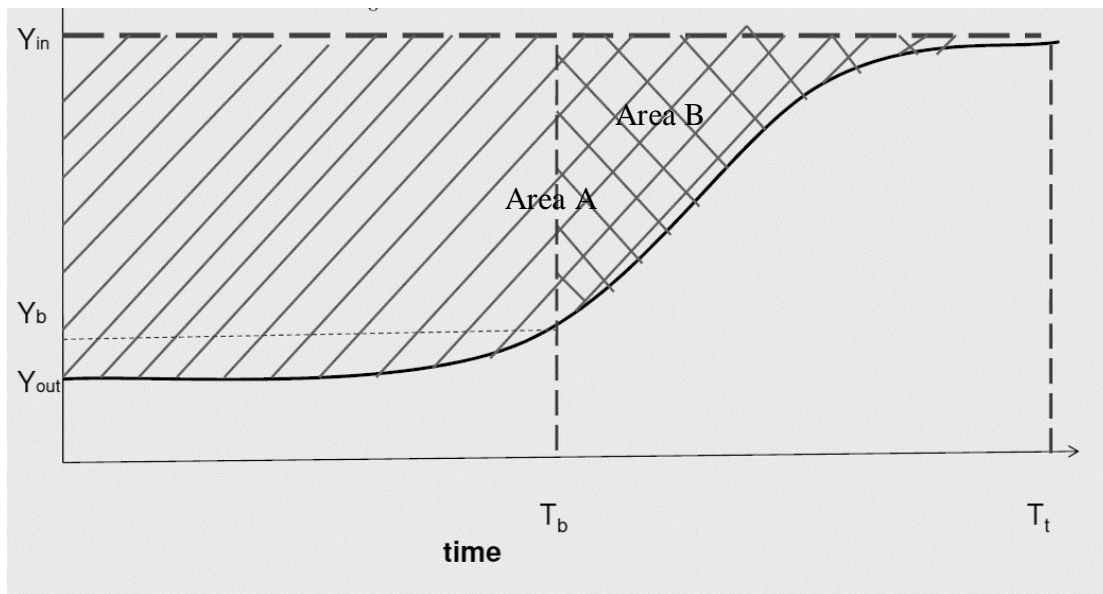


EDTA at 2.8 &
2.26ppm. Trimesic
acid at 8.24 ppm

$$\frac{\text{EDTA}}{\text{Trimesic acid}} m_R = \left(\frac{\text{EDTA. 1H Int.}}{N_{\text{HEDTA.}}}\right) * \left(\frac{N_{\text{HTrimesic acid}}}{\text{Trimesic acid. 1H Int.}}\right)$$

$$\frac{\text{EDTA}}{\text{Trimesic acid}} m_R = \left(\frac{10.46}{4.0}\right) * \left(\frac{3.0}{3.0}\right) = 2.61$$

Appendix 7- Calculation of LUB for resin column adsorption



Total bed capacity = Area A

Unused bed capacity = Area B

$$\frac{\text{Length of unused bed}}{\text{Length of total bed}} = \frac{\text{Unused bed capacity}}{\text{Total bed capacity}}$$

For Co^{2+}

$$\text{Length of unused bed} = \frac{286 \text{ squares}}{721.7 \text{ squares}} \times 5 \text{ cm} = 1.98 \text{ cm}$$

For Ni^{2+}

$$\text{Length of unused bed} = \frac{455.5 \text{ squares}}{940.5 \text{ squares}} \times 5 \text{ cm} = 2.42 \text{ cm}$$

$$\text{Used bed length} = 5 \text{ cm} - 1.98 \text{ cm} = 3.02 \text{ cm}$$

Appendix 8-Adsorption experiments for MOF-808 in single metal solutions

Adsorbent	Metal adsorbate	adsorbate initial concentration (mg L ⁻¹)	Initial solution pH	mass (g)	Solution volume (mL)	Concentration (mg L ⁻¹)	Removal %	Adsorption capacity(mg/g)
MOF-808-EDTA	Ni	2000	2	0.1	20	1734.81	12.02	47.4
MOF-808-EDTA	Ni	2000	4	0.1	20	1730.57	12.23	48.23
MOF-808-EDTA	Ni	2000	6	0.1	20	1733.75	12.07	47.6
MOF-808-EDTA	Co	600	2	0.1	20	470.37	22.55	27.39
MOF-808-EDTA	Co	600	4	0.1	20	432.46	28.8	34.98
MOF-808-EDTA	Co	600	6	0.1	20	437.35	27.99	34
MOF-808	Ni	2000	2	0.1	25	1965.46	0.7	3.46
MOF-808	Ni	2000	4	0.1	25	1941.13	1.92	9.5
MOF-808	Ni	2000	6	0.1	25	1950.65	1.44	7.13
MOF-808	Co	600	2	0.1	25	617.14	1.37	2.14
MOF-808	Co	600	4	0.1	25	623.26	0.39	0.61
MOF-808	Co	600	6	0.1	25	625.7	0	0
MOF-808-Benzoate	Ni	2000	2	0.1	20	1951.71	2.28	9.11
MOF-808-Benzoate	Ni	2000	4	0.1	20	1992.97	0.21	0.84
MOF-808-Benzoate	Ni	2000	6	0.1	20	1995.09	0.11	0.44
MOF-808-Benzoate	Co	600	2	0.1	20	580.45	2.86	3.42
MOF-808-Benzoate	Co	600	4	0.1	20	592.68	0.82	0.98
MOF-808-Benzoate	Co	600	6	0.1	20	593.9	0.01	0.01
MOF-808-DHBA	Ni	2000	2	0.1	20	1964.4	1.64	6.55

MOF-808 DHBA	Ni	2000	4	0.1	20	1994.03	0.16	0.64
MOF-808 DHBA	Ni	2000	6	0.1	20	1997.2	0	0
MOF-808 DHBA	Co	600	2	0.1	20	558.43	6.55	7.83
MOF-808 DHBA	Co	600	4	0.1	20	574.33	3.89	4.65
MOF-808 DHBA	Co	600	6	0.1	20	600.02	0	0

Appendix 9-Metal adsorption in simulated solution -ICP-OES results summary

Sample type	Al	Co	Cu	Fe	Li	Mn	Ni	Al	Co	Cu	Fe	Li	Mn	Ni
	Removal %							Adsorption capacity (mg/g)						
MOF-808-EDTA in synthetic solution-20 mLg ⁻¹	-	4.4	-	-	1.9	1.5	41.8	-	1	-	-	0.3	0.3	34.5
MOF-808-EDTA in synthetic solution -40 mLg ⁻¹	-	2.8	-	-	-4.2	-4.2	66.5	-	0.3	0	-	-0.3	-0.4	27.4